Hybrid As_2Se_3-PMMA Microtapers and Applications

Chams Baker

Department of Electrical & Computer Engineering
McGill University
Montreal, Canada

March 2013

A thesis report submitted to McGill University in partial fulfillment of the requirements for the degree of Doctor of Philosophy.

Abstract

In this thesis, a hybrid technology platform based on As_2Se_3 and PolyMethyl MethAcrylate (PMMA) is investigated with the aim of achieving versatile, compact, mechanically robust, and highly nonlinear microwires. Hybrid microwires composed of an As_2Se_3 core and a PMMA cladding are fabricated by tapering hybrid fiber structures using a state-of-the-art taper fabrication method. Two approaches based on two different hybrid fiber structures have been used for the fabrication of microwires. In the first approach, a single-mode hybrid fiber composed of an As_2Se_3 single-mode fiber and a PMMA coating layer is tapered to obtain a hybrid microwire. In the second approach, a bulk As_2Se_3 cylinder is coated with a PMMA layer to form a multi-mode hybrid fiber that is subsequently tapered into a hybrid microwire. The As_2Se_3 core of the microwire provides an ultrahigh nonlinearity up to $\gamma = 180$ $W^{-1}m^{-1}$ whereas the PMMA cladding provides mechanical strength for normal handling of the device and reduces sensitivity to the surrounding environment. With such a large waveguide nonlinearity parameter, a 10 cm hybrid microwire could replace a conventional highly non-linear silica fiber ($\gamma \sim 0.01$ $W^{-1}m^{-1}$) of 1.8 km. The successful operation of hybrid microwires is demonstrated with the observation of self-phase modulation, supercontinuum generation, and all-optical switching. Moreover, an hybrid microwire structure with an eccentric As_2Se_3 core and a PMMA cladding is fabricated to achieve ultrahigh birefringence and a high nonlinearity. The birefringence is induced by having the As_2Se_3 core eccentric with respect to the circular PMMA cladding symmetry. Eccentric-core microwires with high group birefringence up to $b_g = 0.018$ are demonstrated. Highly nonlinear eccentric-core hybrid microwires with engineerable birefringence can be used for applications such as polarization-entangled photon generation.

Résumé

Dans cette thèse, une plateforme technologique hybride basée sur l'As_2Se_3 et le PolyMethyl MethAcrylate (PMMA) est étudiée avec l'objectif d'obtenir des microfils hybrides hautement nonlinéaires, versatiles, compacts et mécaniquement robustes. Les microfils hybrides composés d'un coeur d'As_2Se_3 et d'une gaine de PMMA sont fabriqués par l'étirement de structures hybrides à partir de méthodes de fabrication dans l'état de l'art. Deux approches basées sur l'usage de deux structures de fibre hybrides ont été utilisées pour la fabrication des microfils. Dans la première approche, une fibre hybride monomode composée d'une fibre optique monomode d'As_2Se_3 enrobée d'une couche de PMMA est étirée pour l'obtention du microfil hybride. Dans la deuxième approche, un cylindre brut d'As_2Se_3 est enrobé de PMMA pour former une fibre hybride multimode et par la suite est étirée en microfil hybride. Le coeur d'As_2Se_3 du microfil génère une nonlinarité élevée de $\gamma = 180$ $W^{-1}m^{-1}$ tandis que la gaine de PMMA assure une robustesse mécanique suffisante pour la manipulation normale du dispositif et réduit la sensibilité à l'environnement. Avec une nonlinéarité de cet ordre, un microfil hybride de 10 cm peut remplacer une fibre conventionnelle et commerciale ($\gamma \sim 0.01$ $W^{-1}m^{-1}$) de 1.8 km. Le fonctionnement réussi de microfils hybrides est démontrée par l'observation d'automodulation de phase, la génération de supercontinuum, et la commutation tout-optique. De plus, une structure hybride de microfil avec un coeur excentrique et une gaine de PMMA est fabriquée pour atteindre une biréfringence élevée et une nonlinéarité élevée. La biréfringence est induite à partir du coeur d'As_2Se_3 excentrique par rapport à la symétrie circulaire de la gaine de PMMA. Des microfils hybrides excentriques avec une biréfringence élevée de $b_g = 0.018$ sont démontrés. Les microfils hybrides à haute biréfringence peuvent être utilisés pour les applications telles que la génération de photons à polarisation intriquée.

Acknowledgements

I would like to thank my supervisor Martin Rochette for his guidance and support. I am grateful to have had the opportunity to learn from his knowledge and experience in the field of nonlinear optics. I would also thank the McGill Photonic Systems Group including professors, graduate students, and staff who were always helpful and supportive. Thanks to Coractive High-Tech Inc and especially Mr. Stéphane Chatigny for generously providing the As_2Se_3 fiber, which is an essential component for this project. Finally, this work would not have been possible without the financial support from the NSERC, FQRNT, McGill University, and CIPI.

Contents

List of Figures

Chapter 1

Introduction

Light is made up of packets of energy called photons that are classified as elementary particles because they are not composed of any subparticles. The true nature of a photon is still a mystery because it sometimes behaves like a wave and othertimes it behaves like a particle. The wave behavior of a photon is confirmed by Young's double slit experiment where light shows an interference pattern known for waves. The particle behavior of a photon is confirmed by the photoelectric effect when photons knock electrons out of a negatively charged metal ball causing it to neutralize.

Generation, propagation, detection, and interaction of photons have been combined into a new scientific field of study called "Photonics". Photons generation can be observed in mundane activities such as lighting a fire or turning a light bulb ON. Generated photons can have different frequencies (colors), phases, or polarizations. Invention of lasers that generates a stream of photons having the same frequency, phase, and polarization has lead to a revolution in the study of photonics since its first demonstration in the 1960s.

Control of photon propagation has been achieved for centuries using light reflection and refraction and lead to practical tools such as mirrors and lenses which have been used in making eye glasses, telescopes, and microscopes. Total internal reflection has also been used to control photon propagation where it has been used to guide photons in step-index optical fibers over hundreds of kilometers. Legend says that the first account of guiding light by total internal reflection was discovered accidentally when a scientist was studying light refraction with a light source immersed in a water tank. When the scientist opened the valve to empty the water tank while the light source was still ON, he/she noticed that

light propagates along the water stream. It was later found that light propagation along the water stream was due to total internal reflection at the water/air interface and that such a guiding mechanism could be achieved in any dielectric cylinder surrounded by a material with a lower refractive index.

Light detection was first achieved through chemical reactions in photosensitive films. Later, with the discovery of electricity, it was noticed that the resistivity of semiconductors, such as intrinsic silicon crystals, changed with the intensity of light projected on it and provided a new method for light detection. The discovery and understanding of p-type semiconductors such as silicon crystals doped with Boron or Aluminum, and n-type semiconductors such as silicon crystals doped with Phosphorus or Arsenic lead to the development of P-N junctions as fast and highly sensitive device for the detection of light.

Interaction between photons has attracted attention due the increasing demand for fast all-optical data computation and communication. Photons interact in the presence of matter, and this interaction is observed as nonlinear optical effects. The first nonlinear effect was observed in the year 1961 where a laser beam was used to generate another laser beam at half the optical wavelength [3]. Devices based on nonlinear optical effect are called nonlinear devices and are key elements in all-optical signal processing.

1.1 Kerr Effect for Nonlinear Processing

One class of nonlinear devices is based on the Kerr effect in optical waveguides, where the refractive index of materials changes with the intensity of optical beams propagating in them [4]. Devices based on the nonlinear Kerr effect enable a wide range of all-optical processing applications such as switching [5], wavelength conversion [6], supercontinuum generation [7], and signal regeneration [8]. For pulses that propagate in a waveguide, the Kerr effect generates a time-dependent nonlinear phase-shift $\phi(t)$ with a maximum phase-shift $\phi_{SPM} = \gamma P_0 L_{eff}$, where $\gamma = k_0 n_2 / A_{eff}$ is the waveguide nonlinearity, P_0 is the peak power of the pulse, $L_{eff} = (1 - e^{-\alpha L})/\alpha$ is the effective length of the nonlinear waveguide, L is the length of the waveguide, α is the loss coefficient, A_{eff} is the modal effective area, n_2 is the material nonlinearity, $k_0 = 2\pi/\lambda$ is the wavenumber, and λ is the wavelength [9]. For a practical implementation of devices based on nonlinear effects, it is desirable to use a nonlinear medium with γ as high as possible such that a given ϕ_{SPM} can be achieved with a low power consumption (low P_0) and in a compact device (short L_{eff}).

1.2 Waveguide Nonlinearity Enhancement in As_2Se_3 Microwires

In one approach for increasing γ, materials with high n_2 such as chalcogenide glasses [10] and doped glasses [11] have been used. Chalcogenide glasses such as As_2Se_3, As_2S_3, and GeS_4 [12] are chemical solutions of elements from group seven in the periodic table of chemical elements. They have relatively high refractive indices of $n_{\mathrm{AsSe}} = 2.83$, $n_{\mathrm{AsS}} = 2.35$, and $n_{\mathrm{GeS}} = 2.51$ at $\lambda = 1550$ nm [13] due to their high material density. They also have a high material nonlinearity up to three orders of magnitude greater than that of silica as shown in Fig. 1.1 [1]. In particular, As_2Se_3 has the potential for a wide range of signal processing application because it has the highest n_2 between all chalcogenide glasses at $\lambda = 1550$ nm. Indeed, As_2Se_3 fibers have a high intrinsic material nonlinearity $n_2 = 1.1 \times 10^{-17}$ $\mathrm{m^2W^{-1}}$, about 500 times greater than that of silica [14].

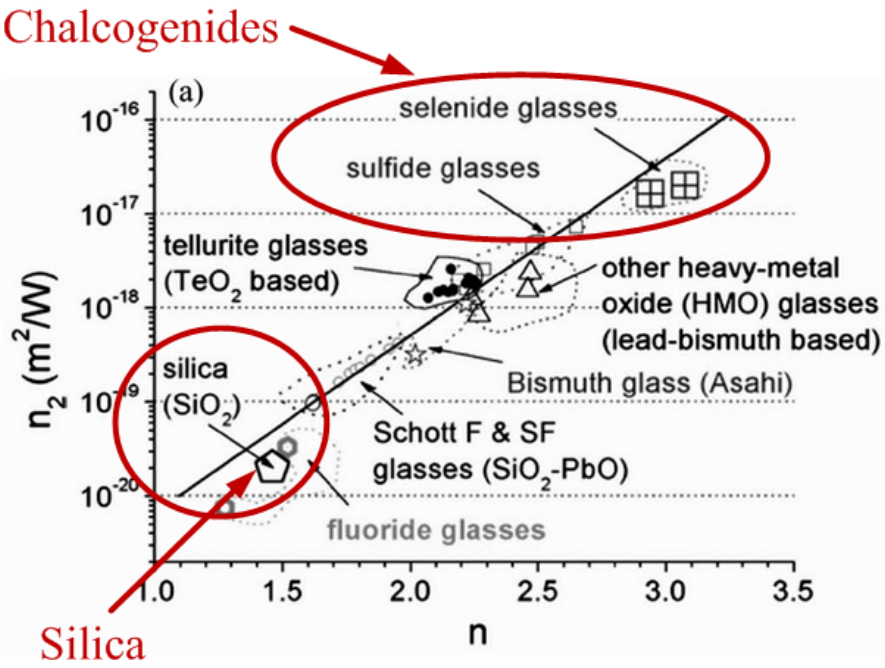

Fig. 1.1 Material nonlinearities [1]. © [2007] IEEE

In another approach, microwires with a large core to cladding refractive index contrast [15], photonic-crystal fibers [7, 16], and suspended-core optical fibers [17], as illustrated in Fig. 1.2, have been used to reduce A_{eff}. In particular, microwires fabricated by tapering optical fibers have two main advantages over other structures: first, efficient power

coupling into the microwire is achieved by gradual transformation of the fundamental mode diameter in the transition region of the taper, and second, they are fabricated starting from widely available standard step-index fibers. Microwires significantly confine optical beams due to the high difference between refractive indices of the microwire material and the surrounding material, which is air in most cases. Due to the tight confinement of optical beams in microwires, A_{eff} decreases and the beam intensity increases. As a result, the refractive index change due to Kerr effect becomes larger, and the nonlinear phase-shift and the waveguide nonlinearity increase.

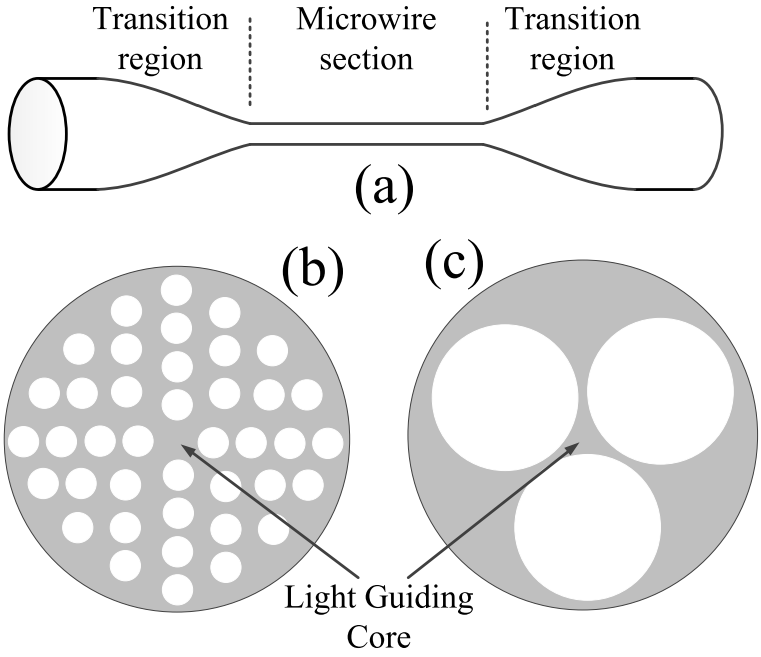

Fig. 1.2 Fiber structures with small A_{eff} including a) a microwire, b) a photonic-crystal fibers, and c) suspended-core fiber.

Microwires [18, 19], photonic-crystal fibers [20], and suspended-core fibers [21] made of chalcogenide glass combine both aforementioned approaches and thus achieve among the largest values of γ available in glass fiber structures. The first designs towards the fabrication of chalcogenide microwires were air-surrounded microwires [18]. Similar to photonic crystal and suspended-core fibers made of chalcogenide glasses [20, 21], such microwires are highly nonlinear and have an engineerable chromatic dispersion. However, chalcogenide microwires are prone to rupture due to their thin structure and must be used in a dust free

or controlled environment because $\sim 9\%$ of the fundamental mode propagates outside the microwire.

Microwires are formed in the waist of tapered optical fibers as presented in Fig. 1.2-a. The widespread heat-brush method is used for tapering fibers where a heater translates back and forth along a variable-length heating-zone and the taper is continuously stretched under tensile force [22]. This method is successful for the fabrication of tapered fibers with similar transition regions and a uniform waist [22–24], as illustrated in Fig. 1.2-a. We have developed and reported a generalized heat-brush tapering method that enables precise control of the shape of the taper waist [25].

1.3 Robust and Highly Nonlinear As_2Se_3-PMMA Microwires

Chalcogenide glasses have been combined with polymers, tellurite, and silica to form photonic fiber structures for a variety of applications. A Bragg fiber composed of alternating chalcogenide-polymer layers surrounding a polymer core have been fabricated to guide CO_2 laser light [26–28]. A photonic crystal fiber composed of a chalcogenide core and a holey tellurite cladding has been fabricated and used for supercontinuum generation [29]. More recently, a fiber with a chalcogenide core and a silica cladding has been used for supercontinuum generation in the near infrared [30].

We have reported the fabrication and optical characterization of the first hybrid As_2Se_3-PMMA microwire, prepared by tapering a single-mode step-index As_2Se_3 fiber that is coated with a PMMA layer [19]. Figure 1.3(a) presents a schematic of a hybrid microwire fabricated by tapering a single-mode step-index As_2Se_3 fiber that is coated with a PMMA layer [19]. With this material combination, the As_2Se_3 core of the microwire provides a large nonlinearity whereas the PMMA coating ensures mechanical robustness and flexibility to the assembly for normal handling as well as limiting the evanescent interaction with the environment. In the fabrication process of the hybrid microwire, a single-mode step-index As_2Se_3 fiber is used to ensure single-mode propagation from the fiber input to the microwire and from the microwire back to the fiber output, given that the taper transition region satisfies the adiabaticity criteria [31, 32]. In this case though, the transmission of the resulting hybrid microwire depends upon the As_2Se_3 fiber quality and design.

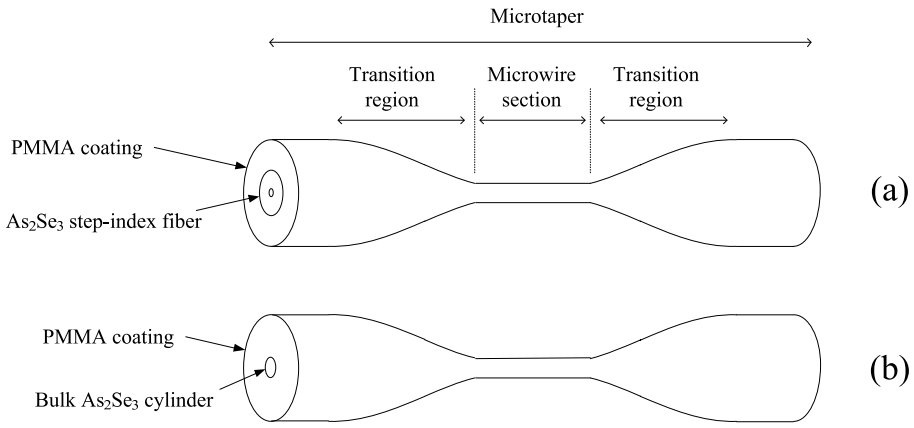

Fig. 1.3 Schematic of hybrid microtapers fabricated from a) a PMMA coated single-mode step-index As_2Se_3 fiber, and b) a PMMA coated multi-mode bulk As_2Se_3 cylinder.

Hybrid microtapers with single-mode transmission can also be fabricated from a multi-mode As_2Se_3-PMMA fiber composed of a bulk As_2Se_3 cylinder that is coated with a PMMA layer [33], as presented in Fig. 1.3(b). The multi-mode hybrid fiber must be tapered sufficiently such that only the fundamental mode is preserved in the As_2Se_3 core of the microwire. Single-mode transmission in tapered multi-mode fiber structures was first observed and studied in tapered fused couplers [22, 34]. Later, different tapering schemes have been used to filter out higher order modes in multi-mode fibers and achieve single-mode transmission [35–37].

Just as the hybrid microwires reported earlier in [19], hybrid microwires fabricated by tapering multi-mode As_2Se_3-PMMA fibers [33] provide single-mode transmission, an ultra-high waveguide nonlinearity, an enhanced mechanical robustness, and reduced sensitivity to the surrounding medium. In addition, tapered multi-mode As_2Se_3-PMMA fibers require low cost As_2Se_3 cylinders instead of the single-mode As_2Se_3 fibers, the initial core of the multi-mode As_2Se_3-PMMA fiber is tailored for optimal coupling between the fundamental modes of the hybrid fiber and the standard single-mode silica fibers, and the PMMA layer is thicker leading to further enhancement of the mechanical robustness and allowing for manual handling and easy packaging of the hybrid microwire.

1.4 Applications of As_2Se_3-PMMA Microwires

Chromatic dispersion in As_2Se_3-PMMA microwires has been engineered for specific applications such supercontinuum generation [19], soliton self-frequency shifting [38], and four-wave mixing [39]. The main design parameter in microwires with a uniform cross-section is the As_2Se_3 core diameter, which can be used to achieve zero dispersion at any wavelength in the C-band [19,39]. Another degree of freedom in the design of chromatic dispersion is achieved through the fabrication of microwires with a non-uniform cross-section, which can be used to shifts the zero-dispersion wavelength along the microwire [25, 38] for extended and flat supercontinuum generation [40, 41] and enhanced soliton self-frequency shift [38, 42].

High birefringence has been achieved in hybrid microwires by placing the As_2Se_3 core close to the air-PMMA interface [43], and thus forming an eccentric-core hybrid microwire [44–46]. Birefringence in such highly nonlinear microwires can be used for applications such as polarization-entangled photon generation by four-wave mixing [47, 48]. Birefringence engineering enables the selection of the wavelength at which the phase matching condition for four-wave mixing is satisfied [49, 50].

Bragg gratings in hybrid microwires have been fabricated using transverse holographic method using an HeNe laser at a wavelength of $\lambda = 633$ nm [51]. The high transparency of PMMA and the high photosensitivity of As_2Se_3 at $\lambda = 633$ nm allows for direct inscription of strong Bragg gratings on the As_2Se_3 core in the microwire. A Bragg grating with an extinction ratio of 40 dB in the C-band has been demonstrated [51]. Such Bragg gratings can be used for sensing applications [52, 53], all-optical switching [54], and slow light [55].

Dual-core hybrid micowires composed of two As_2Se_3 cores and a PMMA cladding can be used for a variety of linear applications such as power splitting and combining [56–60], polarization splitting and combining [56], filtering [57–60], and sensing [22, 61]. Dual-core hybrid microwires with highly nonlinear As_2Se_3 core can be used for all-optical switching [62]. The coupling length in hybrid couplers can be engineered by changing the diameter of each As_2Se_3 core or by varying the separation between the cores to reduce the all-optical switching power [62, 63].

1.5 The Thesis

In this thesis, I present the hybrid As_2Se_3-PMMA technology platform for the fabrication of highly nonlinear microwire structures composed of an As_2Se_3 core and a PMMA cladding. The aim of this thesis is to show that hybrid microwires provide high waveguide nonlinearity, and provide flexibility for the engineering of their linear properties such as chromatic dispersion and birefringence. First, I present methods for the analysis of the field distribution in microwires and the propagation of pulses in them. Second, I present an improved taper fabrication method which is used for the fabrication of hybrid microwires. Third, I present one approach for the fabrication of highly nonlinear hybrid microwires by tapering single-mode step-index As_2Se_3 fibers that are coated with a PMMA layer. Fourth, I present another approach for the fabrication of highly nonlinear hybrid microwires by tapering multi-mode hybrid As_2Se_3-PMMA fibers that are composed of an As_2Se_3 core and a PMMA cladding. Fifth, I present a the fabrication and characterization of highly nonlinear hybrid microwire with an eccentric-core for achieving high birefringence.

1.6 Comparison with Existing Technologies

Main competing technologies include air-cladding As_2Se_3 microwires, other hybrid microwires having an As_2Se_3 core with a tellurite or silica cladding, and fibers with advanced geometrical cross-section such as suspended-core and photonic crystal fibers. This section highlights the main advantages and disadvantages of hybrid As_2Se_3-PMMA microwires with respect to other competing technologies. Relevant points of comparison include mechanical robustness, sensitivity to the surrounding environment, waveguide nonlinearity, dispersion engineering, loss, length, ease of fabrication, and potential applications.

Air-Cladding As_2Se_3 Microwires

The advantages of coated microwires with respect to uncoated microwires include enhanced mechanical robustness, reduced sensitivity to the surrounding environment, dispersion engineering, and length. First, the thick PMMA cladding in hybrid microwires leads to enhanced mechanical robustness and reduced sensitivity to the surrounding environment. Second, hybrid microwires provide additional freedom in dispersion engineering by changing the the PMMA cladding diameter and the use of dye-doped polymers. Finally, uncoated

microwires are fabricated using a tapering process and are limited to a length ≤ 30 cm. An As_2Se_3 microwire coated with a PMMA layer does not have this limitation because a hybrid fiber with a submicron As_2Se_3 core and a PMMA cladding with a diameter > 80 μm can be fabricated by drawing hybrid fiber preforms to obtain any fiber length.

The disadvantages of coated microwires with respect to uncoated microwires include lower waveguide nonlinearity, and higher loss. The core/cladding refractive-index-difference of uncoated microwires [18] with an As_2Se_3 core and an air cladding, $\Delta n = 2.37$, is higher than that of hybrid microwires with and As_2Se_3 core and a PMMA cladding, $\Delta n = 1.83$; hence, uncoated microwires lead to higher waveguide nonlinearity than hybrid microwires. For example, the maximum nonlinearity at $\lambda = 1550$ nm for an uncoated microwire can theoretically reach $\gamma = 255$ $W^{-1}m^{-1}$, whereas it can theoretically reach $\gamma = 187$ $W^{-1}m^{-1}$ in a hybrid microwire. Moreover, replacing the air cladding with a PMMA cladding increases signal attenuation as the PMMA have high absorption losses. The loss in uncoated microwires at the diameter of maximum nonlinearity is 0.0073 dB/cm, whereas the loss in hybrid microwires at the diameter of maximum nonlinearity is 0.069 dB/cm.

Other Hybrid Microwires

Other hybrid structures such as silica-coated and tellurite-coated hybrid mirowires provide similar waveguide nonlinearity and chromatic dispersion values as PMMA-coated microwires [29, 30]. Moreover, similar to PMMA-coated microwires, tellurite-coated microwires can be fabricated using a heat-and-draw process because chalcogenide glasses and tellurite have similar softening temperatures [29]. The advantages of PMMA-coated microwires with respect to other hybrid microwires include ease of fabrication, and unique potential applications. The softening temperatures of silica and chalcogenide glasses differ by more than 1000° C and can not be fabricated using conventional fiber drawing techniques. Instead, a hollow-core silica fiber is drawn separately, and then molten chalcogenide glass is injected into the hollow core [30]. Moreover, the organic chemical composition of the cladding in PMMA-coated hybrid microwires has several advantages over the inorganic chemical composition of the cladding in tellurite-coated and silica-coated hybrid microwires including the following: first, PMMA is porous giving it the ability to trap other chemical molecules for sensing applications, and second, PMMA can incorporate organic dyes for nonlinearity enhancement, dispersion engineering, and sensing applications. The only

disadvantage of PMMA coated hybrid microwires with respect to other hybrid structures is higher loss. Silica-coated and tellurite-coated hybrid mirowires have lower attenuation because silica and tellurite have lower absorption losses than PMMA.

Suspended-Core and Photonic Crystal Fibers

Similar to hybrid microwires, suspended-core fibers guide light by total internal-reflection [64–66]; however, photonic-crystal fibers guide light through a photonic bandgap [67]. The disadvantages of hybrid microwires with respect to fibers with advanced geometrical cross-sections such as suspended-core and photonic crystal fibers include dispersion engineering and loss. Dispersion in photonic-crystal fibers depends on the air-hole diameter d and the hole to hole spacing Λ, and hence provides additional parameters for dispersion engineering [68, 69]. Moreover, suspended-core and photonic-crystal fibers exhibit losses exceeding 0.01 dB/cm when the core diameter is reduced to maximize γ [26, 27, 69]; however, it is still lower than the loss in hybrid microwires, 0.069 dB/cm. The disadvantages of hybrid microwires with respect to suspended-core and photonic crystal fibers can be turned into advantages as follows. If a polymer with lower losses than PMMA is used, the hybrid microwires will have much lower loss. Moreover, our hybrid technology platform can incorporate the dispersion engineering advantage of suspended-core and photonic-crystal fibers by replacing the air-holes in these structures with PMMA to obtain hybrid suspended-core and photonic-crystal fibers. In fact, replacement of air with PMMA in suspended-core and photonic-crystal fibers simplifies the fabrication process because it eliminates the problem of hole collapse.

1.7 Main Contributions

Our main contributions include the following: first, development and demonstration both by simulation and experiment of a generalized heat-brush tapering method for precise fabrication of tapers with a nonuniform waist profile and dissimilar transition regions, as presented in Chapter 3; second, a method for simultaneous measurement of the core diameter D and numerical aperture NA using the transmission spectrum of a step-index optical fiber in the dual-mode wavelength range, as presented in Chapter 4; third, the fabrication and optical characterization of the first hybrid chalcogenide-polymer microwires obtained by tapering single-mode hybrid As_2Se_3-PMMA fibers, as presented in Chapter 4; forth,

demonstration of single-mode transmission and high nonlinearity in tapered multi-mode As_2Se_3-PMMA fibers, as presented in Chapter 5; fifth, the fabrication and characterization of ECHMs with high birefringence and high nonlinearity, using the hybrid As_2Se_3-PMMA technology platform, as presented in Chapter 6.

1.8 Outline

Chapter 2 introduces the methods used in the analysis of microwire structures. First, the basic microwires structure with an As_2Se_3 core and a PMMA cladding is analyticaly studied using a step-index fiber model. Second, microwires with complex structures such as a finite-cladding or an eccentric-core are numerically analyzed using the tangential vector finite-element method. Third, the nonlinear Schrodinger equation is derived for modeling pulse propagation in microwires. Finally, the split-step Fourier method is used for simulating pulse propagation in a microwire by numerically solving the nonlinear Schrodinger equation.

Chapter 3 presents the development and demonstration both by simulation and experiment of the generalized heat-brush tapering method. First, single-sweep tapering is presented and simulated using a viscous fluid flow model. Then, the generalized heat-brush approach is implemented by tapering a fiber over multiple sweeps. The simulation results from the single-sweep tapering analysis are used to quantify the accumulated mismatch error after each tapering sweep. Finally, we use of the generalized heat-brush approach to fabricate an As_2Se_3 chalcogenide taper with a linearly decreasing waist profile and dissimilar transition regions.

Chapter 4 presents the fabrication of a hybrid As_2Se_3-PMMA microwires from single-mode hybrid As_2Se_3-PMMA fibers. First, As_2Se_3-PMMA fibers are fabricated by coating a single-mode As_2Se_3 fiber with a PMMA layer. Second, hybrid micorwire parameters including the waveguide nonlinearity, chromatic dispersion, and material loss are calculated using the analysis methods presented in Chapter 2. Third, the hybrid fiber is tapered using the tapering method presented in Chapter 3 to obtain a hybrid microwire. Finally, self-phase modulation and super-continuum generation are demonstrated in the fabricated microwires.

Chapter 5 investigates an alternative approach for the fabrication of hybrid As_2Se_3-PMMA microwires by tapering multi-mode hybrid As_2Se_3-PMMA fibers. First, multi-mode and large refractive index contrast hybrid fibers are fabricated with an As_2Se_3 core and a

PMMA cladding. The As_2Se_3 core diameter is designed for optimal coupling between the fundamental mode of the hybrid fiber and the fundamental mode of a standard single-mode silica fiber (SMF). Second, a segment of this multi-mode fiber is tapered into a microwire until the As_2Se_3 core sustains single-mode transmission. Finally, the microwire is characterized and used as the nonlinear component of a Kerr-shutter to a achieve all-optical switching.

Chapter 6 presents the fabrication and characterization of eccentric-core hybrid microwires with high birefringence and high nonlinearity. First, birefringence in eccentric-core microwires is calculated using the finite-element method presented in Chapter 2. Second, eccentric-core multi-mode hybrid fibers are fabricated with an eccentric As_2Se_3 core and a PMMA cladding using the multi-mode hybrid fiber fabrication method presented in Chapter 5. Third, a segment of the eccentric-core multi-mode fiber is tapered into a microwire with single-mode transmission. Finally, group birefringence and the waveguide nonlinearity of the resulting eccentric-core hybrid microwire are characterized to show close agreement with numerically calculated values.

Chapter 6 presents some conclusive remarks and a few of the research projects that have been triggered by the results obtained in this thesis.

1.9 List of Publications

Relevant journal publications

Chams Baker, Martin Rochette, “Birefringence engineering and high nonlinearity in eccentric-core As_2Se_3-PMMA microtapers”, J. Lightwave Tech. (2012)

Chams Baker, Martin Rochette, "High nonlinearity and single-mode transmission in tapered multimode As_2Se_3-PMMA fibers," J. Photon. 4, 3, 960-969 (2012)

Chams Baker, Raja Ahmad, Martin Rochette, "Simultaneous measurement of the core diameter and the numerical aperture in dual-mode step-index optical fibers," J. Lightwave Tech. 29, 24, 3834-3837 (2011)

Chams Baker, Martin Rochette, "A generalized heat-brush approach for precise control of the waist profile in fiber tapers," Opt. Mater. Express 1, 1065-1076 (2011)

Chams Baker, Martin Rochette, "Highly nonlinear hybrid AsSe-PMMA microtapers," Opt. Express 18, 12391-12398 (2010)

Other journal publications

Alaa Al-kadry, Chams Baker, Mohammed El Amraoui, Younes Messaddeq, and Martin Rochette, "Broadband supercontinuum generation in As_2Se_3 chalcogenide wires by avoiding the two-photon absorption effects", JOSA B, (2013)

Raja Ahmad, Martin Rochette, and Chams Baker, "Fabrication of Bragg gratings in subwavelength diameter As_2Se_3 chalcogenide wires," Opt. Lett. 36, 2886-2888 (2011)

Martin Rochette, Chams Baker, and Raja Ahmad, "All-optical polarization-mode dispersion monitor for return-to-zero optical signals at 40 Gbits/s and beyond," Opt. Lett. 35, 3703-3705 (2010)

Chapter 2

Microwire Analysis

In this chapter, methods used in microwire analysis are presented. Microwire analysis aspects of interest are the calculation of microwire modes and their associated parameters including dispersion birefringence and nonlinearity, and the simulation of pulse propagation in the microwire with inclusion of the effects of dispersion, birefringence, and nonlinearity. First, we present analytical study of step-index fibers used to model microwires. Second, the tangential vector finite-element method is presented for analyzing microwires with complex structures such as finite-cladding and eccentric-core microwires. Third, the nonlinear Schrodinger equation for modeling pulse propagation in microwires is presented. Fourth, the split-step Fourier method is presented for numerically solving the nonlinear Schrodinger equation and simulating pulse propagation in a microwire.

2.1 Step-Index Fiber Waveguides

In this section, we present an analysis of step-index fiber waveguide used for modeling microwires. Figure 2.1 presents a schematic of a microwire structure, which is modeled a cylindrical core surrounded by an infinite cladding. This analysis is used to find the effective refractive indices and the vector field distribution of the modes propagating in the microwire, which are used to calculate the main microwire parameters including the chromatic dispersion and the waveguide nonlinearity.

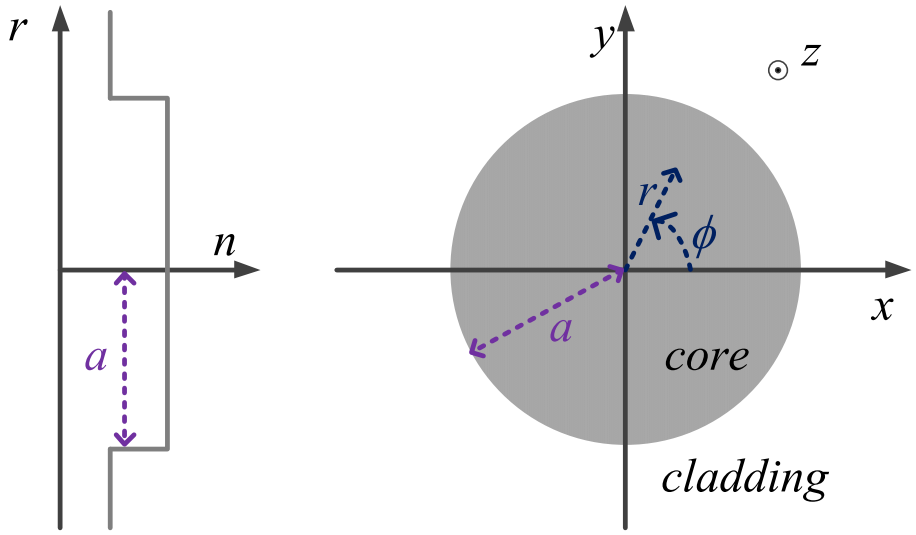

Fig. 2.1 Schematic of a microwire with an infinite cladding diameter.

The propagation of an electromagnetic field is governed by the Maxwell equations given by

$$\nabla \times \vec{E} = -\frac{\partial \vec{B}}{\partial t} \tag{2.1}$$

$$\nabla \times \vec{H} = \vec{J} + \frac{\partial \vec{D}}{\partial t} \tag{2.2}$$

$$\nabla . \vec{D} = \rho_f \tag{2.3}$$

$$\nabla . \vec{B} = 0 \tag{2.4}$$

where $\vec{E}$ and $\vec{H}$ are the electric and magnetic field vectors, ρ_f is the charge density, $\vec{J}$ is the current density, $\vec{D}$ and $\vec{B}$ are the electric and magnetic flux densities given by

$$\vec{D} = \varepsilon_0 \vec{E} + \vec{P}, \tag{2.5}$$

$$\vec{B} = \mu_0 \vec{H} + \vec{M}, \tag{2.6}$$

with $\vec{P}$ and $\vec{M}$ being the induced electric and magnetic polarizations. Dielectric glasses used in optical fiber are charge free and nonmagnetic leading to $\vec{J} = 0$, $\rho_f = 0$, and $\vec{M} = 0$.

Application of the curl operator to Eq. 2.1 leads to

$$\nabla \times \nabla \times \vec{E} = \nabla \times \left[-\frac{\partial \vec{B}}{\partial t} \right],$$

and with the application of Eq. 2.5, the last equation is rearranged to obtain

$$\nabla \times \nabla \times \vec{E} = -\mu_0 \frac{\partial}{\partial t} \left[\nabla \times \vec{H} \right].$$

This equation is expressed in terms of the electric field $\vec{E}$ by using Eq. 2.2 to obtain

$$\nabla \times \nabla \times \vec{E} = -\mu_0 \varepsilon \frac{\partial^2 \vec{E}}{\partial t^2},$$

and the application of the vector identity $\nabla \times \left(\nabla \times \vec{A} \right) = \nabla \left(\nabla \cdot \vec{A} \right) - \nabla^2 \vec{A}$ leads to

$$\nabla \left(\nabla \cdot \vec{E} \right) - \nabla^2 \vec{E} = -\mu_0 \varepsilon \frac{\partial^2 \vec{E}}{\partial t^2}.$$

In a homogeneous medium, where the refractive index is the same everywhere, the term $\nabla \left(\nabla \cdot \vec{E} \right)$ is zero leading to the Helmholtz equation

$$\nabla^2 \vec{E} - \mu \varepsilon \frac{\partial^2 \vec{E}}{\partial t^2} = 0. \tag{2.7}$$

In a circular coordinate system, the electric field $\vec{E}$ is expressed as

$$\vec{E}\left(r, \phi, z\right) = E_r\left(r, \phi, z\right) \hat{r} + E_\phi\left(r, \phi, z\right) \hat{\phi} + E_z\left(r, \phi, z\right) \hat{z} \tag{2.8}$$

and Eq. 2.7 becomes

$$\begin{aligned} &\left(\nabla^2 E_r - \tfrac{2}{r^2} \tfrac{\partial E_\phi}{\partial \phi} - \tfrac{E_r}{r^2} \right) \hat{r} + \left(\nabla^2 E_\phi + \tfrac{2}{r^2} \tfrac{\partial E_r}{\partial \phi} - \tfrac{E_\phi}{r^2} \right) \hat{\phi} \\ &\quad + \left(\nabla^2 E_z \right) \hat{z} - \mu \varepsilon \tfrac{\partial^2}{\partial t^2} \left(E_r \hat{r} + E_\phi \hat{\phi} + E_z \hat{z} \right) = 0 \end{aligned}$$

leading the following set of equations

$$\nabla^2 E_r - \frac{2}{r^2}\frac{\partial E_\phi}{\partial \phi} - \frac{E_r}{r^2} - \mu\varepsilon\frac{\partial^2}{\partial t^2}E_r = 0$$

$$\nabla^2 E_\phi + \frac{2}{r^2}\frac{\partial E_r}{\partial \phi} - \frac{E_\phi}{r^2} - \mu\varepsilon\frac{\partial^2}{\partial t^2}E_\phi = 0$$

$$\nabla^2 E_z - \mu\varepsilon\frac{\partial^2}{\partial t^2}E_z = 0$$

The equation for E_z is expanded as

$$\frac{1}{r}\frac{\partial}{\partial r}\left(r\frac{\partial E_z}{\partial r}\right) + \frac{1}{r^2}\frac{\partial^2 E_z}{\partial \phi^2} + \frac{\partial^2 E_z}{\partial z^2} - \mu\varepsilon\frac{\partial^2}{\partial t^2}E_z = 0 \tag{2.9}$$

and is solved using the method of separation of variables by assuming the solution E_z has the form

$$E_z\left(r,\phi,z\right) = R\left(r\right)\Phi\left(\phi\right)Z\left(z\right)e^{j\omega t}. \tag{2.10}$$

Replacing E_z from Eq. 2.10 in Eq. 2.9 leads to

$$\frac{1}{R\left(r\right)}\frac{1}{r}\frac{\partial R\left(r\right)}{\partial r} + \frac{1}{R\left(r\right)}\frac{\partial^2 R\left(r\right)}{\partial r^2} + \frac{1}{\Phi\left(\phi\right)}\frac{1}{r^2}\frac{\partial^2 \Phi\left(\phi\right)}{\partial \phi^2} + \frac{1}{Z\left(z\right)}\frac{\partial^2 Z\left(z\right)}{\partial z^2} + k_0^2 n^2 = 0$$

which is rearranged as

$$\frac{1}{R\left(r\right)}\frac{1}{r}\frac{\partial R\left(r\right)}{\partial r} + \frac{1}{R\left(r\right)}\frac{\partial^2 R\left(r\right)}{\partial r^2} + \frac{1}{\Phi\left(\phi\right)}\frac{1}{r^2}\frac{\partial^2 \Phi\left(\phi\right)}{\partial \phi^2} + k_0^2 n^2 = -\frac{1}{Z\left(z\right)}\frac{\partial^2 Z\left(z\right)}{\partial z^2}$$

to obtain

$$\begin{cases} -\frac{1}{Z(z)}\frac{\partial^2 Z(z)}{\partial z^2} = \beta^2, \\ \frac{1}{R(r)}\frac{1}{r}\frac{\partial R(r)}{\partial r} + \frac{1}{R(r)}\frac{\partial^2 R(r)}{\partial r^2} + \frac{1}{\Phi(\phi)}\frac{1}{r^2}\frac{\partial^2 \Phi(\phi)}{\partial \phi^2} + k_0^2 n^2 = \beta^2. \end{cases}$$

The equation in $Z\left(z\right)$ is solved as

$$Z\left(z\right) = e^{-j\beta.z} \tag{2.11}$$

whereas the second equation is rearranged as

$$\frac{r}{R(r)}\frac{\partial R(r)}{\partial r}+\frac{r^2}{R(r)}\frac{\partial^2 R(r)}{\partial r^2}+k_0^2n^2r^2-\beta^2r^2=-\frac{1}{\Phi(\phi)}\frac{\partial^2\Phi(\phi)}{\partial\phi^2}$$

to obtain

$$\begin{cases} -\frac{1}{\Phi(\phi)}\frac{\partial^2\Phi(\phi)}{\partial\phi^2}=v^2, \\ \frac{r}{R(r)}\frac{\partial R(r)}{\partial r}+\frac{r^2}{R(r)}\frac{\partial^2 R(r)}{\partial r^2}+k_0^2n^2r^2-\beta^2r^2=v^2. \end{cases}$$

The equation of $\Phi(\phi)$ is solved as

$$\Phi(\phi)=e^{jv\phi} \tag{2.12}$$

where v must be an integer which to satisfy the condition $\Phi(\phi)=\Phi(\phi+2\pi)$. The equation of $R(r)$, rearranged as

$$\frac{\partial^2 R(r)}{\partial r^2}+\frac{1}{r}\frac{\partial R(r)}{\partial r}+\left(k_0^2n^2-\beta^2-\frac{v^2}{r^2}\right)R(r)=0, \tag{2.13}$$

is known as the Bessel differential equation, which is solved using the series method to obtain a series expansion of the solutions known as the Bessel functions [70].

The microwire is composed of a cylindrical core and a cladding, and the refractive index distribution in the microwire is given by

$$n=\begin{cases} n_1 & \text{for } r\le a, \\ n_2 & \text{for } r>a. \end{cases}$$

where n_1 and n_2 are the refractive indices of the core and the cladding, respectively, and a is the radius of the core. Within the core, $(k_0^2n_1^2-\beta^2-v^2/r^2)>0$ and the solution is given by $R(r)=AJ_v(\kappa r)+BY_v(\kappa r)$ where $J_v(\kappa r)$ and $Y_v(\kappa r)$ are the Bessel functions and $\kappa^2=k_0^2n_1^2-\beta^2$. The function $Y_v(\kappa r)$ has an infinite value at $r=0$, and hence, B must be zero because the field energy should be finite. Outside the core, $(k_0^2n_2^2-\beta^2-v^2/r^2)<0$ and the solution is given by $R(r)=CK_v(\gamma r)+DI_v(\gamma r)$ where $K_v(\gamma r)$ and $I_v(\gamma r)$ are the modified Bessel functions and $\gamma^2=\beta^2-k_0^2n_2^2$. The function $I_v(\gamma r)$ has an infinite value as $r\to\infty$, and hence, D must be zero to get a physically acceptable solution. The solution of Eq. 2.13 is $R(r)=AJ_v(\kappa r)$ inside the core and $R(r)=CK_v(\gamma r)$ in the cladding and

the distribution of the z-component of the electric field E_z is given by

$$\left\{ \begin{array}{ll} E_z\left(r,\phi,z\right) = AJ_v\left(\kappa r\right)e^{jv\phi}e^{-j\beta.z}e^{j\omega t} & r \leq a, \\ E_z\left(r,\phi,z\right) = CK_v\left(\gamma r\right)e^{jv\phi}e^{-j\beta.z}e^{j\omega t} & r \geq a. \end{array} \right\} \tag{2.14}$$

Using a similar analysis as the one for the electric field, the distribution of the z-component of magnetic field H_z is given by

$$\left\{ \begin{array}{ll} H_z\left(r,\phi,z\right) = A'J_v\left(\kappa r\right)e^{jv\phi}e^{-j\beta.z}e^{j\omega t} & r \leq a \\ H_z\left(r,\phi,z\right) = C'K_v\left(\gamma r\right)e^{jv\phi}e^{-j\beta.z}e^{j\omega t} & r \geq a \end{array} \right\} \tag{2.15}$$

The remaining electric and magnetic field components E_r, E_ϕ, H_r, and H_ϕ are calculated from E_z and H_z using

$$\left\{ \begin{array}{l} E_r = \frac{j\beta}{\omega^2\mu\varepsilon-\beta^2}\left[\frac{\partial E_z}{\partial r} + \frac{\omega\mu}{\beta}\frac{1}{r}\frac{\partial H_z}{\partial \phi}\right] \\ E_\phi = \frac{j\beta}{\omega^2\mu\varepsilon-\beta^2}\left[\frac{1}{r}\frac{\partial E_z}{\partial \phi} - \frac{\omega\mu}{\beta}\frac{\partial H_z}{\partial r}\right] \\ H_r = \frac{j\beta}{\omega^2\mu\varepsilon-\beta^2}\left[\frac{\partial H_z}{\partial r} - \frac{\omega\varepsilon}{\beta}\frac{1}{r}\frac{\partial E_z}{\partial \phi}\right] \\ H_\phi = \frac{j\beta}{\omega^2\mu\varepsilon-\beta^2}\left[\frac{1}{r}\frac{\partial H_z}{\partial \phi} - \frac{\omega\varepsilon}{\beta}\frac{\partial E_z}{\partial r}\right] \end{array} \right. \tag{2.16}$$

Replacing E_z and H_z from Eq. 2.14 and Eq. 2.15 for $r \leq a$ in Eq. 2.16 leads to

$$\left\{ \begin{array}{l} E_r = \frac{-j\beta}{\kappa^2}\left[A\kappa\frac{\partial J_v(\kappa r)}{\partial \kappa r} + \frac{j\omega\mu v}{\beta r}A'J_v\left(\kappa r\right)\right]e^{jv\phi}e^{-j\beta.z}e^{j\omega t} \\ E_\phi = \frac{-j\beta}{\kappa^2}\left[\frac{jv}{r}AJ_v\left(\kappa r\right) - \frac{\omega\mu}{\beta}A'\kappa\frac{\partial J_v(\kappa r)}{\partial \kappa r}\right]e^{jv\phi}e^{-j\beta.z}e^{j\omega t} \\ H_r = \frac{-j\beta}{\kappa^2}\left[A'\kappa\frac{\partial J_v(\kappa r)}{\partial \kappa r} - \frac{j\omega\varepsilon_0 n_1^2 v}{\beta r}AJ_v\left(\kappa r\right)\right]e^{jv\phi}e^{-j\beta.z}e^{j\omega t} \\ H_\phi = \frac{-j\beta}{\kappa^2}\left[\frac{jv}{r}A'J_v\left(\kappa r\right) + \frac{\omega\varepsilon_0 n_1^2}{\beta}A\kappa\frac{\partial J_v(\kappa r)}{\partial \kappa r}\right]e^{jv\phi}e^{-j\beta.z}e^{j\omega t} \end{array} \right. \tag{2.17}$$

and replacing Eq. 2.14 and Eq. 2.15 for $r \geq a$ in Eq. 2.16 leads to

$$\left\{ \begin{array}{l} E_r = \frac{j\beta}{\gamma^2}\left[C\gamma\frac{\partial K_v(\gamma r)}{\partial \gamma r} + \frac{j\omega\mu v}{\beta r}C'K_v\left(\gamma r\right)\right]e^{jv\phi}e^{-j\beta.z}e^{j\omega t} \\ E_\phi = \frac{j\beta}{\gamma^2}\left[\frac{jv}{r}CK_v\left(\gamma r\right) - \frac{\omega\mu}{\beta}C'\gamma\frac{\partial K_v(\gamma r)}{\partial \gamma r}\right]e^{jv\phi}e^{-j\beta.z}e^{j\omega t} \\ H_r = \frac{j\beta}{\gamma^2}\left[C'\gamma\frac{\partial K_v(\gamma r)}{\partial \gamma r} - \frac{j\omega\varepsilon_0 n_2^2 v}{\beta r}CK_v\left(\gamma r\right)\right]e^{jv\phi}e^{-j\beta.z}e^{j\omega t} \\ H_\phi = \frac{j\beta}{\gamma^2}\left[\frac{jv}{r}C'K_v\left(\gamma r\right) + \frac{\omega\varepsilon_0 n_2^2}{\beta}C\gamma\frac{\partial K_v(\gamma r)}{\partial \gamma r}\right]e^{jv\phi}e^{-j\beta.z}e^{j\omega t} \end{array} \right. \tag{2.18}$$

The set of values of β and v that make the tangential electric field components E_z, H_z, E_ϕ and H_ϕ continuous at the core/cladding boundary correspond to the modes of the

microwire. The continuity of E_z, H_z, E_ϕ and H_ϕ at the boundary leads to

$$\begin{cases} AJ_v(\kappa a) = CK_v(\gamma a) \\ A'J_v(\kappa a) = C'K_v(\gamma r) \\ \frac{-j\beta}{\kappa^2}\left[\frac{jv}{a}AJ_v(\kappa a) - \frac{\omega\mu}{\beta}A'\kappa\frac{\partial J_v(\kappa a)}{\partial \kappa r}\right] = \frac{j\beta}{\gamma^2}\left[\frac{jv}{a}CK_v(\gamma a) - \frac{\omega\mu}{\beta}C'\gamma\frac{\partial K_v(\gamma a)}{\partial \gamma r}\right] \\ \frac{-j\beta}{\kappa^2}\left[\frac{jv}{a}A'J_v(\kappa a) + \frac{\omega\varepsilon_0 n_1^2}{\beta}A\kappa\frac{\partial J_v(\kappa a)}{\partial \kappa r}\right] = \frac{j\beta}{\gamma^2}\left[\frac{jv}{a}C'K_v(\gamma a) + \frac{\omega\varepsilon_0 n_2^2}{\beta}C\gamma\frac{\partial K_v(\gamma a)}{\partial \gamma r}\right] \end{cases} \tag{2.19}$$

which is rearranged to obtain

$$[\mathbf{M}]\begin{pmatrix} A & A' & C & C' \end{pmatrix}^T = 0 \tag{2.20}$$

where

$$[\mathbf{M}] = \begin{pmatrix} J_v(\kappa a) & 0 & -K_v(\gamma a) & 0 \\ 0 & J_v(\kappa a) & 0 & -K_v(\gamma a) \\ \frac{\beta v}{a\kappa^2}J_v(\kappa a) & \frac{j\mu\omega}{\kappa}J_v'(\kappa a) & \frac{\beta v}{a\gamma^2}K_v(\gamma a) & \frac{j\mu\omega}{\gamma}K_v'(\gamma a) \\ \frac{-j\omega\varepsilon_0 n_1^2}{\kappa}J_v'(\kappa a) & \frac{\beta v}{a\kappa^2}J_v(\kappa a) & \frac{-j\omega\varepsilon_0 n_2^2}{\gamma}K_v'(\gamma a) & \frac{\beta v}{a\gamma^2}K_v(\gamma a) \end{pmatrix}. \tag{2.21}$$

To get a nontrivial solution for $\begin{pmatrix} A & A' & C & C' \end{pmatrix}^T$, the determinant of the matrix $[\mathbf{M}]$ is set to zero leading to the characteristic equation

$$\frac{\beta^2 v^2}{a^2}\left[\frac{1}{\gamma^2}+\frac{1}{\kappa^2}\right]^2 = \left[\frac{J_v'(\kappa a)}{\kappa J_v(\kappa a)} + \frac{K_v'(\gamma a)}{\gamma K_v(\gamma a)}\right]\cdot\left[\frac{k_0^2 n_1^2 J_v'(\kappa a)}{\kappa J_v(\kappa a)} + \frac{k_0^2 n_2^2 K_v'(\gamma a)}{\gamma K_v(\gamma a)}\right], \tag{2.22}$$

known as the dispersion equation. For any wavelength λ and integer v, the only unknown in Eq. 2.22 is β, which is found by solving Eq. 2.22 numerically or graphically.

To completely determine the field distribution, the coefficients A, A', C, and C' must be specified. When the determinant of $[\mathbf{M}]$ is zero, the coefficients A', C, and C' in Eq. 2.20 are expressed in terms of A. The coefficients C and C' have unique expressions given by

$$C = \frac{J_v(\kappa a)}{K_v(\gamma a)}A, \tag{2.23}$$

$$C' = \frac{J_v(\kappa a)}{K_v(\gamma a)}A', \tag{2.24}$$

but the coefficient A' can be expressed by either

$$A' = \frac{j\beta v}{\omega\mu a} \frac{\left[\frac{1}{\gamma^2} + \frac{1}{\kappa^2}\right]}{\left[\frac{J'_v(\kappa a)}{\kappa J_v(\kappa a)} + \frac{K'_v(\gamma a)}{\gamma K_v(\gamma a)}\right]]} A \tag{2.25}$$

which corresponds to E_ϕ continuity leading to EH modes for which $A' > A$, or

$$A' = \frac{j\omega a}{\beta v} \frac{\left[\frac{k_0^2 n_1^2 J'_v(\kappa a)}{\kappa J_v(\kappa a)} + \frac{k_0^2 n_2^2 K'_v(\gamma a)}{\gamma K_v(\gamma a)}\right]}{\left[\frac{1}{\gamma^2} + \frac{1}{\kappa^2}\right]} A \tag{2.26}$$

which corresponds to H_ϕ continuity leading to HE modes for which $A' < A$. Setting A to an arbitrary value such as $A = 1$ specifies the coefficients A', C, and C' and the field distribution for both HE and EH modes are calculated using Eq. 2.17 and Eq. 2.18.

Figure 2.2 presents the calculated electric field components E_r, E_ϕ, and E_z for a hybrid microwire with an As_2Se_3 core refractive index $n_1 = 2.83$, a PMMA cladding refractive index $n_2 = 1.463$, and a core diameter of 0.45 µm at $\lambda = 1550$ nm. The radial field component E_r is discontinuous at the core/cladding interface due to the large refractive index difference between the core and the cladding; therefore, any analysis based on the weak guiding approximation is not accurate. Moreover, the longitudinal field component E_z has the same order of magnitude as both the radial component E_r and the angular component E_ϕ; therefore, any analysis based on the scalar field approximation is not accurate and the vectorial nature of the field must be considered.

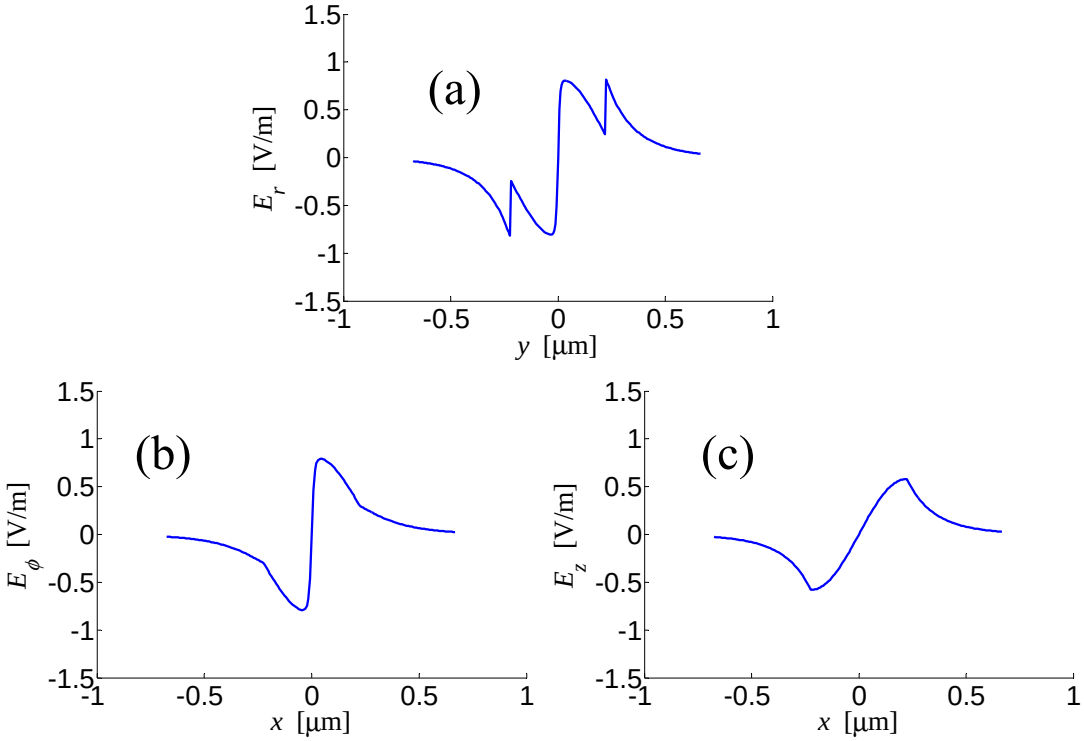

Fig. 2.2 The distribution of a) E_r, b) E_ϕ, and c) E_z for the mode HE_{11} in a microwire with $n_1 = 2.83$, $n_2 = 1.463$, and $a = 0.225$ µm at $\lambda = 1550$ nm.

2.2 Microwire Parameters

The microwire parameters of interest are chromatic dispersion, waveguide nonlinearity and losses. These parameters are essential for the study of nonlinear pulse propagation in microwires. These parameters can be engineered for linear and nonlinear applications by changing the microwire structures and geometrical dimensions such as the core diameter.

Chromatic Dispersion

Determination of the chromatic dispersion (D_c) and the waveguide nonlinearity involves solving Eq 2.22 to obtain the propagation constant β as a function of λ for the fundamental mode HE_{11}. Solving the characteristic equation takes into account the wavelength dependence of the refractive indices of the core and the cladding obtained from the Sellmier

relation [71]

$$n^2(\lambda) = 1 + \sum_{i=1}^{i=3} A_i^2 \lambda^2 / \left(\lambda^2 - \lambda_i^2\right),$$

or equivalently, from the Cauchy relation [71]

$$n^2 = B_1 + B_2\lambda^2 + B_3\lambda^{-2} + B_4\lambda^{-4} + B_5\lambda^{-6} + B_6\lambda^{-8}.$$

The chromatic dispersion is calculated using [9]

$$D_c = \frac{-\lambda}{c}\frac{d^2 n_{eff}}{d\lambda^2}, \tag{2.27}$$

where $n_{eff} = \beta/k_0$ with k_0 being the wavenumber.

Waveguide Nonlinearity

Using scalar analysis as described in [9], the value of γ is calculated using

$$\gamma = k_0 n_2 / A_{eff} \tag{2.28}$$

with n_2 being the material nonlinearity where A_{eff} is the effective area given by

$$A_{eff} = \frac{\left[\int\int_{-\infty}^{\infty} |F(x,y)|^2 \, dxdy\right]^2}{\int\int_{-\infty}^{\infty} |F(x,y)|^4 \, dxdy} \tag{2.29}$$

and k_0 is the wavenumber and $F(x,y)$ is the scalar electric field distribution. However, it has been shown in Section 2.1 that the scalar field approximation is not accurate for microwires and the vectorial nature of the field must be considered. The first analytical formulation of the waveguide nonlinearity using the vector electric field distribution $\overrightarrow{E}$, and the vector magnetic field distribution $\overrightarrow{H}$ of the fundamental mode HE_{11} in microwires has been presented by Tzolov et al. [72, 73]. The difference of material composition between the core and cladding of the microwire has been included in the calculation of γ by Foster et al. [74]. A formula for γ accounting for both the vectorial field distribution and the

different material composition of the microwire has been presented in [75] and is given by

$$\gamma = k_0 \bar{n}_2 / A_{eff} \tag{2.30}$$

with $\bar{n}_2$ being the effective material nonlinearity given by [75, 76]

$$\bar{n}_2 = \frac{\varepsilon_0}{\mu_0} \frac{\iint_\infty n_0^2(x,y)\, n_2(x,y) \left(2\left|\vec{E}\right|^4 + \left|\vec{E}^2\right|^2 \right) dA}{3 \iint_\infty \left| \left[\vec{E} \times \vec{H}^* \right] \cdot \hat{z} \right|^2 dA}, \tag{2.31}$$

and A_{eff} given by [75, 76]

$$A_{eff} = \frac{\left| \iint_\infty \left[\vec{E} \times \vec{H}^* \right] \cdot \hat{z} dA \right|^2}{\iint_\infty \left| \left[\vec{E} \times \vec{H}^* \right] \cdot \hat{z} \right|^2 dA}, \tag{2.32}$$

where n_0 is the refractive index, n_2 is the material nonlinearity, $\overrightarrow{E}$ and $\overrightarrow{H}$ are calculated using Eq. 2.14, Eq. 2.15, Eq. 2.17, and Eq. 2.18, ε_0 and μ_0 are the electric permittivity and the magnetic permeability of free space, respectively, z is the direction of propagation and A is the transverse surface area.

Material Loss

Losses in microwires can arise from the material losses and roughness of the surface of the microwires. Material losses in a microwire depend on both material absorption and Rayleigh scattering [9]. The estimation of the material losses in a microwire must take into account the difference of material composition between the core and the cladding. Material losses in a microwire are calculated using

$$\alpha_{hybrid}^{dB} = \Gamma_{core} \times \alpha_{core}^{dB} + \Gamma_{clad} \times \alpha_{clad}^{dB}, \tag{2.33}$$

where $\Gamma_i = P_i / P_{tot}$ is the confinement factor with P_i being the power fraction of the mode in layer i and P_{tot} the total power of the mode [77].

2.3 Tangential Vector Finite-Element Method

Advanced fiber microwires structures with a finite cladding diameter, an eccentric core, or multiple cores are analyzed using numerical methods such as the finite-difference method [78], the boundary-integral method [79], the eigenfunction expansion method [44], and the finite-element method [80–82]. Full vector field analysis is required in fiber waveguides with composite structures and sub-wavelength dimensions because scalar field approximation is not accurate. Vectorial finite-element methods have been developed to find vector field distributions in fiber waveguides; however, these methods give rise to "spurious solutions" corresponding to non-physical solutions where the calculated field amplitude does not converge to zero as $r \to \infty$ [82]. Spurious solutions arise because continuity of tangential components of the electric field at the element edges is not enforced.

A tangential finite-element method, based on "edge elements", has been used to eliminate spurious solutions that result from vector finite-element methods. In this method, a combination of scalar and vector basis functions are used to represent the vector field distribution in an element, and the unknowns are the tangential component and the longitudinal z-component of the electric field. In this section, we present the tangential vector finite-element method for analysis subwavelength fiber waveguides.

Domain Discretization

Figure 2.3 presents a schematic of a triangular element used for the discretization of the waveguide structure. The nodes n_i with $i \in \{1, 2, 3\}$ on the elements are numbered in anti-clockwise orientation, and the edges e_{ti} with $i \in \{1, 2, 3\}$ in each element are numbered as illustrated in Fig. 2.3. An open source mesh generator is used to construct a mesh representing the fiber waveguides under study [83]. Figure 2.4 presents a sample mesh generated for a microwire with a finite cladding.

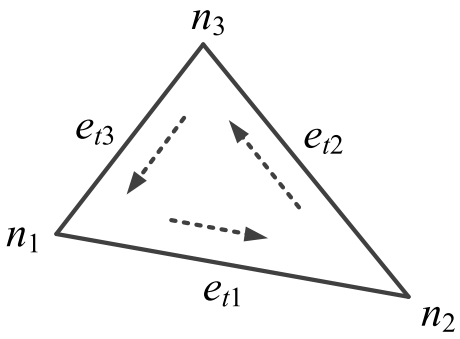

Fig. 2.3 Schematic of a triangular element.

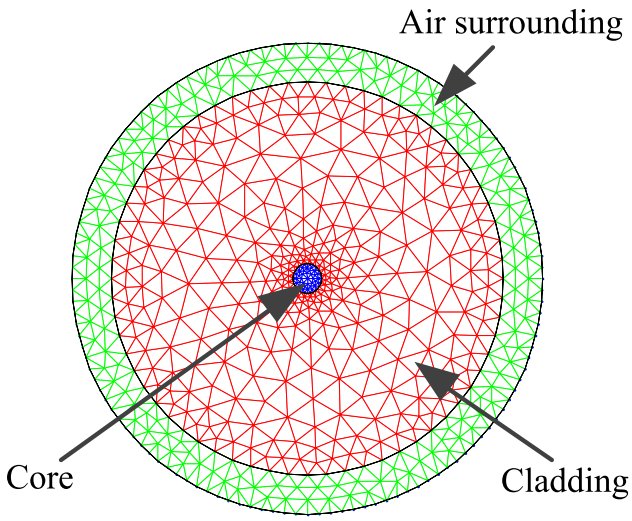

Fig. 2.4 Mesh sample for a microwire with a finite cladding.

First-order interpolation functions are used to approximated the electric field within each element; therefore, capturing the details of the field distribution requires increased density of the triangular elements in and around the core to guarantee adequate representation of the electric field distribution. Larger elements can be used away from the core because the electric field distribution has smoother changes; however, according to the sampling theorem, the lengths of the edges of all the triangular elements must be shorter than half the wavelength of the electromagnetic wave propagating in the microwire so that the finite-element analysis is able to detect modes at that wavelength. In fact, the longest edge

length of all the triangular elements must be sufficiently shorter than half the wavelength to obtain precise solutions of the field distribution. Moreover, the boundary of the mesh is assumed to be a perfect conductor such that the electric field at the outer boundary edges of the mesh is zero. Therefore, obtaining a precise mode solution requires the mesh boundary to be placed such that the electric field can be approximated to be zero.

Variational Formulation

The boundary value problem for a waveguide is given by

$$\nabla \times \left(\frac{1}{\mu_r} \nabla \times \vec{E} \right) - k_0^2 \varepsilon_r \vec{E} = 0$$

in Ω and the boundary condition

$$\hat{n} \times \vec{E} = 0$$

on Γ_1, and

$$\hat{n} \times \left(\nabla \times \vec{E} \right) = 0$$

on Γ_2, where Ω is the cross section region and the boundary of the cross section is $\Gamma = \Gamma_1 \bigcup \Gamma_2$ [82]. The equivalent variational problem is $\delta F(\vec{E}) = 0$, and $\hat{n} \times \vec{E} = 0$ on Γ_1 where

$$F(\vec{E}) = \frac{1}{2} \iint_{\Omega} \left[\frac{1}{\mu_r} \left(\nabla \times \vec{E} \right) . \left(\nabla \times \vec{E} \right)^* - k_0^2 \varepsilon_r \vec{E} . \vec{E}^* \right] d\Omega$$

given that ε_r and μ_r are real. Using $\vec{E}(x, y, z) = \vec{E}(x, y) e^{-jk_z z}$ with $\vec{E}(x, y) = \vec{E}_t(x, y) + E_z(x, y)\hat{k}$ and $\vec{E}_t(x, y) = E_x(x, y)\hat{i} + E_y(x, y)\hat{j}$, the expression $\vec{E}.\vec{E}^*$ becomes $\vec{E}.\vec{E}^* = \vec{E}_t.\vec{E}_t^* + E_z.E_z^*$, and the product $\left(\nabla \times \vec{E} \right) . \left(\nabla \times \vec{E} \right)^*$ becomes

$$\left(\nabla \times \vec{E} \right) . \left(\nabla \times \vec{E} \right)^* = \left[\nabla_t E_z + j k_z E_t \right] \left[\nabla_t E_z + j k_z E_t \right]^* + \left(\nabla_t \times \vec{E}_t \right) \left(\nabla_t \times \vec{E}_t \right)^*$$

where

$$\nabla_t \times \vec{E}_t = \begin{vmatrix} \frac{\partial}{\partial x} & \frac{\partial}{\partial y} \\ E_x & E_y \end{vmatrix} \hat{k}$$

leading to a new form for the functional given by

$$F(\vec{E}) = \frac{1}{2}\iint_{\Omega}\left[\begin{array}{l}\frac{1}{\mu_r}\left(\nabla_t\times\vec{E}_t\right).\left(\nabla_t\times\vec{E}_t\right)^* - k_0^2\varepsilon_r\vec{E}_t.\vec{E}_t^* \\ \quad +\frac{1}{\mu_r}\left(\nabla_t E_z + jk_z\vec{E}_t\right).\left(\nabla_t E_z + jk_z\vec{E}_t\right)^* - k_0^2\varepsilon_r E_z.E_z^*\end{array}\right]d\Omega.$$

Using the substitution $\vec{e}_t = k_z\vec{E}_t$ and $e_z = -jE_z$ the functional becomes

$$F(\vec{e}) = \frac{1}{2}\iint_{\Omega}\left\{\begin{array}{l}\frac{1}{\mu_r}\left(\nabla_t\times\vec{e}_t\right).\left(\nabla_t\times\vec{e}_t\right)^* - k_0^2\varepsilon_r\vec{e}.\vec{e}^* \\ \quad +k_z^2\left[\frac{1}{\mu_r}\left(\nabla_t e_z + \vec{e}_t\right).\left(\nabla_t e_z + \vec{e}_t\right)^* - k_0^2\varepsilon_r e_z e_z^*\right]\end{array}\right\}d\Omega.$$

Basis Functions

The first order interpolation expansion functions inside each element are given in terms of the coordinates (x_i, y_i) of node n_i with $i \in \{1,2,3\}$ by the relation [82]

$$L_i = \frac{1}{2\Delta^e}\left(a_i + b_i x + c_i y\right)$$

where the coefficients a_i, b_i, and c_i are given by

$$\begin{array}{lll} a_1 = x_2y_3 - y_2x_3 & b_1 = y_2 - y_3 & c_1 = x_3 - x_2 \\ a_2 = x_3y_1 - y_2x_1 & b_2 = y_3 - y_1 & c_2 = x_1 - x_3 \\ a_3 = x_1y_2 - y_1x_2 & b_3 = y_1 - y_2 & c_1 = x_2 - x_1 \end{array}$$

and the area of the triangular element Δ^e is given by

$$\Delta^e = \frac{1}{2}\begin{vmatrix} 1 & x_1 & y_1 \\ 1 & x_2 & y_2 \\ 1 & x_3 & y_3 \end{vmatrix} = \frac{1}{2}\left(b_1c_2 - b_2c_1\right).$$

Scalar basis functions $N_i = L_i$ is defined inside an element e for each node i and the z-component of the electric field is given by

$$e_z = \sum_{i=1}^{3} N_i^e e_{zi}^e = \left\{N^e\right\}^T\left\{e_z^e\right\} = \left\{e_z^e\right\}^T\left\{N^e\right\}. \tag{2.34}$$

Vector basis functions $\vec{N}_k = l_k\left(L_i\nabla L_j - L_j\nabla L_i\right)$ are defined inside an element for each

edge k connecting node i to node j, where l_k is the length of the edge e_{tk} and $\nabla L_i = (1/2\Delta^e)\left(b_i\hat{i} + c_i\hat{j}\right)$. These vector basis functions satisfy the following identities [82]:

$$\vec{\nabla}.\vec{N}_k = 0,$$

$$\vec{\nabla} \times \vec{N}_k = \frac{l_k}{\Delta^e}\hat{k},$$

$$\vec{e}_k.\vec{N}_k = 1.$$

The electric field component in the plane of the cross-section of the fiber waveguide is expressed in terms of the vector basis function as

$$\vec{e}_t = \sum_{i=1}^{3} \vec{N}_i^e e_{ti}^e = \left\{\vec{N}^e\right\}^T \left\{e_t^e\right\} = \left\{e_t^e\right\}^T \left\{\vec{N}^e\right\}. \tag{2.35}$$

The Ritz Formulation

Using $e_z = \left\{e_z^e\right\}^T \left\{N^e\right\}$ and $\vec{e}_t = \left\{e_t^e\right\}^T \left\{\vec{N}^e\right\}$, the functional becomes

$$F(\vec{e}) = \sum_e F^e\left(\vec{e}\right)$$

where $F^e\left(\vec{e}\right)$ is the functional integral within element e with

$$F^e(\vec{e}) = \sum_{i=1}^{n}\sum_{j=1}^{n} \left\{ \begin{array}{l} \frac{1}{2}\iint_{\Omega^e}\left[\frac{1}{\mu_r^e}\left(\nabla_t \times \vec{N}_i^e\right).\left(\nabla_t \times \vec{N}_j^e\right) - k_0^2\varepsilon_r\left(\vec{N}_i^e\right).\left(\vec{N}_j^e\right)\right] d\Omega\ e_{ti}^e e_{tj}^{e*} \\ +k_z^2 \left[\begin{array}{l} \frac{1}{2}\iint_{\Omega^e}\left[\frac{1}{\mu_r}\left(\vec{N}_i^e\right).\left(\vec{N}_j^e\right)\right] d\Omega\ e_{ti}^e e_{tj}^{e*} \\ +\frac{1}{2}\iint_{\Omega^e}\left[\frac{1}{\mu_r}\left(\vec{N}_i^e\right).\left(\nabla_t N_j^e\right)\right] d\Omega\ e_{ti}^e e_{zj}^{e*} \\ +\frac{1}{2}\iint_{\Omega^e}\left[\frac{1}{\mu_r}\left(\nabla_t N_i^e\right).\left(\vec{N}_j^e\right)\right] d\Omega\ e_{zi}^e e_{tj}^{e*} \\ +\frac{1}{2}\iint_{\Omega^e}\left[\frac{1}{\mu_r}\left(\nabla_t N_i^e\right).\left(\nabla_t N_j^e\right) - k_0^2\varepsilon_r\left(N_i^e\right)\left(N_j^e\right)\right] d\Omega\ e_{zi}^e e_{zj}^{e*} \end{array} \right] \end{array} \right\}.$$

The field distribution over the entire domain Ω is obtained when

$$\frac{\partial}{\partial Re\{e_{tk}\}}F(\vec{e}) + j\frac{\partial}{\partial Im\{e_{tk}\}}F(\vec{e}) = 0$$

$$\frac{\partial}{\partial Re\{e_{zk}\}}F(\vec{e}) + j\frac{\partial}{\partial Im\{e_{zk}\}}F(\vec{e}) = 0$$

leading to the global eigenvalue equation

$$\begin{bmatrix} A_{tt} & 0 \\ 0 & 0 \end{bmatrix} \begin{Bmatrix} e_t \\ e_z \end{Bmatrix} = k_z^2 \begin{bmatrix} B_{tt} & B_{tz} \\ B_{zt} & B_{zz} \end{bmatrix} \begin{Bmatrix} e_t \\ e_z \end{Bmatrix}$$

Using $[B_{zt}]\{e_t\} - k_z^2 [B_{zz}]\{e_z\} = 0$, the eigenvalue equation reduces to

$$[A_{tt}]\{e_t\} = k_z^2 [B'_{tt}]\{e_t\}$$

where $[B'_{tt}] = [B_{tz}][B_{zz}]^{-1}[B_{zt}] - [B_{tt}]$. The global matrices $[A_{tt}]$, $[B_{tt}]$, $[B_{tz}]$, $[B_{zt}]$, and $[B_{zz}]$ are calculated from the element matrices $[A^e_{tt}]$, $[B^e_{tt}]$, $[B^e_{tz}]$, $[B^e_{zt}]$, and $[B^e_{zz}]$ given by

$$[A^e_{tt}] = \iint_{\Omega^e} \left\{ \tfrac{1}{\mu^e_r} \left\{ \nabla_t \times \vec{N}^e \right\} . \left\{ \nabla_t \times \vec{N}^e \right\}^T - k_0^2 \varepsilon^e_r \left\{ \vec{N}^e \right\} . \left\{ \vec{N}^e \right\}^T \right\} d\Omega$$

$$[B^e_{tt}] = \iint_{\Omega^e} \tfrac{1}{\mu^e_r} \left\{ \vec{N}^e \right\} . \left\{ \vec{N}^e \right\}^T d\Omega$$

$$[B^e_{tz}] = \iint_{\Omega^e} \tfrac{1}{\mu^e_r} \left\{ \vec{N}^e \right\} . \{\nabla_t N^e\}^T d\Omega$$

$$[B^e_{zt}] = \iint_{\Omega^e} \tfrac{1}{\mu^e_r} \{\nabla_t N^e\} . \left\{ \vec{N}^e \right\}^T d\Omega$$

$$[B^e_{zz}] = \iint_{\Omega^e} \left[\tfrac{1}{\mu^e_r} \{\nabla_t N^e\} . \{\nabla_t N^e\}^T - k_0^2 e^e_r \left\{ \vec{N}^e \right\} \left\{ \vec{N}^e \right\}^T \right] d\Omega$$

where

$$A^e_{tt}(i,j) = \iint_{\Omega^e} \left[\tfrac{1}{\mu^e_r} \left(\nabla_t \times \vec{N}^e_i \right) . \left(\nabla_t \times \vec{N}^e_j \right) - k_0^2 \varepsilon^e_r \vec{N}^e_i . \vec{N}^e_j \right] d\Omega$$

$$B^e_{tt}(i,j) = \iint_{\Omega^e} \tfrac{1}{\mu^e_r} \vec{N}^e_i . \vec{N}^e_j d\Omega$$

$$B^e_{tz}(i,j) = \iint_{\Omega^e} \tfrac{1}{\mu^e_r} \vec{N}^e_i . \nabla_t N^e_j d\Omega$$

$$B^e_{zt}(i,j) = \iint_{\Omega^e} \tfrac{1}{\mu^e_r} \nabla_t N^e_i . \vec{N}^e_j . d\Omega$$

$$B^e_{zz}(i,j) = \iint_{\Omega^e} \left[\tfrac{1}{\mu^e_r} \left(\nabla_t N^e_i \right) . \left(\nabla_t N^e_j \right) - k_0^2 \varepsilon^e_r N^e_i N^e_j \right] d\Omega$$

are the components of the element matrices.

Algebraic Expressions for the Element Matrices

The components of the element matrices can be calculated using simple algebraic expressions [82]. Using the identity $\vec{\nabla} \times \vec{N}_k = (l_k/\Delta^e)\,\hat{k}$ and defining the integral $F_{ij} =$

$\iint_{\Omega^e} \vec{N}_i^e . \vec{N}_j^e d\Omega$ that is algebraically calculated using

$$\begin{aligned}
F_{11} &= \frac{\left(l_1^e\right)^2}{24\Delta^e}\left(f_{22} - f_{12} + f_{11}\right) \\
F_{12} = F_{21} &= \frac{l_1^e l_2^e}{48\Delta^e}\left(f_{23} - f_{22} - 2f_{13} + f_{12}\right) \\
F_{13} = F_{31} &= \frac{l_1^e l_3^e}{48\Delta^e}\left(f_{21} - 2f_{23} - f_{11} + f_{13}\right) \\
F_{22} &= \frac{\left(l_2^e\right)^2}{24\Delta^e}\left(f_{33} - f_{23} + f_{22}\right) \\
F_{23} = F_{32} &= \frac{l_2^e l_3^e}{48\Delta^e}\left(f_{31} - f_{33} - 2f_{21} + f_{23}\right) \\
F_{33} &= \frac{\left(l_3^e\right)^2}{24\Delta^e}\left(f_{11} - f_{13} + f_{33}\right)
\end{aligned}$$

where $f_{ij} = b_i^e b_j^e + c_i^e c_j^e$, the value of $A_{tt}^e(i,j)$ is

$$A_{tt}^e(i,j) = \frac{l_i^e l_j^e}{\mu_r^e \Delta^e} - k_0^2 \varepsilon_r^e F_{ij}.$$

Also, $B_{tt}^e(i,j)$ is calculated using the

$$B_{tt}^e(i,j) = \frac{1}{\mu_r^e} F_{ij}.$$

Using the identity $\iint_{\Omega^e} N_i d\Omega = \Delta^e/3$, the element matrix component $B_{tz}^e(i,j)$ is calculated using the following equations:

$$\begin{aligned}
B_{tz}^e(1,1) &= \tfrac{1}{12\mu_r^e\Delta^e} l_1 \left[f_{21} - f_{11}\right] \\
B_{tz}^e(1,2) &= \tfrac{1}{12\mu_r^e\Delta^e} l_1 \left[f_{22} - f_{12}\right] \\
B_{tz}^e(1,3) &= \tfrac{1}{12\mu_r^e\Delta^e} l_1 \left[f_{23} - f_{13}\right]
\end{aligned}$$

$$\begin{aligned}
B_{tz}^e(2,1) &= \tfrac{1}{12\mu_r^e\Delta^e} l_2 \left[f_{31} - f_{21}\right] \\
B_{tz}^e(2,2) &= \tfrac{1}{12\mu_r^e\Delta^e} l_2 \left[f_{32} - f_{22}\right] \\
B_{tz}^e(2,3) &= \tfrac{1}{12\mu_r^e\Delta^e} l_2 \left[f_{33} - f_{23}\right]
\end{aligned}$$

$$\begin{aligned}
B_{tz}^e(3,1) &= \tfrac{1}{12\mu_r^e\Delta^e} l_3 \left[f_{11} - f_{31}\right] \\
B_{tz}^e(3,2) &= \tfrac{1}{12\mu_r^e\Delta^e} l_3 \left[f_{12} - f_{32}\right] \\
B_{tz}^e(3,3) &= \tfrac{1}{12\mu_r^e\Delta^e} l_3 \left[f_{13} - f_{33}\right].
\end{aligned}$$

The value of $B^e_{zt}(i,j)$ is algebraically calculated using the following equations:

$$\begin{aligned}
B^e_{zt}(1,1) &= \tfrac{l_1}{12\mu^e_r\Delta^e}\left[f_{12}-f_{11}\right]\\
B^e_{zt}(1,2) &= \tfrac{l_2}{12\mu^e_r\Delta^e}\left[f_{13}-f_{12}\right]\\
B^e_{zt}(1,3) &= \tfrac{l_3}{12\mu^e_r\Delta^e}\left[f_{11}-f_{13}\right]
\end{aligned}$$

$$\begin{aligned}
B^e_{zt}(2,1) &= \tfrac{l_1}{12\mu^e_r\Delta^e}\left[f_{22}-f_{21}\right]\\
B^e_{zt}(2,2) &= \tfrac{l_2}{12\mu^e_r\Delta^e}\left[f_{23}-f_{22}\right]\\
B^e_{zt}(2,3) &= \tfrac{l_3}{12\mu^e_r\Delta^e}\left[f_{21}-f_{23}\right]
\end{aligned}$$

$$\begin{aligned}
B^e_{zt}(3,1) &= \tfrac{l_1}{12\mu^e_r\Delta^e}\left[f_{32}-f_{31}\right]\\
B^e_{zt}(3,2) &= \tfrac{l_2}{12\mu^e_r\Delta^e}\left[f_{33}-f_{32}\right]\\
B^e_{zt}(3,3) &= \tfrac{l_3}{12\mu^e_r\Delta^e}\left[f_{31}-f_{33}\right]
\end{aligned}$$

Finally, using equation $\iint_{\Omega^e} N^e_i N^e_j d\Omega = \left(\Delta^e/12\right)\left(1+\delta_{ij}\right)$ where

$$\delta_{ij} = \begin{cases} 1 & \text{when } \; i=j \\ 0 & \text{when } \; i\neq j \end{cases}$$

and using $\left(\nabla_t N^e_i\right)\cdot\left(\nabla_t N^e_j\right) = \left(2\Delta^e\right)^{-2} f_{ij}$ leads to

$$B^e_{zz}(i,j) = \left[\frac{1}{4\Delta^e\mu^e_r}f_{ij} - k_0^2\varepsilon^e_r\frac{\Delta^e}{12}(1+\delta_{ij})\right].$$

The element matrices $[A^e_{tt}]$, $[B^e_{tt}]$, $[B^e_{tz}]$, $[B^e_{zt}]$, and $[B^e_{zz}]$ are algebraically calculated and used to construct the global matrices $[A_{tt}]$, $[B_{tt}]$, $[B_{tz}]$, $[B_{zt}]$, and $[B_{zz}]$. The global matrices are used to solve the eigenvalue equation to obtain the propagation constant k_z and the unknowns e^e_t and e^e_z for every mode sustained in the fiber. The field distribution $\vec{E}_t$ and E_z are calculated from the unknowns e^e_t and e^e_z using

$$\vec{E}_t = \frac{1}{k_z}\vec{e}_t = \frac{1}{k_z}\left\{e^e_t\right\}^T\left\{\vec{N}^e\right\},$$

$$E_z = je_z = \left\{e^e_z\right\}^T\left\{N^e\right\}.$$

The finite-element method is used to analyze an infinite cladding hybrid microwire with an As_2Se_3 core refractive index of $n_1 = 2.83$, a PMMA cladding refractive index of $n_2 =$

1.463, and a core diameter of 0.45 µm at $\lambda = 1550$ nm. The calculated effective refractive index of the fundamental mode of the microwire is $n_{eff}^{FEM} = 1.961529$ is in close agreement with the exact value of $n_{eff}^{Exact} = 1.964285$ obtained using the step-index fiber waveguide analysis presented in Section 2.1. Figure 2.5 presents the E_z distribution calculated using both the tangential vector finite-element method and the analysis in Section 2.1.

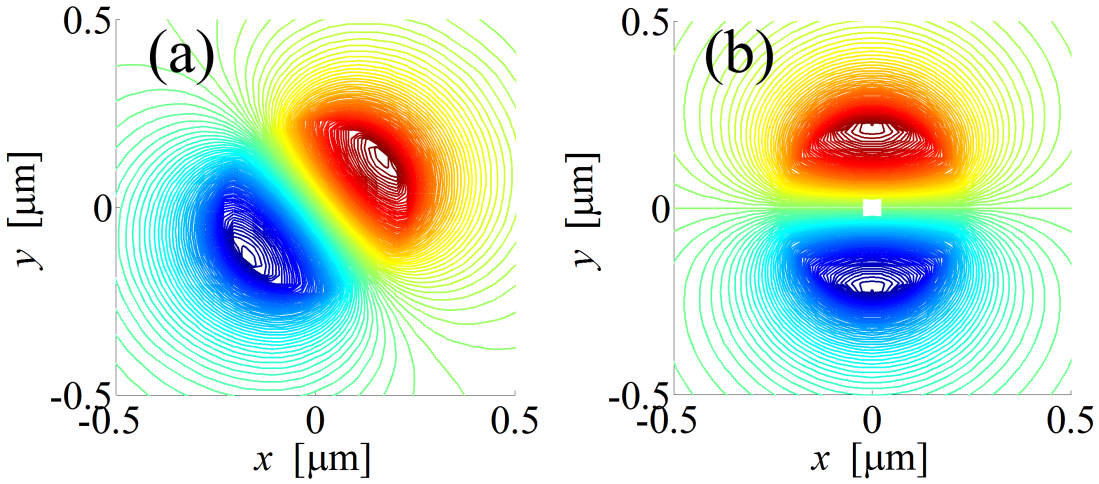

Fig. 2.5 Calculated E_z distribution for the mode HE_{11} in a microwire with $n_1 = 2.83$, $n_2 = 1.463$, and $a = 0.225$ µm at $\lambda = 1550$ nm using a) the tangential vector finite-element method and b) the exact analytical solution presented in Section 2.1.

2.4 Pulse Propagation Equation

This section presents the derivation of the nonlinear Schrodinger equation that is used to describe pulse propagation in nonlinear fiber structures. The Maxwell equations in the frequency domain are obtained by taking the Fourier transform of Eq. 2.1 and Eq. 2.2 to obtain

$$\nabla \times \vec{E} = -j\mu_0 \omega \vec{H}\left(\vec{r}, \omega\right) \tag{2.36}$$

$$\nabla \times \vec{H} = j\varepsilon_0 \omega \vec{E}\left(\vec{r}, \omega\right) + j\omega \vec{P}\left(\vec{r}, \omega\right) \tag{2.37}$$

where the Fourier transform is defined as

$$f\left(\vec{r}, \omega\right) = \int f\left(\vec{r}, t\right) e^{-j\omega t} d\omega,$$

$$f(\vec{r},t) = \frac{1}{2\pi}\int f(\vec{r},\omega)\, e^{j\omega t} d\omega.$$

Using the polarization expansion

$$\vec{P}(\vec{r},\omega) = \vec{P}_L(\vec{r},\omega) + \vec{P}_{NL}(\vec{r},\omega)$$

where

$$\vec{P}_L(\vec{r},\omega) = \chi^{(1)}\vec{E}(\vec{r},\omega)$$

and $\vec{P}_{NL}$ is a nonlinear polarization perturbation satisfying $\left|\vec{P}_{NL}(\vec{r},\omega)\right| \ll \left|\vec{P}_L(\vec{r},\omega)\right|$, Eq. 2.36 and Eq. 2.37 become

$$\nabla \times \vec{E} = -j\mu_0\omega\vec{H}(\vec{r},\omega) \tag{2.38}$$

$$\nabla \times \vec{H} = j\varepsilon_0 n^2(\vec{r},\omega)\,\omega\vec{E}(\vec{r},\omega) + j\omega\vec{P}_{NL}(\vec{r},\omega) \tag{2.39}$$

where $n^2(\vec{r},\omega) = 1 + \chi^{(1)}$.

Perturbation Analysis

The perturbed and unperturbed fields are related using the reciprocal theorem [73, 75]

$$\frac{\partial}{\partial z}\int \vec{F}_C.\hat{z}dA = \int \nabla\cdot\vec{F}_C dA \tag{2.40}$$

where

$$\vec{F}_C = \vec{E}_0 \times \vec{H}^* + \vec{E}^* \times \vec{H}_0. \tag{2.41}$$

where $\vec{E}$, $\vec{H}$ represent the perturbed field, and $\vec{E}_0$, $\vec{H}_0$ represent the unperturbed field. The perturbed and unperturbed fields are expressed as

$$\vec{E}(\vec{r},\omega) = a(z,\omega)\,\hat{e}(x,y,\omega) \tag{2.42}$$

$$\vec{H}(\vec{r},\omega) = a(z,\omega)\,\hat{h}(x,y,\omega) \tag{2.43}$$

$$\vec{E}_0(\vec{r},\omega_0) = \hat{e}(x,y,\omega_0) \tag{2.44}$$

$$\vec{H}_0(\vec{r},\omega_0) = \hat{h}(x,y,\omega_0) \tag{2.45}$$

where $a(z,\omega)$ is the field envelope,

$$\hat{e} = \frac{\vec{e}(x,y,\omega)}{\sqrt{N}} e^{j\beta z} \tag{2.46}$$

$$\hat{h} = \frac{\vec{h}(x,y,\omega)}{\sqrt{N}} e^{j\beta z} \tag{2.47}$$

with

$$N = \frac{1}{2}\left| \int \left[\vec{e}(x,y,\omega) \times \vec{h}^{*}(x,y,\omega) \right] \cdot \hat{z} dA \right|, \tag{2.48}$$

$\vec{e}$ and $\vec{h}$ are the electric and magnetic vector field distributions of the fundamental mode, and β is the propagation constant of the fundamental mode.

Using Eq. 2.42, Eq. 2.43, Eq. 2.44, and Eq. 2.45 with the approximations $\hat{e}(x,y,\omega) = \hat{e}(x,y,\omega_0)$ and $\hat{h}(x,y,\omega) = \hat{h}(x,y,\omega_0)$, the product $\vec{F}_C \cdot \hat{z}$ becomes

$$\vec{F}_C.\hat{z} = a^{*}(z,\omega) \left[\left(\hat{e} \times \hat{h}^{*} \right) \cdot \hat{z} + \left(\hat{e}^{*} \times \hat{h} \right) \cdot \hat{z} \right]$$

which leads to

$$\frac{\partial}{\partial z} \int \vec{F}_C.\hat{z} dA = 4 \frac{\partial a^{*}(z,\omega)}{\partial z}. \tag{2.49}$$

Using the product rule $\nabla \cdot (\vec{u} \times \vec{v}) = \vec{v} \cdot (\nabla \times \vec{u}) - \vec{u} \cdot (\nabla \times \vec{v})$, the term $\nabla \cdot \vec{F}_C$ is expressed as

$$\nabla \cdot \vec{F}_C = \vec{H}^{*} \cdot \left(\nabla \times \vec{E}_0 \right) - \vec{E}_0 \cdot \left(\nabla \times \vec{H} \right)^{*} + \vec{H}_0 \cdot \left(\nabla \times \vec{E} \right)^{*} - \vec{E}^{*} \cdot \left(\nabla \times \vec{H}_0 \right),$$

and with the application of Eq. 2.38 and Eq. 2.39, the term $\nabla \cdot \vec{F}_C$ becomes

$$\nabla \cdot \vec{F}_C = j\mu_0 (\omega - \omega_0) \vec{H}^{*} \cdot \vec{H}_0 + j\varepsilon_0 \left[n^2(\vec{r},\omega)\omega - n^2(\vec{r},\omega_0)\omega_0 \right] \vec{E}^{*} \cdot \vec{E}_0 + j\omega \vec{E}_0 \cdot \vec{P}_{NL}{}^{*}(\vec{r},\omega).$$

The use of Eq. 2.42, Eq. 2.43, Eq. 2.44, and Eq. 2.45 with the approximations $\hat{e}(x,y,\omega) =$

$\hat{e}(x,y,\omega_0)$ and $\hat{h}(x,y,\omega) = \hat{h}(x,y,\omega_0)$ leads to

$$\begin{aligned}\nabla \cdot \vec{F}_C = {} & j\mu_0(\omega-\omega_0)\, a^*(z,\omega)\, \hat{h}^* \cdot \hat{h} \\ & + j\varepsilon_0 \left[n^2(\vec{r},\omega)\,\omega - n^2(\vec{r},\omega_0)\,\omega_0\right] a^*(z,\omega)\, \hat{e}^* \cdot \hat{e} \\ & + j\omega \hat{e} \cdot \vec{P}_{NL}{}^*(\vec{r},\omega)\,.\end{aligned}$$

and the integral $\int \nabla \cdot \vec{F}_C dA$ becomes

$$\begin{aligned}\int \nabla \cdot \vec{F}_C dA = {} & j\mu_0(\omega-\omega_0)\, a^*(z,\omega) \int \hat{h}^* \cdot \hat{h} dA \\ & + j\varepsilon_0 a^*(z,\omega) \int \left[n^2(\vec{r},\omega)\,\omega - n^2(\vec{r},\omega_0)\,\omega_0\right] \hat{e}^* \cdot \hat{e} dA \\ & + j\omega \int \hat{e} \cdot \vec{P}_{NL}{}^*(\vec{r},\omega)\, dA.\end{aligned} \tag{2.50}$$

Replacing Eq. 2.49 and Eq. 2.50 in Eq. 2.40 leads to

$$\frac{\partial a(z,\omega)}{\partial z} = -j\frac{1}{4}[C+D]\, a(z,\omega) - j\frac{\omega}{4}\int \hat{e}^* \cdot \vec{P}_{NL}(\vec{r},\omega)\, dA \tag{2.51}$$

where

$$C = \mu_0(\omega-\omega_0)\int \hat{h}\cdot\hat{h}^* dA,$$

$$D = \varepsilon_0 \int \left[n^2(x,y,\omega)\,\omega - n^2(x,y,\omega_0)\,\omega_0\right] \hat{e}\cdot\hat{e}^* dA.$$

The dispersion terms in Eq. 2.51 is expressed as

$$\frac{\partial a(z,\omega)}{\partial z} = -j\sum_{n=1}^{\infty}\left[\frac{(\omega-\omega_0)^n}{n!}\beta^{(n)}\right] a(z,\omega) - j\frac{\omega}{4}\int \hat{e}^* \cdot \vec{P}_{NL}(\vec{r},\omega)\, dA, \tag{2.52}$$

where

$$\beta^{(1)} = \frac{1}{4}\int \left[\mu_0 \hat{h}\cdot\hat{h}^* + \varepsilon_0 \frac{\partial}{\partial\omega}\left(\omega n^2\right)\Big|_{\omega=\omega_0} \hat{e}\cdot\hat{e}^*\right] dA,$$

$$\beta^{(n)} = \frac{\partial^n}{\partial\omega^n}\beta^{(1)}.$$

Taking the inverse Fourier transform of Eq. 2.52 leads to

$$\frac{\partial a(z,t)}{\partial z} = -j\sum_{n=1}^{\infty}\left[\frac{\left(j\frac{\partial}{\partial t}\right)^n}{n!}\beta^{(n)}\right] a(z,t) - j\frac{\omega_0}{4}\left(1+\tau_{shock}\frac{\partial}{\partial t}\right)\int \hat{e}^* \cdot \vec{P}_{NL}(\vec{r},t)\, dA, \tag{2.53}$$

where $\tau_{shock} = j/\omega_0$.

Nonlinear Perturbation

When the Kerr nonlinearity is dominant, the nonlinear polarization is $\vec{P}_{NL}(\vec{r},t) \approx \vec{P}^{(3)}(\vec{r},t)$ with

$$\vec{P}^{(3)}(\vec{r},t) = \frac{3}{4}\varepsilon_0\chi^{(3)}\left|\vec{E}(\vec{r},t)\,\vec{E}(\vec{r},t)\,\vec{E}^{*}(\vec{r},t)\right|,$$

where $\chi^{(3)}$ is a tensor of the fourth rank and | represents tensor multiplication. For isotropic material $\chi^{(3)}$has 81 elements $\chi^{(3)}_{ijkl}$, where $i,j,k,l = \{x,y,z\}$, of which 60 elements are zero and the remaining 21 elements depend on three independent quantities $\chi^{(3)}_{xxyy}$, $\chi^{(3)}_{xyxy}$, and $\chi^{(3)}_{xyyx}$ such that [9]

$$\chi^{(3)}_{ijkl} = \chi^{(3)}_{xxyy}\delta_{ij}\delta_{kl} + \chi^{(3)}_{xyxy}\delta_{ik}\delta_{jl} + \chi^{(3)}_{xyyx}\delta_{il}\delta_{jk},$$

which satisfies the rotation symmetry leading to

$$\chi^{(3)}_{xxxx} = \chi^{(3)}_{yyyy} = \chi^{(3)}_{zzzz} = \chi^{(3)}_{xxyy} + \chi^{(3)}_{xyxy} + \chi^{(3)}_{xyyx}.$$

Hence, the vector components of $\vec{P}^{(3)}(\vec{r},t)$ become

$$P^{(3)}_i(\vec{r},t) = \frac{3}{4}\varepsilon_0\left[\sum_j \chi^{(3)}_{xxyy}E_j{E_j}^{*}E_i + \sum_j \chi^{(3)}_{xyxy}E_j{E_j}^{*}E_i + \sum_j \chi^{(3)}_{xyyx}E_jE_j{E_i}^{*}\right]$$

which can be simplified to [9, 75]

$$\vec{P}^{(3)}(\vec{r},t) = \frac{1}{2}\varepsilon_0\chi^{(3)}_{xxxx}\left[\left(\vec{E}\cdot\vec{E}^{*}\right)\vec{E} + \frac{1}{2}\left(\vec{E}\cdot\vec{E}\right)\vec{E}^{*}\right].$$

Using $\vec{P}_{NL}(\vec{r},t) \approx \vec{P}^{(3)}(\vec{r},t)$, the integration term $\hat{e}^{*}\cdot\vec{P}_{NL}(\vec{r},t)$ becomes

$$\hat{e}^{*}\cdot\vec{P}_{NL}(\vec{r},t) = \frac{3}{4}\varepsilon_0\chi^{(3)}_{xxxx} \times \left(\frac{|a|^2 a}{3N^2}\right)\left[2\left|\vec{e}\right|^4 + \left|\vec{e}^{2}\right|^2\right].$$

Using the relation $(3/4)\,\mathrm{Re}\left\{\chi^{(3)}_{xxxx}\right\} = \varepsilon_0 c n^2 n_2$, Eq. 2.53 becomes

$$\frac{\partial a\,(z,t)}{\partial z} = -j\sum_{n=1}^{\infty}\left[\frac{\left(j\frac{\partial}{\partial t}\right)^n}{n!}\beta^{(n)}\right]a\,(z,t) - j\left(1+\tau_{shock}\frac{\partial}{\partial t}\right)\gamma\,|a|^2\,a, \tag{2.54}$$

where γ is the waveguide nonlinearity

$$\gamma = k_0\frac{\bar{n}_2}{A_{eff}},$$

$\bar{n}_2$ is the effective material nonlinearity given by

$$\bar{n}_2 = \frac{\varepsilon_0}{\mu_0}\frac{\int n^2 n_2\left(2\,|\vec{e}|^4 + |\vec{e}^2|^2\right)dA}{3\int\left|\left(\vec{e}\times\vec{h}^*\right)\cdot\hat{z}\right|^2 dA},$$

and A_{eff} is the effective area of the fundamental mode given by

$$A_{eff} = \frac{\left|\int\left(\vec{e}\times\vec{h}^*\right)\cdot\hat{z}dA\right|^2}{\int\left|\left(\vec{e}\times\vec{h}^*\right)\cdot\hat{z}\right|^2 dA}.$$

2.5 Split-Step Fourier Method

In this section, the split-step Fourier method is presented to numerically solve the nonlinear Schrodinger equation [9,84,85]. This method is relatively fast and accurate, and it includes the effects of chromatic dispersion and waveguide nonlinearity.

Frequency Domain Small Step Equation

The field envelope propagation equation in the frequency domain is given by

$$\frac{\partial}{\partial z}A\,(z,\omega) = \left[\hat{D}_\omega + \hat{N}_\omega\right]A\,(z,\omega)\,, \tag{2.55}$$

which is solved as

$$A\,(z,\omega) = A\,(0,\omega)\,e^{\left[\hat{D}_\omega+\hat{N}_\omega\right]z}.$$

where the operators $\hat{N}_\omega$ and $\hat{D}_\omega$ are given by

$$\hat{D}_\omega = -j\tfrac{1}{2}\beta_2 \left(\omega - \omega_0\right)^2 - \tfrac{\alpha}{2},$$
$$\hat{N}_\omega = -j\gamma|A|^2.$$

Increasing z by a step h to $z + h$ leads to

$$A\left(z + h, \omega\right) = A\left(0, \omega\right) e^{\left[\hat{D}_\omega + \hat{N}_\omega\right](z+h)}$$

which is expressed in terms of $A\left(z, \omega\right)$ as

$$A\left(z + h, \omega\right) = A\left(z, \omega\right) e^{\left[\hat{D}_\omega + \hat{N}_\omega\right](h)}. \tag{2.56}$$

Time Domain Small Step Equation

The time domain equation of field envelope propagation is given by

$$\frac{\partial A\left(z, t\right)}{\partial z} = \left[\hat{D}_t + \hat{N}_t\right] A\left(z, t\right), \tag{2.57}$$

which is solved to obtain

$$A(z, t) = A(0, t) e^{z(\hat{D}_t + \hat{N}_t)}$$

where $\hat{N}_t$ and $\hat{D}_t$

$$\hat{D}_t = -\tfrac{j\beta_2}{2}\tfrac{\partial^2}{\partial t^2} - \tfrac{\alpha}{2},$$
$$\hat{N}_t = -j\gamma|A|^2.$$

Increasing z by a step h to $z + h$ leads to

$$A\left(z + h, t\right) = A\left(0, t\right) e^{\left[\hat{D}_t + \hat{N}_t\right](z+h)}$$

which is expressed in terms of $A\left(z, t\right)$ as

$$A\left(z + h, t\right) = A\left(z, t\right) e^{\left[\hat{D}_t + \hat{N}_t\right](h)}. \tag{2.58}$$

The Split-Step Fourier Method

Eq. 2.58 is rearranged to obtain

$$A\left(z+h,t\right)=e^{h\hat{N}_t}\left[e^{h\hat{D}_t}A\left(z,t\right)\right],$$

in which

$$e^{h\hat{D}_t}A\left(z,t\right)$$

is easily calculated in the frequency domain using

$$e^{h\hat{D}_t}A\left(z,t\right)=\mathbf{F}^{-1}\left[e^{h\hat{D}_\omega}A\left(z,\omega\right)\right],$$

where $\mathbf{F}^{-1}$ is the inverse Fourier transform operator, leading to

$$A\left(z+h,t\right)=e^{h\hat{N}_t}\mathbf{F}^{-1}\left[e^{h\hat{D}_\omega}A\left(z,\omega\right)\right]. \tag{2.59}$$

To obtain an equation in terms of the time domain field amplitude $A\left(z,t\right)$, Eq. 2.59 is expressed as

$$A\left(z+h,t\right)=e^{h\hat{N}_t}\mathbf{F}^{-1}\left[e^{h\hat{D}_\omega}\mathbf{F}\left[A\left(z,t\right)\right]\right], \tag{2.60}$$

where $\mathbf{F}$ is the Fourier transform operator.

Pulse propagation through a nonlinear microwire is simulated by dividing the propagation length into steps with a length h and iteratively using Eq. 2.60 to compute the pulse shape after each step. Using this method, the temporal shape and the spectrum of a pulse after propagation through a microwire are computed from the temporal shape and the spectrum of an input pulse. Figure 2.6 presents an example of propagating a transform limited Gaussian pulse with a full width at half maximum width $T_0 = 8$ ps and a peak power of 300 mW in a 10 cm long microwire with $\gamma = 255$ $\mathrm{W^{-1}m^{-1}}$ and $D_c = 264$ ps/(nm.km).

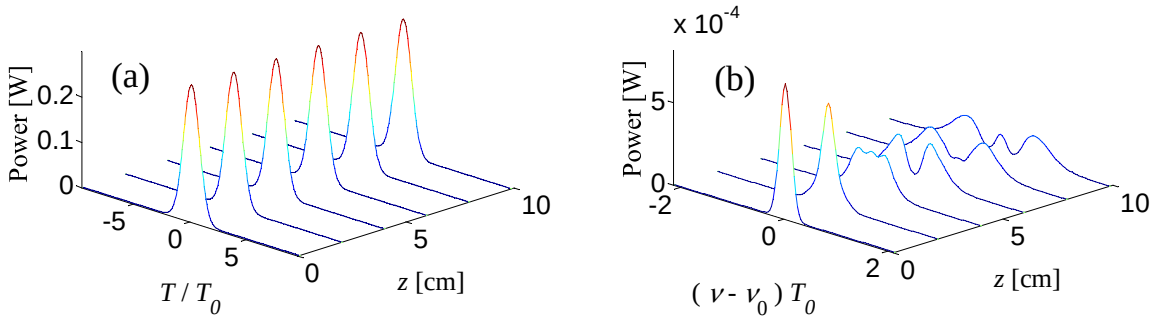

Fig. 2.6 Gaussian pulse propagation in an As_2Se_3 microtaper using the split-step Fourier method showing (a) the temporal and (b) the spectral shape of the pulse.

2.6 Conclusion

Two different methods for the analysis of microwires are presented. The first method is based on modeling the microwire as a step-index fiber waveguide with an infinite cladding and finding an analytical solution for the modes' propagation constants and vector field distributions. The analytical solution of the step-index fiber waveguide shows that any analysis based on the weak guiding approximation is not accurate due to the large refractive index between the core and the cladding. Moreover, the scalar field approximation is not valid in microwires and the vector field distribution must be calculated. The second method is based on the tangential vector finite-element method that is used for analyzing complex microwire structures including microwire structures with a finite cladding diameter, an eccentric core, or multiple cores. The nonlinear Schrodinger equation for simulating pulse propagation in microwires is then derived and numerically solved using the split-step Fourier method.

Chapter 3

Taper Fabrication

Microwires are formed in the waist of tapered optical fibers, illustrated in Fig. 3.1, which are made by a heat-and-draw approach. In general, tapered optical fibers have been used for enhancing nonlinear effects [15, 19], coaxial mode coupling [57], power splitting/combining [61], filtering optical spectra [59], and switching [62]. In all cases, a fine control of the taper shape is required to ensure an adiabatic transformation of the propagating mode [31, 32].

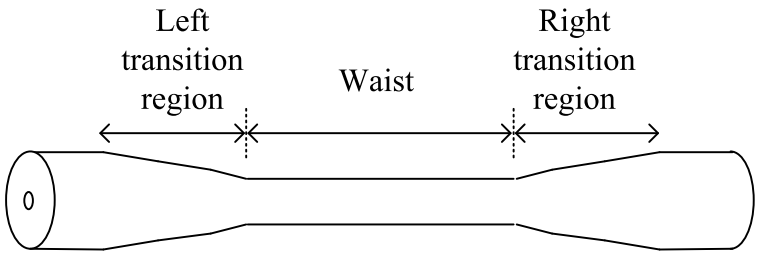

Fig. 3.1 Schematic of a fiber taper with a uniform waist and similar transition regions.

In this chapter, we develop and demonstrate both by simulation and experiment a generalized heat-brush tapering method, and use it for the fabrication of tapers with a nonuniform waist profile and dissimilar transition regions. First, single-sweep tapering, the main constituent of the generalized heat-brush approach, is presented and simulated using a viscous fluid flow model to quantify the mismatch error between the targeted and the resulting taper profiles. Then, the generalized heat-brush approach is implemented by tapering a fiber over multiple sweeps, and the simulation results from the single-sweep

tapering analysis are used to quantify the accumulated mismatch error after each tapering sweep. Finally, we use of the generalized heat-brush approach to fabricate an As_2Se_3 chalcogenide taper with a linearly decreasing waist profile and dissimilar transition regions.

3.1 Single-Sweep Tapering

In this section, we present the single-sweep tapering method, an instance of the well-known fiber-drawing approach [86–88]. In the process of fiber drawing, mass conservation leads to $\phi(t) = \phi_0\sqrt{s(t)}$ where $\phi(t)$ is the taper diameter, ϕ_0 is the initial fiber diameter, and $s(t) = v_f(t)/v_d(t)$ is the tapering function. To draw a taper with a predefined profile $\phi(z)$, the tapering function $s(t)$ must be determined accordingly. The replacement of the time variable t by the drawing length $l_d(t) = \int_0^t v_d(\tau)\,d\tau$ simplifies the implementation of the single-sweep tapering method because it can be readily used as a feedback parameter to control the draw velocity $v_d(l_d) = v_f(l_d)/s(l_d)$. In this case, the tapering function $s(l_d)$ is calculated from the taper profile $\phi(z)$ using

$$s(l_d) = \left.\frac{\phi^2(z)}{\phi_0^2}\right|_{z=l_d}.$$

Figure 3.2 provides an arbitrary taper profile $\phi(z)$ and its corresponding tapering function $s(l_d)$.

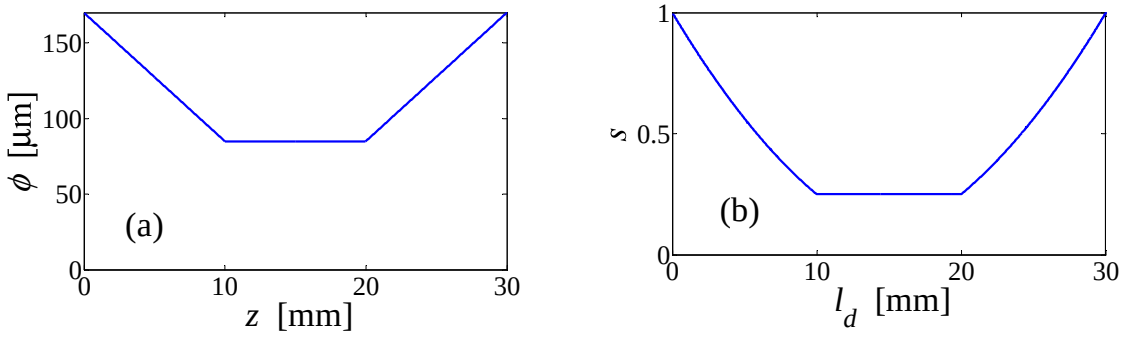

Fig. 3.2 a) A taper profile and b) the resulting tapering function.

Single-Sweep Tapering Simulations

A general model of the viscous flow in the heat-softened region, or hot-zone, due to unidirectional stretching has been reported in [86]. A simplified model has been derived for the case when the fiber diameter is much smaller than the hot-zone length (L_{hz}) [87]. In this model, the deformation of the hot-zone due to stretching is governed by

$$\frac{\partial}{\partial z}\left(3\mu A\frac{\partial u}{\partial z}\right)=0, \tag{3.1}$$

$$\frac{\partial A}{\partial t}+\frac{\partial}{\partial z}\left(uA\right)=0, \tag{3.2}$$

where $\mu\left(z,t\right)$ is the viscosity distribution, $u\left(z,t\right)$ is the axial velocity distribution, and $A\left(z,t\right)$ is the cross-sectional area in the hot-zone [87]. For a Newtonian fluid, μ is independent of u, and hence, Eq (3.1) leads to

$$\frac{\partial \bar{u}}{\partial z}\frac{\partial F}{\partial z}+F\frac{\partial^2 \bar{u}}{\partial z^2}=0,$$

where $\bar{u}=u/v_d$ is the normalized axial velocity and $F=\mu A$. Using the centered differentiation formulas [89]

$$\begin{array}{c}\frac{\partial F}{\partial z}=\frac{\left(F_{i+1}-F_{i-1}\right)}{2\Delta z}\\ \frac{\partial \bar{u}}{\partial z}=\frac{\left(\bar{u}_{i+1}-\bar{u}_{i-1}\right)}{2\Delta z}\\ \frac{\partial^2 \bar{u}}{\partial z^2}=\frac{\left(\bar{u}_{i+1}-2\bar{u}_i+\bar{u}_{i-1}\right)}{\Delta z^2}\end{array}$$

leads to the finite difference form of Eq (3.1)

$$\left[F_i-0.25\left(F_{i+1}-F_{i-1}\right)\right]\bar{u}_{i-1}-2F_i\bar{u}_i+\left[F_i+0.25\left(F_{i+1}-F_{i-1}\right)\right]\bar{u}_{i+1}=0 \tag{3.3}$$

where $F_i=F\left(l_d,z_i\right)$, $\bar{u}_i=\bar{u}\left(l_d,z_i\right)$, and Δz is the separation between any two consecutive z_i. Changing the variable t to l_d in Eq (3.2) leads to the equation

$$v_d\frac{\partial A}{\partial l_d}+\frac{\partial\left(uA\right)}{\partial z}=0,$$

which is expanded and divided by v_d to obtain

$$\frac{\partial A}{\partial l_d}+A\frac{\partial \bar{u}}{\partial z}+\bar{u}\frac{\partial A}{\partial z}=0.$$

Using the centered differentiation formulas

$$\frac{\partial \bar{u}}{\partial z} = \frac{(\bar{u}_{i+1} - \bar{u}_{i-1})}{2\Delta z},$$
$$\frac{\partial A}{\partial z} = \frac{(A_{i+1} - A_{i-1})}{2\Delta z},$$

and the forward differentiation formula [89]

$$\frac{\partial A}{\partial l_d} = \frac{\left[A_i^{new} - A_i\right]}{\Delta l_d} \ ,$$

the finite difference form of Eq (3.2) corresponding to the extension of the fiber by a distance $\Delta l_d = 2\Delta z$ is given by

$$A_i^{new} = A_i - \left[A_i \left(\bar{u}_{i+1} - \bar{u}_{i-1}\right) + \bar{u}_i \left(A_{i+1} - A_{i-1}\right)\right] \tag{3.4}$$

where $A_i = A\left(l_d, z_i\right)$, $A_i^{new} = A\left(l_d + \Delta l_d, z_i\right)$. It is clear from Eq (3.3) and Eq (3.4) that, for a Newtonian fluid, the deformation of the hot-zone is independent of the actual drawing velocity.

The flow-chart in Fig. 3.3 describes the program used to simulate the single-sweep experimental setup presented in Section 3.1. In this program, the taper profile is represented by an array of diameter values ϕ_k taken at points z_k with any two consecutive points separated by Δz. The hot-zone is a subarray of the taper array and the starting point of the hot-zone subarray can change to simulate a moving heater as illustrated in Fig. 3.4(a). The cross-section area in the hot-zone is given by A_i where $i = 1, 2, ..., N$ and the cross-section area of the extended hot-zone that results from drawing the hot-zone, as illustrated in Fig. 3.4(b), is calculated as follows: first, Eq (3.3) is used with the boundary conditions $\bar{u}_{i=0} = -1/2$ and $\bar{u}_{i=N+1} = 1/2$ to calculate the normalized axial velocity distribution $\bar{u}_i$ in the hot-zone, and then, Eq (3.4) is used to calculate the extended hot-zone profile. In the simulations that follow, the hot-zone is assumed to have a uniform viscosity distribution.

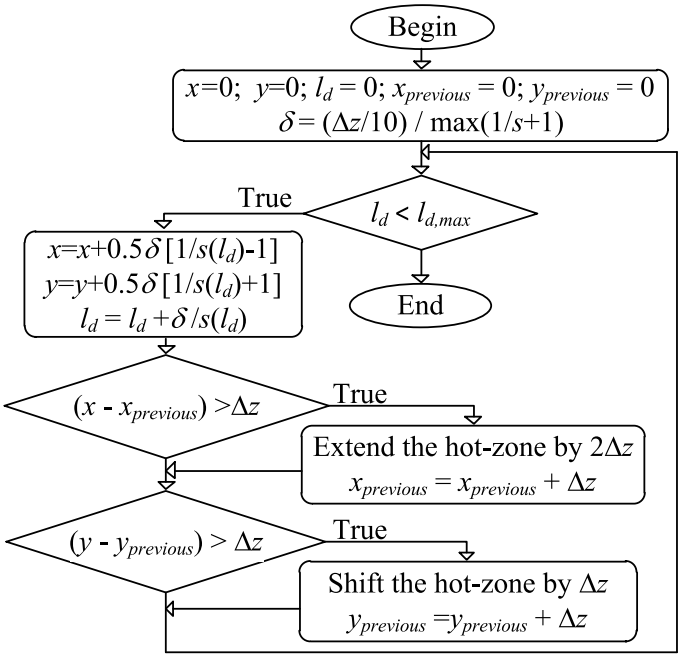

Fig. 3.3 Flow-chart of the simulation program for the single-sweep tapering setup presented in Section 3.1. In this flow-chart, x is the displacement of both translation stages extending the fiber, y is the displacement of the heater translation stage, $x_{previous}$ and $y_{previous}$ are state variables, δ is a differential feed step, s is the tapering function, l_d is the drawing length, and Δz is the longitudinal separation between any two consecutive diameter sampling points.

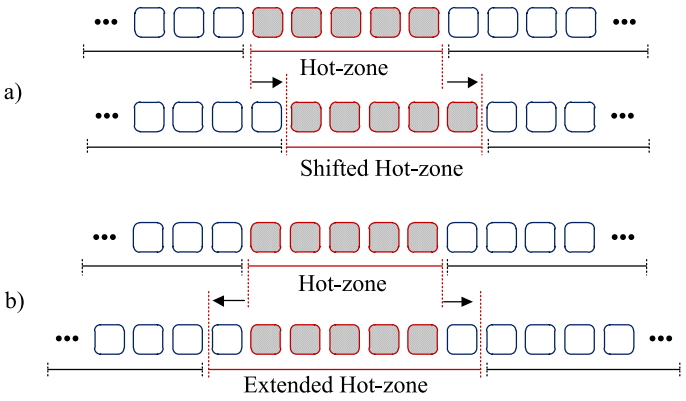

Fig. 3.4 Single-sweep simulation schematics of a) shifting the hot-zone by Δz, and b) extension of the fiber by $2\Delta z$.

We simulate the fabrication of a step-taper where the diameter changes abruptly from the initial to the final taper diameter. Typical simulation results of step-taper fabrication

show a transient response in the resulting taper with an overshoot and oscillations in the waist before the diameter settles to a final value, as shown in Fig. 3.5. The mismatch between the resulting and the targeted taper profiles is quantified by the percent error along the taper defined as

$$\varepsilon(z) = \frac{[\phi_r(z) - \phi_t(z)]}{\phi_t(z)} \times 100\%$$

where ϕ_r is the resulting taper diameter and ϕ_t is the targeted taper diameter. The transient response is quantified by the percent overshoot

$$\varepsilon_{os} = \frac{(\phi_t - \phi_{os})}{\phi_t} \times 100\%$$

where ϕ_{os} is the overshoot diameter, and by the settling distance z_s defined as the distance between the beginning of the waist and the point where the envelope of the absolute percent error is less than $\varepsilon_s = 2\%$.

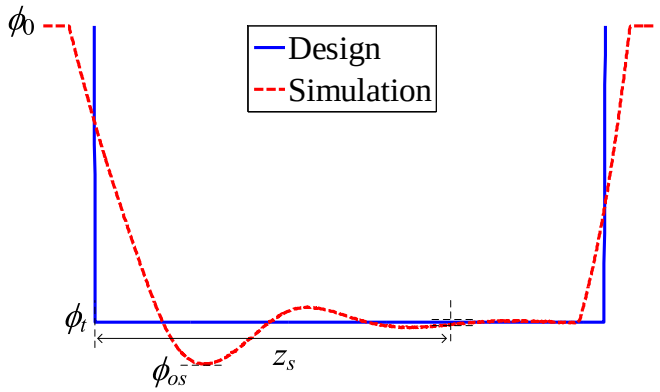

Fig. 3.5 Simulation of step-taper fabrication using the single-sweep tapering method.

The transient response parameters ε_{os} and z_s represent the closeness of the of the resulting taper shape to the taper design, and the overall mismatch is reduced by reducing ε_{os} and z_s. Step-taper simulation results in Fig. 3.6 show ε_{os} and z_s as a function of L_{hz} and the inverse tapering ratio $\rho = \phi_{min}/\phi_0$, where ϕ_{min} is the minimum taper diameter. As expected, ε_{os} and z_s decrease with increasing ρ (≤ 1) and shortening L_{hz}. With respect to

optical propagation in the taper, the overshoot in the waist diameter acts as a perturbation that may lead to coupling between the fundamental mode and higher order modes, radiation modes, or reflection modes [63]. The values of ε_{os} and z_s also represents the strength and the length of the perturbation region; therefore, a lower ε_{os} and a shorter z_s reduces the perturbation impact.

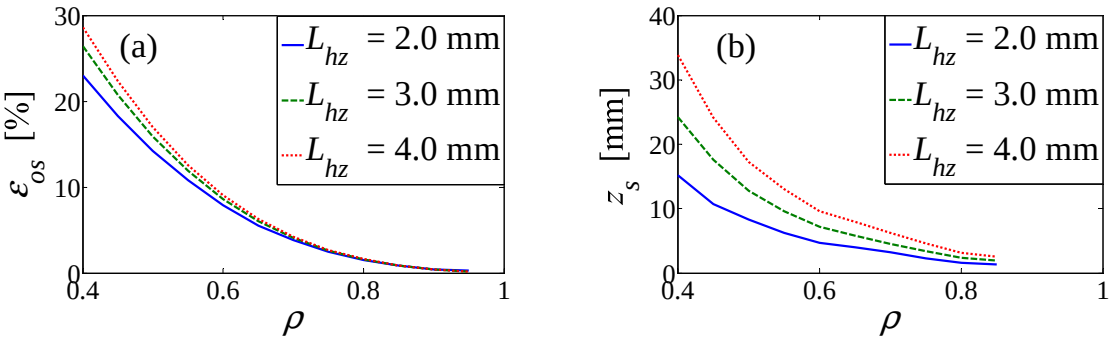

Fig. 3.6 a) Percent overshoot, and b) settling distance dependence on the inverse tapering ratio at different hot-zone lengths for the step-taper.

Single-Sweep Tapering Optimization

Simulation results in subsection 3.1 showed that ε_{os} and z_s decrease when $\rho \to 1$ and $L_{hz} \to 0$ mm. However, applications such as the enhancement of the waveguide nonlinearity or the sensitivity require microtapers with a waist diameter on the order of 1 µm drawn from fibers with a diameter on the order of 100 µm leading to $\rho \sim 0.01$. Also, L_{hz} is on the order of 1 mm and is limited by the temperature distribution in the fiber and the heater dimensions. Moreover, it turns out that ε_{os} and z_s decrease when the taper slope decreases. As an example, Fig. 3.7 shows that as the slope decreases from 0.0105 to 0.0035, ε_{os} decreases from 8.8% to 3.8% and z_s decreases from 13.5 mm to 11.65 mm. In most cases, however, it is desirable to use the largest slope allowed by the adiabaticity criteria because using a small taper slope to reduce ε_{os} and z_s leads to a long transition region and consequently increases the sensitivity of the taper to environmental variations [24] as well as increasing the device length. Section 3.2 shows that ε_{os} and z_s are reduced by tapering a fiber over multiple sweeps leading to an implementation of the generalized heat-brush approach.

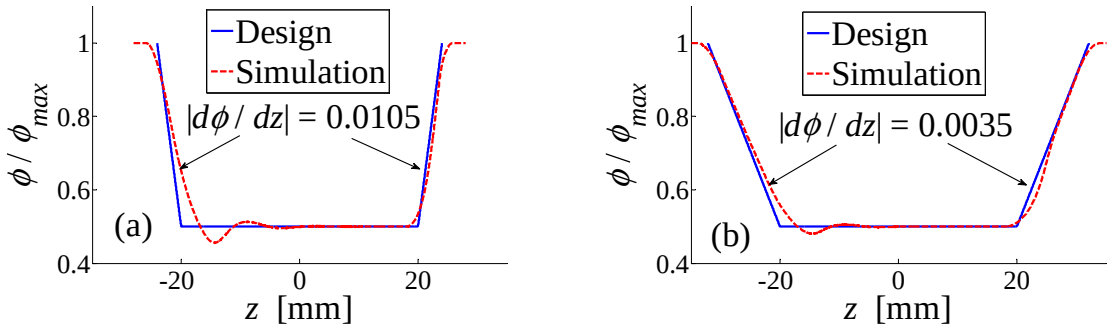

Fig. 3.7 Simulated fabrication results of taper profiles with linear transition regions at different slopes using the single-sweep tapering method.

Experimental Setup

Figure 3.8 illustrates the experimental implementation of the single-sweep tapering method where a translation stage moves the heater at a velocity v_y and two other translation stages pull the fiber from opposite directions at equal velocities v_w and v_x. Using $v_d = v_y + v_w$ and $v_f = v_y - v_x = \alpha$, where α is a constant, the velocities of the heater and the translation stages pulling on the fiber at a drawing length $l_d = y + w$ are

$$v_y(l_d) = \frac{v_d(l_d) + v_f(l_d)}{2} = \frac{\alpha}{2}\left[\frac{1}{s(l_d)} + 1\right],$$

$$v_x(l_d) = v_w(l_d) = \frac{v_d(l_d) - v_f(l_d)}{2} = \frac{\alpha}{2}\left[\frac{1}{s(l_d)} - 1\right].$$

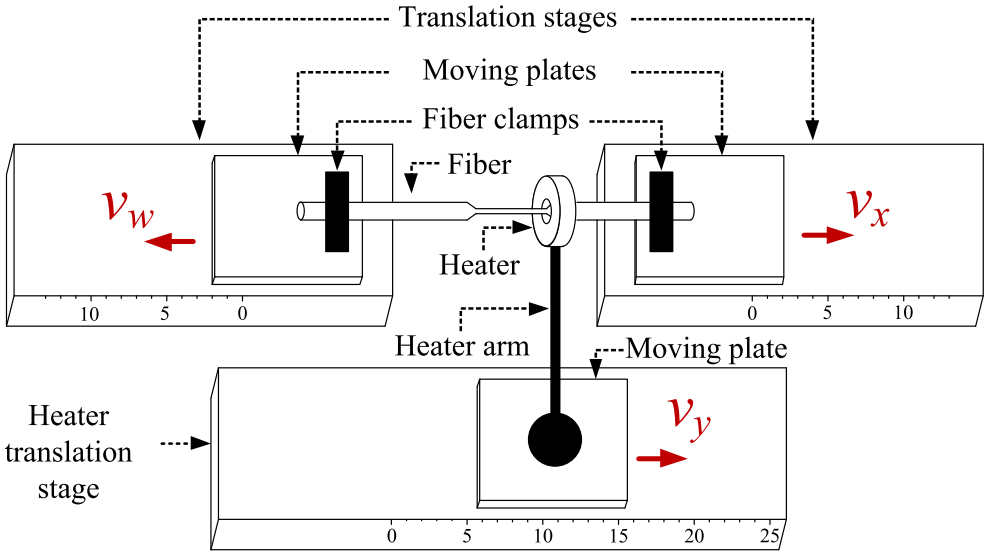

Fig. 3.8 Schematic of the experimental implementation of the single-sweep tapering method.

Single-Sweep Tapering Experimental Results

Figure 3.9(a) shows the experimental results of a step-taper fabricated from an As_2Se_3 fiber with an initial diameter of 170 µm using a 5 mm long resistive heater at 210° C with $v_f = 0.72$ mm/min and $v_d^{max} = \max(v_f/s) = 4.5$ mm/min. The fabricated taper is removed from the tapering setup and placed straight on a flat plate, and then, an imaging system composed of a 20× lens and a CCD camera mounted on a motorized translation stage is used to measure the taper profile with a measurement taken every 1.0 mm. The measured step-taper profile clearly shows an overshoot in the fiber diameter arising from the finite length of the hot-zone. An effective hot-zone length of 2.7 mm is retrieved by simulating the step-taper fabrication and fitting the simulation results with the measured profile. The measured effective length is used to simulate the fabrication of the taper in Fig. 3.9(b) and the simulation results show good agreement with the experimental results within the measurement error of 1 µm.

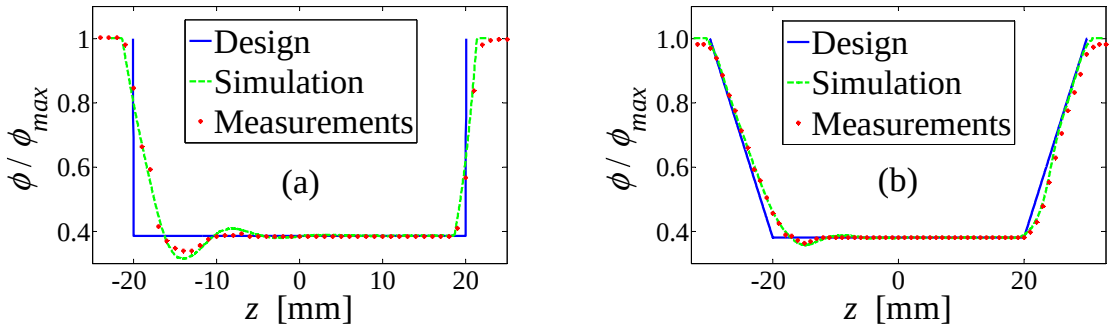

Fig. 3.9 Experimentally measured profiles of a) a step taper, and b) an arbitrary taper fabricated using the single-sweep tapering method.

3.2 Multi-Sweep Tapering

Multi-sweep tapering performed by systematic repetition of the single-sweep method as illustrated in Fig. 3.10 represents an implementation of the generalized heat-brush method. To taper a fiber over n sweeps, the taper profile is divided into subsections as shown in Fig. 3.11, where ϕ_n is the minimum taper diameter, and ϕ_1 to ϕ_{n-1} are the waist diameters for all intermediate tapering sweeps and are calculated using $\phi_j = r\phi_{j-1}$ with $r = \rho^{1/n}$ and $\rho = \phi_n/\phi_0$. For every sweep $j < n$, the stage tapering function $s^{(j)}(l_p)$ is calculated from the stage taper profile $\phi^{(j)}(z)$ composed of a left transition region extracted from $\phi(z)$ between z_{j-1}^{left} and z_j^{left}, a right transition region extracted from $\phi(z)$ between z_j^{right} and z_{j-1}^{right}, and a uniform waist with a length

$$L_j = \frac{\int_{z_j^{left}}^{z_j^{right}} \phi^2(z)\, dz}{\phi_j^2},$$

where L_j makes the mass volume of the waist at stage j equal to the mass volume required to draw the taper section between z_j^{left} and z_j^{right}. The stage taper profile of the final sweep $\phi^{(n)}(z)$ is extracted from $\phi(z)$ between z_{n-1}^{left} and z_{n-1}^{right}, and is used to calculate the final stage tapering function $s^{(n)}(l_p)$. Finally, for each stage j, a single tapering sweep is performed using the calculated stage tapering function and then the heater is moved back a distance $\left(z_{j-1}^{right} - z_j^{right}\right) + L_j$.

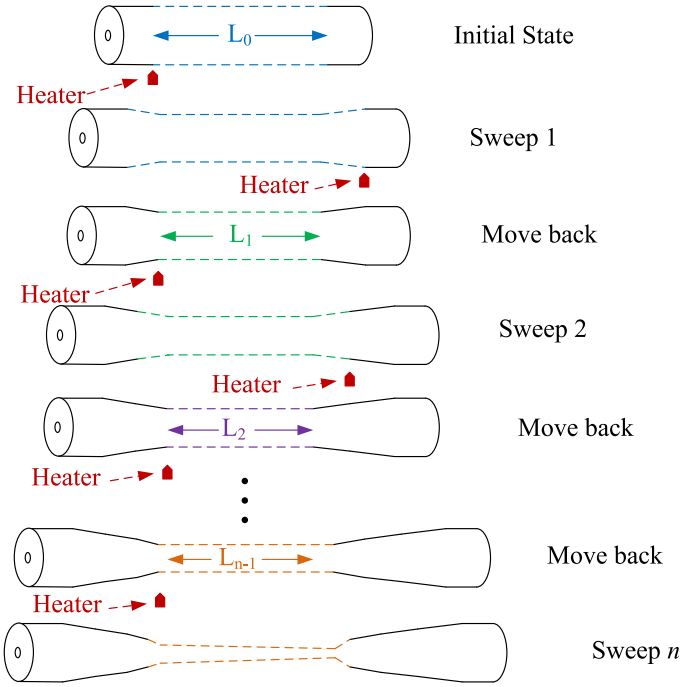

Fig. 3.10 Schematic of taper profile evolution using the multi-sweep tapering method.

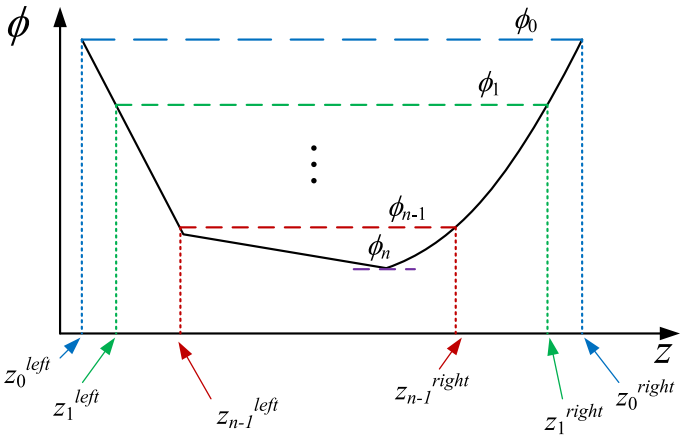

Fig. 3.11 Dividing the taper into sections for the determination of the tapering function of each tapering stage.

Quantitative Analysis of Multi-Sweep Tapering

Based on the divide-and-conquer paradigm [90], tapering a fiber over multiple sweeps reduces the percent overshoot. For a step-taper, the worst-case overshoot diameter at sweep j is estimated using the recurrence relation

$$\phi_{os}^{(j)} = \left[1 - \varepsilon_{os}\left(\rho_j\right)/100\%\right] \times \rho_j \times \phi_{os}^{(j-1)}$$
$$\phi_{os}^{(1)} = \left[1 - \varepsilon_{os}\left(\rho_1\right)/100\%\right] \times \rho_1 \times \phi_0,$$

where $\varepsilon_{os}\left(\rho_j\right)$ is provided in Fig. 3.6(a). By setting the inverse tapering ratio for all sweeps to r, the worst-case overshoot diameter becomes

$$\phi_{os}^{(j)} = \left[1 - \varepsilon_{os}\left(r\right)/100\%\right]^j \times r^j \times \phi_0,$$

and the maximum percent overshoot at the end of tapering is

$$\varepsilon_{os,max}^{(n)} = \left[1 - \left(1 - \varepsilon_{os}\left(r\right)/100\%\right)^n\right] \times 100\%, \tag{3.5}$$

which is simplified to $\varepsilon_{os,max}^{(n)} \approx n\varepsilon_{os}\left(r\right)$ when $\varepsilon_{os}\left(r\right) \leq 1\%$. It is clear from Fig. 3.6(a) that $\varepsilon_{os,max}^{(n)} < \varepsilon_{os}\left(\rho\right)$ and that $\varepsilon_{os,max}^{(n)}$ decreases as n increases. For, example, the fabrication of a step-taper with $\rho = 0.5$ over a single sweep using a 4 mm long hot-zone leads to $\varepsilon_{os}\left(0.5\right) = 17\%$. However, when tapering is performed over 6 sweeps with $r = 0.89$ and $\varepsilon_{os}\left(0.89\right) = 0.5\%$, the maximum percent overshoot is $\varepsilon_{os,max}^{(6)} = 3\%$.

The use of a large number of sweeps increases the tapering duration. For the case of a step-taper, the minimum time duration for stage j is $T_j = L_{j-1}/v_f^{max}$, where v_f^{max} is the maximum practical feed velocity, and the total tapering duration after n sweeps is

$$T = \frac{L_0}{v_f^{max}} \times \frac{1 - \rho^{-2}}{1 - \rho^{-2/n}},$$

which is reduced by increasing v_f^{max} and reducing n. In general, to keep the tapering duration at a minimum, n is selected to be the minimum number of sweeps required to keep ε_{os} bellow a certain prescribed value.

Multi-Sweep Tapering Simulation

Multi-sweep tapering simulation is performed by repeated application of the single sweep tapering program. Simulation results in Fig. 3.12 performed using $L_{hz} = 3$ mm for a step-taper with $\rho = 0.4$ show that the percent overshoot $\varepsilon_{os}^{(n)}$ decreases as n increases. Also shown in Fig. 3.12 is the worst-case percent overshoot, $\varepsilon_{os,max}^{(n)}$, calculated using Eq (3.5). It is observed that $\varepsilon_{os}^{(n)}$ does not exceed $\varepsilon_{os,max}^{(n)}$, which is expected as $\varepsilon_{os,max}^{(n)}$ estimates the upper limit of $\varepsilon_{os}^{(n)}$.

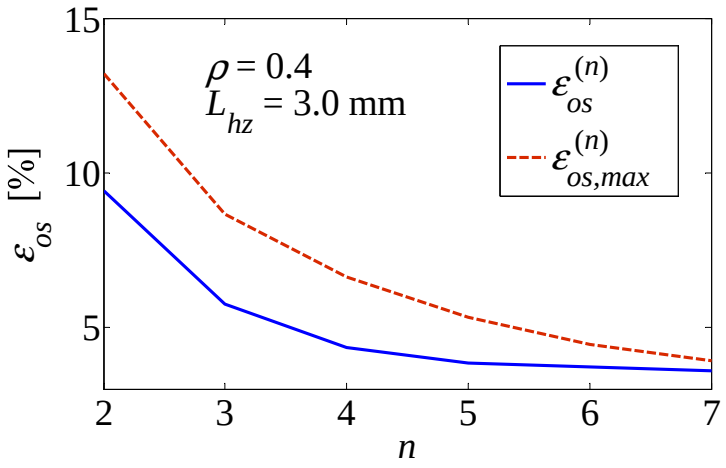

Fig. 3.12 Percent overshoot and maximum percent overshoot versus the number of tapering sweeps n for a step-taper with $\rho = 0.4$ using $L_{hz} = 3$ mm.

Although increasing n reduces ε_{os}, L_{hz} must also be shortened to ensure that $|\varepsilon(z)|$ is less than a prescribed value ε_{target}. Shortening L_{hz} is critical when the taper profile incorporates fine details such as a large $\partial\phi/\partial z$, a large change in $\partial\phi/\partial z$, or a short waist. For example, if the taper waist length is of the same order as L_{hz}, then the details of the waist can not be precisely shaped. The value of L_{hz} that ensures $|\varepsilon(z)| < \varepsilon_{target}$ for a given taper profile can be determined through simulations.

Multi-Sweep Tapering Experimental Results

Figure 3.13 shows the experimental results for the fabrication of an As_2Se_3 taper with an initial fiber diameter of 170 µm, dissimilar left and right transition regions, and a

nonuniform waist with a diameter decreasing linearly from 15 µm to 10 µm over a waist length of 2.0 cm. The taper is experimentally fabricated over 24 sweeps using the same resistive heater in the single-sweep experiment in Subsection 3.1 at 210° C with v_f = 3.56 mm/min and v_d^{max} = 4.50 mm/min. The measurement error is 1 µm and the resulting taper matches the design within the measurement error.

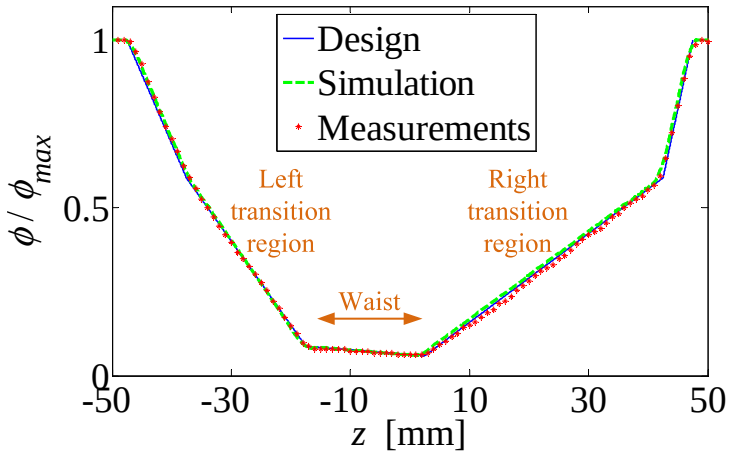

Fig. 3.13 Experimental results showing the profile of an As_2Se_3 taper fabricated using the multi-sweep tapering method with $n = 24$.

3.3 Conclusion

The multi-sweep tapering method has been used to implement the generalized heat-brush approach, which allows the ratio of the feed and draw velocities to change within each tapering sweep. A quantitative analysis showed that the mismatch error decreases by increasing the number of tapering sweeps and shortening the length of the hot-zone formed by the heater. An As_2Se_3 chalcogenide taper with dissimilar transition regions and a waist diameter decreasing linearly from 15 µm to 10 µm over 2.0 cm was fabricated using the multi-sweep tapering method showing good agreement between the targeted and the measured taper profiles.

Chapter 4

Hybrid Microwires from Single-Mode Hybrid Fibers

In this chapter, we present the fabrication and optical characterization of a hybrid chalcogenide-polymer microwires composed of an As_2Se_3 core and a PMMA cladding. With this material combination, the As_2Se_3 core induces a large Kerr effect whereas the PMMA cladding provides sufficient mechanical robustness and flexibility to the assembly for normal handling as well as limiting the evanescent interaction with the surrounding environment. Self-phase modulation and super-continuum generation are demonstrated in such microwires.

4.1 Single-Mode Hybrid Fibers Fabrication

Fabrication of a single-mode hybrid fiber involves the characterization of a multi-mode step-index As_2Se_3 fiber and pretapering it to obtain the single-mode As_2Se_3 fiber. The single-mode As_2Se_3 fiber is then coated with a PMMA layer using a PMMA microtube to obtain a single-mode hybrid fiber. The PMMA microtube is fabricated by drawing a commercially available PMMA tube. Both ends of the hybrid fiber are polished and coupled to SMF fibers using UV curing epoxy to obtain a hybrid fiber ready for tapering.

As_2Se_3 Fiber Characterization

Figure 4.1 presents a schematic of the setup used for the characterization of the step-index As_2Se_3 fiber provided by Coractive High-Tech. Amplified spontaneous-emission noise from

an Erbium-Doped Fiber Amplifier with a peak power at $\lambda = 1530$ nm and a Semiconductor Optical Amplifier with a peak power at $\lambda = 1310$ nm combined together using a 3 dB coupler to form a broadband source in the wavelength range between 1150 nm and 1650 nm. Using butt-coupling, the broadband light is launched from an SMF into the core of a 22.6 cm long As_2Se_3 fiber in such a way as to excite both of the LP_{01} and LP_{11} modes. Power is coupled into the LP_{11} mode by transverse misalignment of the cores of the launching fiber and the As_2Se_3 fiber. The electric fields of the LP_{01} and LP_{11} modes interfere with each other forming a unique spectral pattern at the output of the As_2Se_3 fiber. To observe this spectral pattern, the output end of the As_2Se_3 fiber is butt-coupled to a receiving SMF, which in turn is connected to an OSA. The core of the receiving fiber is transversely misaligned with respect to the core of As_2Se_3 fiber to provide a clear interference pattern at the OSA.

Fig. 4.1 Schematic of the As_2Se_3 fiber characterization setup.

When both of the LP_{01} and LP_{11} modes are excited at the input of a fiber, the total electric field at any point of the output of the fiber has the form

$$E = a_{01}e^{j\beta_{01}L} + a_{11}e^{j\beta_{11}L}$$

and the intensity is given by

$$I = |a_{01}|^2 + |a_{11}|^2 + 2\,|a_{01}|\,|a_{11}|\cos\left[\Delta\beta L + \theta_{01} - \theta_{11}\right],$$

where a_{m1} and β_{m1} are the complex amplitude and the propagation constant of the LP_{m1} mode with m being 0 or 1, θ_{m1} is the phase of a_{m1}, L is the length of the fiber, and $\Delta\beta = \beta_{01} - \beta_{11}$. A spectral interference pattern with a modulation proportional to $\cos\left[\Delta\beta L + \theta_{01} - \theta_{11}\right]$ arises from the wavelength dependence of $\Delta\beta$, which is completely determined by D and NA.

Figure 4.2 shows the spectral interference pattern in the dual-mode wavelength range of a 22.6 cm long As_2Se_3 fiber, measured using and OSA with a resolution-bandwidth (RBW)

of 5 nm, a sensitivity (s) of -85 dBm, and a wavelength separation ($\Delta\lambda$) of 0.63 nm between any two consecutive spectrum points. The spectral interference pattern exhibits a relatively large number of oscillations per unit of spectral width at short wavelengths because of a strong variation of $\Delta\beta(\lambda)$, expressed mathematically by $|\partial\Delta\beta/\partial\lambda|$. The number of oscillations per unit of spectral width decreases to a minimum at a wavelength in coincidence with the maximum of the $\Delta\beta(\lambda)$ function, and then increases at longer wavelengths as $|\partial\Delta\beta/\partial\lambda|$ increases again. Two wavelengths λ_{left} and λ_{right} are selected to identify the wavelength region of slow oscillations, as highlighted in Fig. 4.2. Wavelength values $\lambda_i \leq \lambda_{left}$ and $\lambda_j \geq \lambda_{right}$ corresponding to the minima of the measured interference pattern are recorded. The phase difference $\Delta\phi(\lambda) = \Delta\beta(\lambda)\,L + \theta_{01} - \theta_{11}$ increases by 2π between λ_i and λ_{i+1} for all $\lambda_i \leq \lambda_{left}$ and decreases by 2π between λ_j and λ_{j+1} for all $\lambda_j \geq \lambda_{right}$ leading to

$$\Delta\beta_{i+1} = \Delta\beta_i + 2\pi/L = \Delta\beta_{i=1} + 2\pi i/L,$$

$$\Delta\beta_{j+1} = \Delta\beta_j - 2\pi/L = \Delta\beta_{j=1} - 2\pi j/L,$$

where $\Delta\beta_i = \Delta\beta(\lambda_i)$ and $\Delta\beta_j = \Delta\beta(\lambda_j)$. If $\Delta\beta_{i=1}$ and $\Delta\beta_{j=1}$ were known, a set of values $\Delta\beta_{meas}(\lambda)$ representing the measured propagation constant difference as a function of wavelength is obtained.

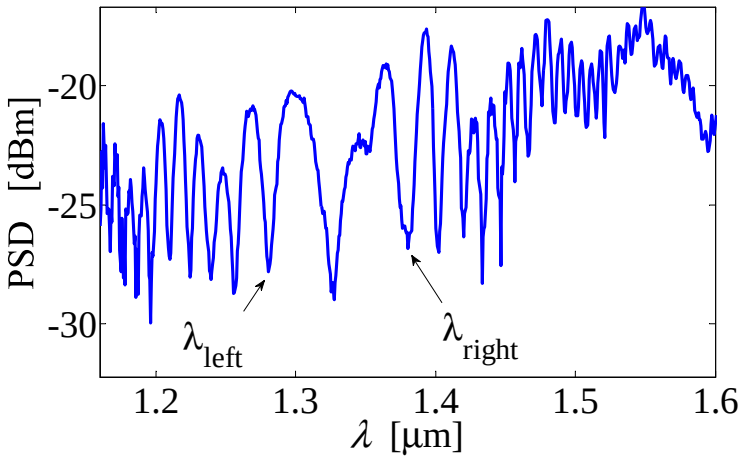

Fig. 4.2 The interference spectrum between the LP_{01} and LP_{11} modes in a 20.7 cm long As_2Se_3 fiber.

An iterative optimization process is used to determine the values of D and NA. In each iteration, a theoretical curve $\Delta\beta_{th}(\lambda)$ is calculated first using a pair D and NA, and the measured propagation constant difference $\Delta\beta_{meas}(\lambda)$ is specified by setting $\Delta\beta_{i=1} = \Delta\beta_{th}(\lambda_{i=1})$ and $\Delta\beta_{j=1} = \Delta\beta_{th}(\lambda_{j=1})$. The values of the core diameter and numerical aperture of the FUT result in the minimum error $\epsilon = \sum |\Delta\beta_{meas}(\lambda) - \Delta\beta_{th}(\lambda)|$ where λ takes on all the values of λ_i and λ_j. The fiber parameters obtained from the optimization process are $D = 6.88$ µm and $NA = 0.184$ leading to the best fit between $\Delta\beta_{meas}(\lambda)$ and $\Delta\beta_{th}(\lambda)$ as shown in Fig. 4.3.

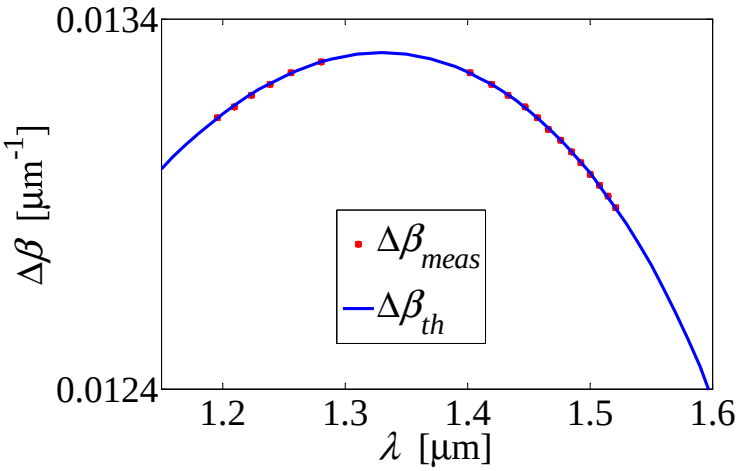

Fig. 4.3 Experimental and theoretical values of $\Delta\beta(\lambda)$ for the 20.7 cm long As_2Se_3 fiber using the optimal values of $D = 6.88$ µm and $NA = 0.184$.

As_2Se_3 Fiber Pretapering

Using the measured values of $D = 6.88$ µm and $NA = 0.184$, the normalized frequency $(V = 3.2) > 2.4$ and the fiber is multi-mode. The core diameter must be reduced such the $V < 2.4$ to obtain single-mode guidance in the core of the As_2Se_3 fiber. The single-sweep tapering method is used to taper the As_2Se_3 fiber and reduce its dimensions by a ratio of 0.8, as illustrated in Fig. 4.4. The waist of the resulting taper is cut to obtain an As_2Se_3 fiber with $D = 5.5$ µm, $NA = 0.184$, and $V = 2.1$ which satisfies the single-mode fiber condition $V < 2.4$.

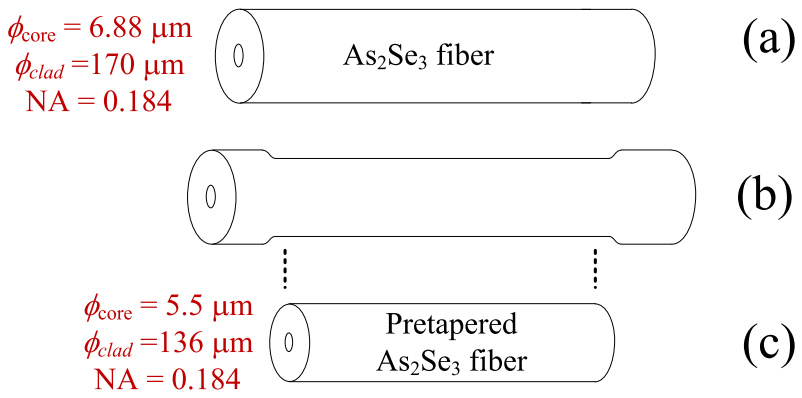

Fig. 4.4 Schematic of pretapered As_2Se_3 fiber preparation showing a) the initial As_2Se_3 fiber, b) fiber diameter reduction by tapering, and c) the pretapered single-mode As_2Se_3 fiber.

Drawing PMMA Microtubes

Microtubes are fabricated by the process of drawing PMMA preforms obtained from commercially available PMMA tubes. In this process, the preform is slowly inserted at a constant velocity into a furnace that heats the preform to a softening point, and the microtube is drawn at a higher velocity from the other side of the furnace. This causes the soft part to elongate and a microtube with a scaled down cross-section pattern results from the preform. The ratio of the microtube diameter and the initial tube diameter is given by

$$r_t/r_p = \sqrt{v_f/v_d}$$

where r_p is the preform radius, r_t is the radius of the resulting microtube, v_f is the preform feed velocity, and v_d is the tube drawing velocity. In general, the cross sectional pattern of the preform is scaled down by a factor $\sqrt{v_f/v_d}$.

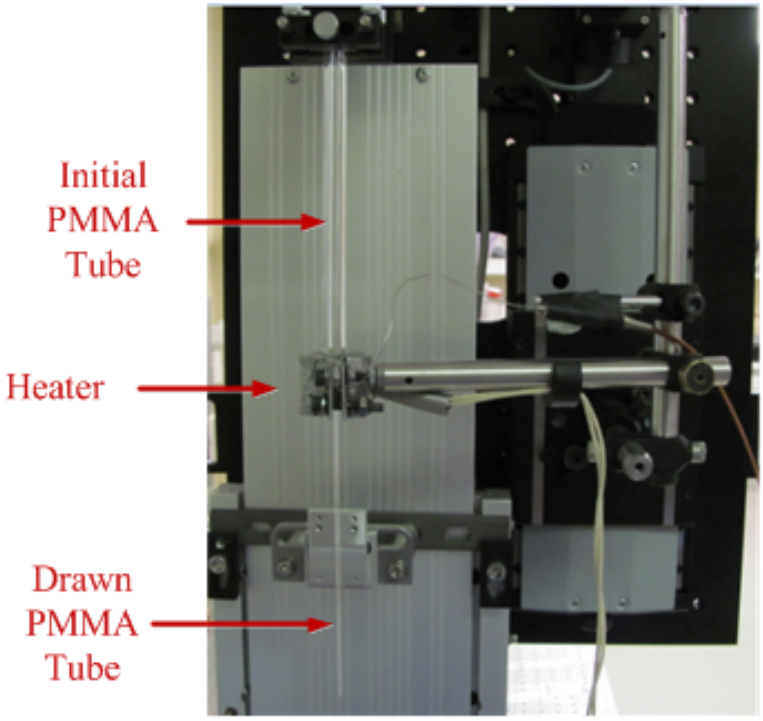

Fig. 4.5 Drawing setup.

PMMA microtubes fabricated using the drawing setup must be free of internal stresses. A PMMA preform becomes soft and malleable when it enters the furnace in the drawing setup. As microtubes are drawn from the PMMA preform, elastic forces forming in PMMA work to restore it back to the preform shape. Before elastic forces are completely relaxed, the drawn PMMA microtube leaves the furnace, cools down, and solidifies. The elastic forces become frozen in the solid PMMA microtube as internal stresses, which remain as dormant forces. The effect of internal stresses is observed when the PMMA microtube is heated to the softening point where internal stresses deform its shape. PMMA microtubes with no internal stresses are fabricated by increasing the furnace temperature and decreasing the drawing velocity. Another approach that can be used for removing internal stresses is annealing.

Coating As_2Se_3 Fibers with a PMMA Layer

Figure 4.6 illustrates the process of coating the pretapered As_2Se_3 fiber with a PMMA layer. This polymer is used because its softening temperature is compatible with that of

As_2Se_3 which is $T = 190°$ C. The As_2Se_3 fiber is placed in the PMMA microtube and the assembly is inserted at a feed velocity v_f into an cylindrical oven heated using a resistive heater to $175^o - 185$ C. The PMMA microtube with a down-scaled cross-section exits from the other side of the oven at a drawing velocity $v_d > v_f$, and the inner diameter of the PMMA tube is reduced to coat the As_2Se_3 fiber.

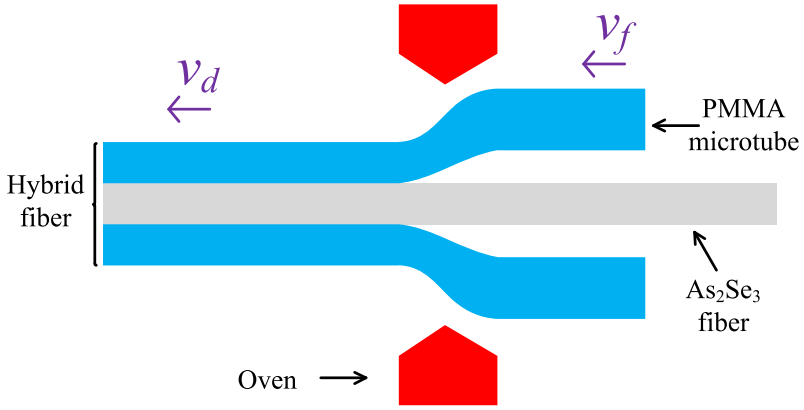

Fig. 4.6 Schematic illustration of As_2Se_3 fiber coating with a PMMA layer.

Polishing Hybrid Fibers

Figure 4.7 shows the setup used to polish the end facets of hybrid fibers. The polishing setup consists of a rotating polishing disc on which polishing paper is placed, a fiber holder to hold the fiber perpendicular to the polishing disc surface, and a camera to monitor the fiber tip as it is being polished. A translation stage is used to approach the fiber tip to the rotating polishing disc. The polishing is preformed is five stages in which polishing paper with particles sizes of 20 µm, 3.0 µm, 1.0 µm, 0.5 µm, and 0.3 µm are used.

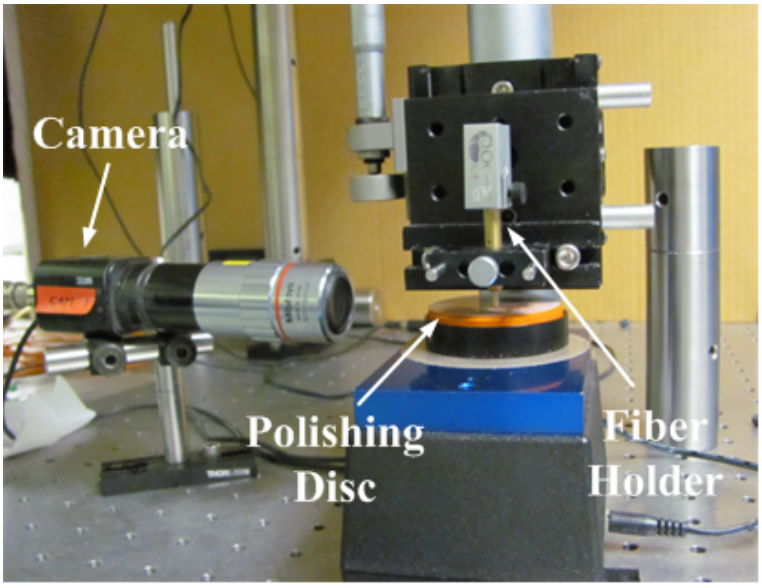

Fig. 4.7 Fiber polishing setup.

The Coupling Setup

The coupling setup consists mainly of two alignment stages, an IR camera connected to a screen, a microscope, and a UV lamp, as shown in Fig. 4.8. The first alignment stage is used to launch light at $\lambda = 1550$ nm from an SMF into the core of the hybrid fiber. The output end of the fiber is observed using an infrared camera connected to a screen to monitor the alignment process and ensure that light is coupled into the core. The output end of the hybrid fiber is then transferred to a second alignment stage to be coupled to a receiving SMF, which in turn is connected to a power-meter. The core of the receiving fiber is aligned to maximize the power measured at the power-meter. Further fine-tuning of alignment stages is performed to maximize the power measured at the power-meter, which indicates optimal coupling into and out of the hybrid fiber. UV cured epoxy is then used to permanently fix the input and output end of the hybrid fiber to the launching and receiving SMFs.

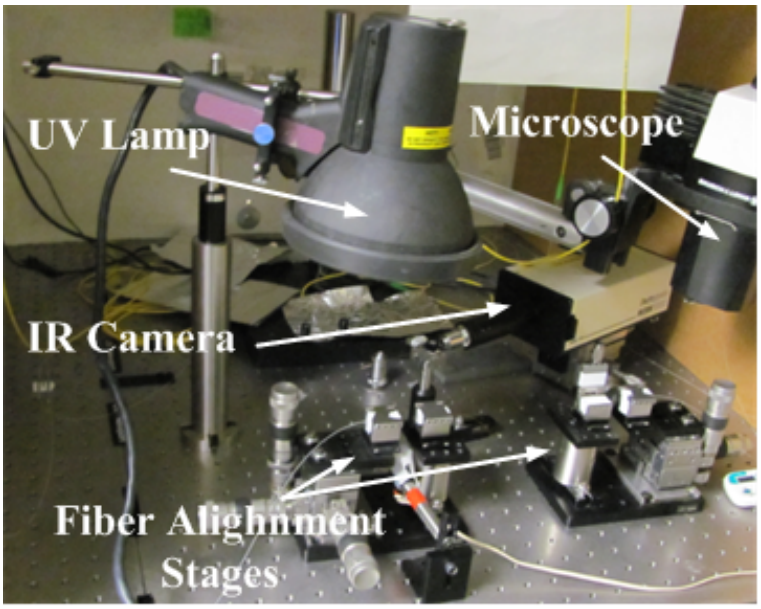

Fig. 4.8 Coupling Setup.

Material Processing Considerations

PMMA has a tendency to absorb water from the surrounding environment because it is porous and water molecules can diffuse in. PMMA foams if it is heat-softened without having been dried due to the formation bubbles that arise from the evaporation of the water absorbed in the PMMA structure, as illustrated in Fig. 4.9. The density of the bubbles decreases as PMMA is partially dried, and no bubbles appear when it is completely dried. PMMA is dried by keeping it for several hours in an oven at a temperature of 80^o C as shown in Fig. 4.10 before being heat-softened.

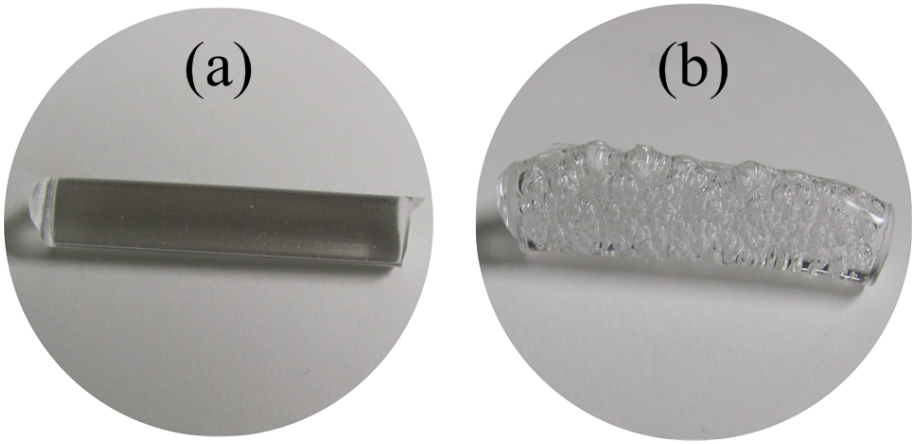

Fig. 4.9 Foaming of PMMA showing a) a PMMA rod before heating, and b) the formation of bubbles in the PMMA rod after heating to 180^o C.

Fig. 4.10 Oven with temperature controller.

In the process of preparing hybrid fibers for tapering, ultraviolet (UV) light cured epoxy is used for permanently fixing the coupling interfaces between PMMA coated As_2Se_3 fiber and SMFs. During this process, the hybrid fiber must be covered to avoid UV exposure because UV light destroys the PMMA polymeric structure. Otherwise, the heat softened PMMA does not flow properly when being tapered and it can not be tapered to small diameters.

As_2Se_3 also has a tendency to absorb water from the surrounding environment due to its porous structure that allows water molecules to diffuse in. A fiber made of As_2Se_3 is dried by placing it in an oven for a duration of 1 hour at a temperature of 140^o C. A dried

As_2Se_3 fiber can be tapered to diameter smaller than 0.5 µm; however, if the fiber is not dried before tapering, the taper breaks before reaching a diameter 0.7 µm.

4.2 Microtaper Design

Figure 4.11 presents a schematic of a hybrid microtaper. It comprises a microwire section where most of the nonlinear effects occur and a transition region between the single-mode fiber and the microwire section. The microtaper is made of a single-mode step-index As_2Se_3 fiber surrounded by a polymer coating made of PMMA. The optimal microtaper parameters are obtained by analyzing the fundamental mode in the microwire section of the microtaper.

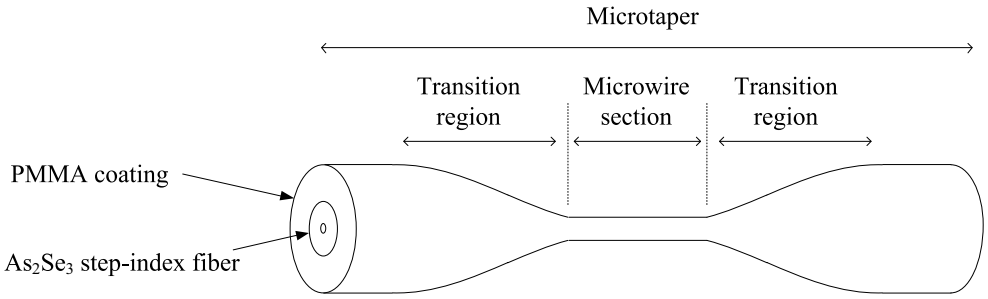

Fig. 4.11 Schematic of the hybrid microtaper geometry.

Determination of the chromatic dispersion and the waveguide nonlinearity involves solving the characteristic equation of an infinite cladding cylindrical waveguide to obtain the propagation constant β, the electric field distribution $\overrightarrow{E}$, and the magnetic field distribution $\overrightarrow{H}$ for the fundamental mode HE_{11} [70]. Solving the characteristic equation takes into account the wavelength dependence of the refractive index of As_2Se_3 obtained from the Sellmier relation

$$n^2_{AsSe}(\lambda) = 1 + \sum_{i=1}^{i=3} A_i^2 \lambda^2 / \left(\lambda^2 - \lambda_i^2\right)$$

where $A_1 = 2.234921$, $A_2 = 0.347441$, $A_3 = 1.308575$, $\lambda_1 = 0.24164$ µm, $\lambda_2 = 19$ µm, and $\lambda_3 = 0.48328$ µm [91], and the refractive index of PMMA obtained from the Cauchy relation

$$n^2_{PMMA} = B_1 + B_2\lambda^2 + B_3\lambda^{-2} + B_4\lambda^{-4} + B_5\lambda^{-6} + B_6\lambda^{-8}$$

where $B_1 = 2.399964$, $B_2 = -8.308636 \times 10^{-2}$, $B_3 = -1.919569 \times 10^{-1}$, $B_4 = +8.720608 \times$

10^{-2}, $B_5 = -1.666411 \times 10^{-2}$, and $B_6 = +1.169519 \times 10^{-3}$ [92], with λ being the wavelength in µm. Figure 4.12 presents the chromatic dispersion (D_c) as a function of ϕ_{AsSe} calculated using [9]

$$D_c = \frac{-\lambda}{c} \frac{d^2 n_{eff}}{d\lambda^2},$$

where $n_{eff} = \beta / k_0$ with k_0 being the wavenumber.

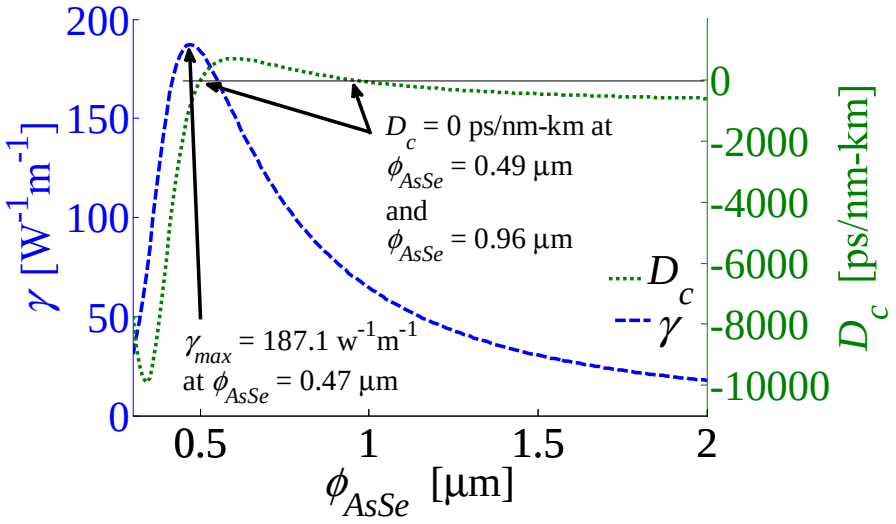

Fig. 4.12 Calculated waveguide nonlinearity parameter and chromatic dispersion of the hybrid microwire as a function of the As_2Se_3 core diameter at a wavelength of 1550 nm.

Also presented in Fig. 4.12 is γ as a function of ϕ_{AsSe} at $\lambda = 1550$ nm calculated using $\gamma = k_0 \bar{n}_2 / A_{eff}$ with $\bar{n}_2$ being the effective material nonlinearity given by [75, 76]

$$\bar{n}_2 = \frac{\varepsilon_0}{\mu_0} \frac{\iint_\infty n_0^2(x,y)\, n_2(x,y) \left(2 \left| \vec{E} \right|^4 + \left| \vec{E}^2 \right|^2 \right) dA}{3 \iint_\infty \left| \left[\vec{E} \times \vec{H}^* \right] \cdot \hat{z} \right|^2 dA},$$

and A_{eff} given by [75, 76]

$$A_{eff} = \frac{\left| \iint_\infty \left[\vec{E} \times \vec{H}^* \right] \cdot \hat{z} dA \right|^2}{\iint_\infty \left| \left[\vec{E} \times \vec{H}^* \right] \cdot \hat{z} \right|^2 dA}$$

where n_0 is the refractive index, n_2 is the material nonlinearity with $n_{2,AsSe} = 1.1 \times 10^{-17}$ m^{2}W^{-1} and $n_{2,PMMA} = -8 \times 10^{-19}$ m^{2}W^{-1} [10, 93], ε_0 and μ_0 are the electric permittivity and the magnetic permeability of free space, respectively, z is the direction of propagation and A is the transverse surface area. Figure 4.12 shows that the optimal As_2Se_3 core diameter to achieve a maximum nonlinearity is $\phi_{AsSe} = 0.47$ µm for which $\gamma = 187.1$ W^{-1}m^{-1}.

Linear losses in the hybrid microtaper arise from various origins: butt-coupling losses, material absorption losses, and adiabaticity losses. Butt-coupling losses occur at the SMF-As_2Se_3 fiber interfaces due to mode mismatch and Fresnel reflection (0.5 dB per interface). Material losses in the hybrid microwire are calculated using

$$\alpha^{dB}_{hybrid} = \Gamma_{AsSe} \times \alpha^{dB}_{AsSe} + \Gamma_{PMMA} \times \alpha^{dB}_{PMMA},$$

where $\Gamma_i = P_i/P_{tot}$ is the confinement factor with P_i being the power fraction of the mode in layer i and P_{tot} the total power of the mode. Figure 4.13 presents the value of α^{dB}_{hybrid} as a function of ϕ_{AsSe} calculated using the attenuation coefficients $\alpha^{dB}_{AsSe} = 0.0085$ dB/cm [10] and $\alpha^{dB}_{PMMA} = 0.5$ dB/cm [94] at $\lambda = 1550$ nm. At the diameter of maximum nonlinearity $\phi_{AsSe} = 0.47$ µm the calculated α^{dB}_{hybrid} for the hybrid microwire is 0.069 dB/cm . Finally, adiabaticity losses may occur in the transition regions where the mode from the single-mode As_2Se_3 fiber is converted into a microwire mode, and back into a single-mode As_2Se_3 fiber mode [31].

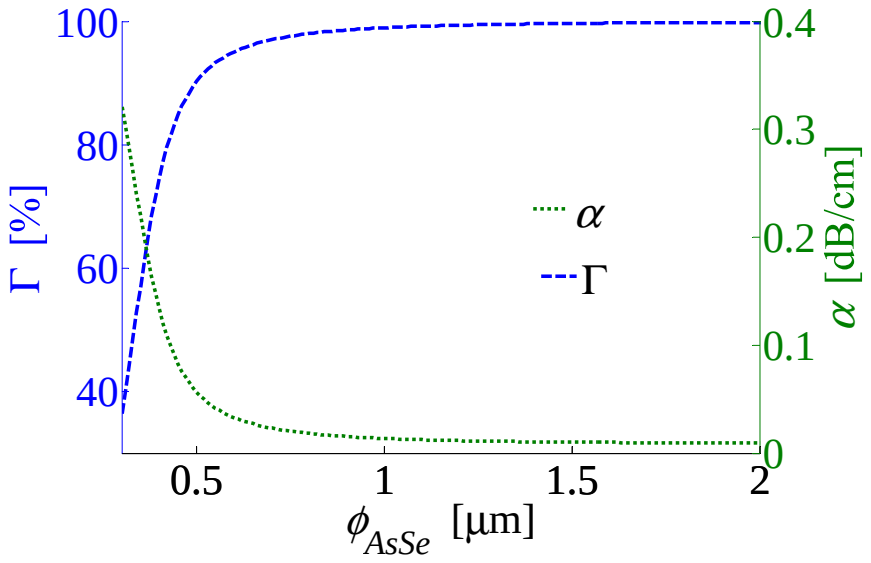

Fig. 4.13 Calculated confinement factor and loss of the hybrid microtaper as a function of the As_2Se_3 core diameter at a wavelength of 1550 nm.

4.3 Adiabaticity Criteria

The changing diameter along the microtaper transition region causes coupling between the fundamental mode and higher order modes which include higher order guided modes and radiation modes [32, 63]. A microtaper is said to be adiabatic if power coupling to higher order modes is negligible. Coupling power to higher order modes causes loss in the power of the fundamental mode propagating in the microtaper [2, 31, 95–100]. Loss in the power of the fundamental mode leads to reduced nonlinear effects, which is undesirable. Moreover, when power is coupled to higher order modes, the waveguide nonlinearity cannot be measured using available characterization techniques. Coupling power to higher order modes can not be completely eliminated in step-index fiber microtapers [100]. However, it has been minimized to negligible values by controlling the rate of change of core and cladding diameters along the microtaper [95].

Loss Mechanisms

There are three main mechanisms that lead to loss in the power of the fundamental mode in the transition region of a microtaper. The first mechanism is the breakdown of the total internal reflection guiding condition $\theta_i > \theta_c$, where θ_i is the incidence angle of a ray at the

core cladding interface and $\theta_c = \sin^{-1}(n_{clad}/n_{core})$ is the critical angle with n_{core} and n_{clad} being the core and cladding refractive indices [98]. The second mechanism is the transfer of power from the fundamental HE_{11} mode to higher order modes with the same symmetry, mainly HE_{12} [32,63]. The third mechanism is the interference between the HE_{11} and HE_{12} modes [2,95]. The severity of all three mechanisms depends on the rate of change of core and cladding diameters along the microtaper axis [31,32,95]. In step-index fibers, if the rate of change of the diameter is changed such that the third mechanism is eliminated, the other two mechanisms are automatically eliminated [32].

Criteria for Adiabatic Microtapers

The interference between the HE_{11} and HE_{12} modes is eliminated if the beat period z_b is much larger than a step Δz along the microtaper axis at any point of the microtaper i.e. $\Delta z \ll z_b$. The beat period z_b, illustrated in Fig. 4.14, is given by $z_b = 2\pi/(\beta_{11} - \beta_{12})$ with β_{11} and β_{12} being the propagation constants of the HE_{11} and HE_{12} modes respectively. The cladding diameter changes by $\Delta\phi_{clad}$ over a step Δz and the inequality $\Delta z/z_b \ll 1$ is expressed as $\Delta z/z_b \leq \Delta\phi_{clad}/\phi_{clad}$ because in most practical tapers $\Delta\phi_{clad}/\phi_{clad} \ll 1$. Hence, at any point of the fiber microtaper the rate of change of cladding diameter must satisfy [95]

$$|d\phi_{clad}/dz| \leq \frac{\phi_{clad}}{2\pi}(\beta_{11} - \beta_{12}). \tag{4.1}$$

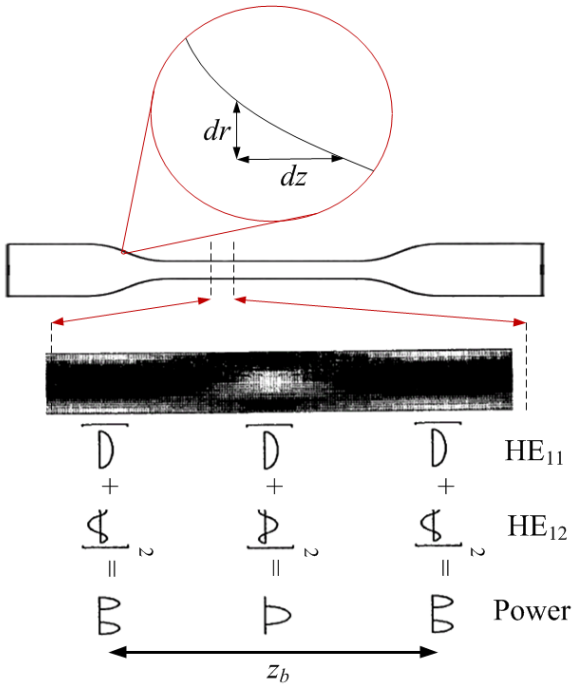

Fig. 4.14 The differential step Δz and the beat length z_b [2]. © [1987] OSA

The Delineation Line

The maximum allowed value of $|d\phi_{AsSe}/dz|$ for hybrid microtapers is plotted as a function of the cladding diameter to obtain a curve known as the delineation line, as presented in Fig. 4.15. If the rate of change of the cladding diameter for a microtaper exceeds the delineation line, then there will be loss in the power of the fundamental mode propagating along the microtaper [31]. If the rate of change of the As_2Se_3 diameter for a microtaper remains below the delineation line, then the loss in the power of the fundamental mode propagating along the microtaper will be negligible [31].

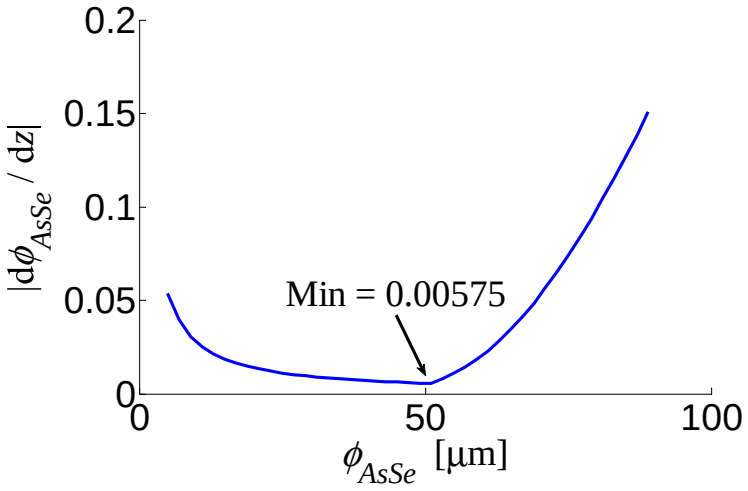

Fig. 4.15 The delineation line for hybrid microtapers.

4.4 Microwire Fabrication and Characterization

Figure 4.16 presents an image of the setup used for tapering hybrid fibers. The tapering setup consists of three motorized translation stages and a resistive heater with a temperature controller. The resistive heater with the temperature controller is used to heat the hybrid fiber to the softening point, two of the motorized translation stages are used to stretch the fiber, and the third one is used to sweep the heater along the fiber length. This setup allows for precise control the microtaper profile including the transition regions and the diameter of the microwire section by tapering the fiber over multiple sweeps as described in Chapter 3. Given a specific microtaper profile, a Matlab program is used to generate a set of files containing information describing each tapering sweep. Then, a LabView program reads the files generated by the Matlab program and uses the information stored in them to control the motorized translation stages and fabricate a microtaper with the prescribed profile.

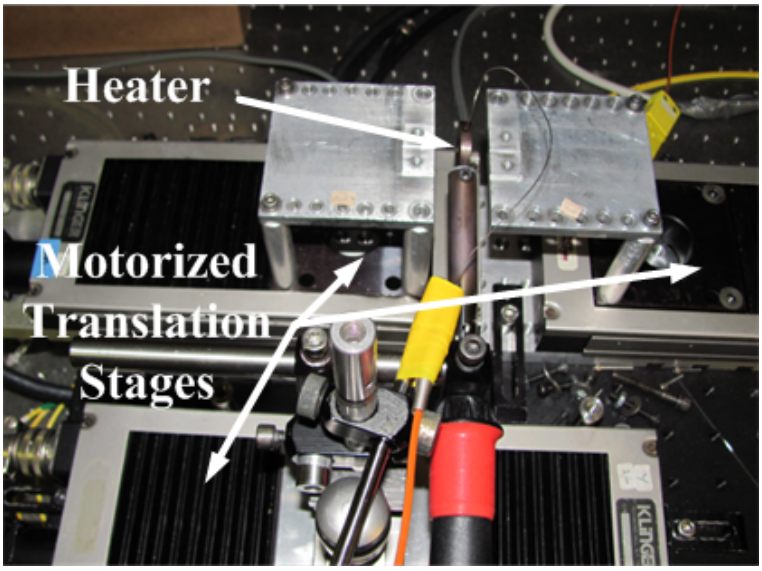

Fig. 4.16 Fiber tapering setup.

The hybrid fiber is tapered adiabatically at a temperature of 190° C until the As_2Se_3 core diameter in the microwire section of the hybrid microtaper reaches the target diameter. A hybrid microtaper is fabricated with microwire section length of 7.0 cm, an As_2Se_3 core diameter of 1.8 µm, and a PMMA cladding diameter of 5.4 µm. Figure 4.17 shows a microscope picture of the hybrid microtaper. The PMMA cladding diameter is sufficiently large to allow handling of the hybrid microtaper without damage.

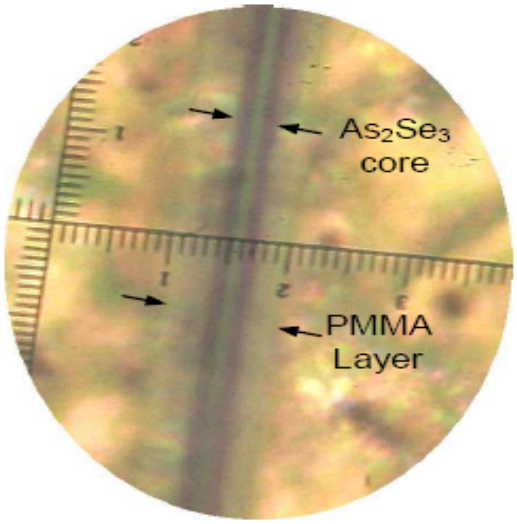

Fig. 4.17 Picture of the wire section of the hybrid microwire sample.

Figure 4.18 shows the setup used to characterize the linear and nonlinear properties of the samples. A mode-locked laser sends pulses of 330 fs full-width at half-maximum at a repetition rate of 20 MHz and at a central wavelength of $\lambda = 1552.4$ nm. The power from the pulses is then adjusted using a variable attenuator and an in-line power meter before injection into the microtaper. The peak power reaching the microwire section of the microtaper can be varied up to a maximum of 50 W. Light from the microtaper output is monitored using an optical spectrum analyzer and a powermeter.

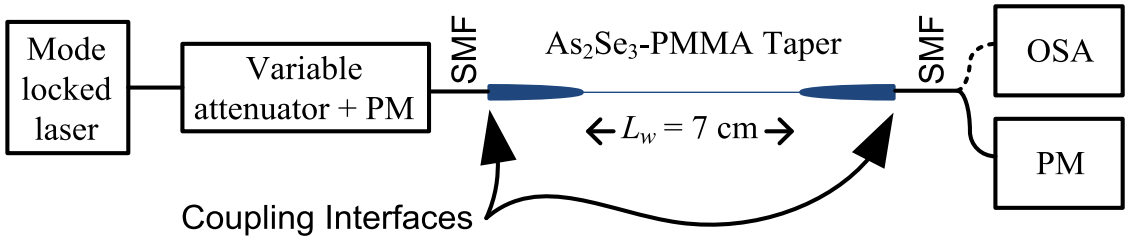

Fig. 4.18 Characterization setup. PM: Power meter, OSA: Optical spectrum analyzer, SMF: Single-mode fiber.

Figure 4.19 shows the optical spectrum of pulses at increasing peak power levels at the output of the hybrid microtaper. To simulate pulse propagation in the microtaper, a split-step Fourier method based on the generalized nonlinear Schrodinger equation is

used [9]

$$\frac{\partial A(z,T)}{\partial z} + \frac{1}{2}\left(\alpha + \frac{\alpha_2}{A_{eff}}\left|A\left(z,T\right)\right|^2\right)A\left(z,T\right) - \sum_{k\geq 2}\frac{j^{k+1}}{k!}\beta_k\frac{\partial^k A(z,T)}{\partial T^k} = j\gamma\left(1+\frac{j}{\omega_0}\frac{\partial}{\partial T}\right)\left[A\left(z,T\right)\int_{-\infty}^{T}R\left(T-T'\right)\left|A\left(z,T'\right)\right|^2 dT'\right].$$

where $A\left(z,T\right)$ is the electric field envelope as a function of distance z along the fiber and time T with respect to the moving frame of reference. The parameter ω_0 is the angular carrier frequency, $\beta_n\left(\omega_0\right)$ is the n^{th} propagation constant derivative at angular frequency ω_0. Parameters α and α_2 are the linear and two-photon absorption coefficients. The nonlinear response function

$$R\left(t\right) = \left(1-f_R\right)\delta\left(t\right) + f_R h\left(t\right)$$

includes both the instantaneous $\delta\left(t\right)$ Kerr contribution and the delayed Raman contribution

$$h\left(t\right) = \left[\left(\tau_1^2+\tau_2^2\right)/\left(\tau_1\tau_2^2\right)\right]\exp\left(-t/\tau_2\right)\sin\left(t/\tau_1\right)$$

where $\tau_1 = 23.3$ fs, $\tau_2 = 230$ fs, and $f_R = 0.1$ [9, 10]. In the simulations, the pulse is propagated in the SMF fiber as well as in the hybrid microtaper, transition region and microwire section, each with appropriate values of γ and D_c. No higher order of β than β_3 is required to ensure a good agreement between experiment and theory. The split-step Fourier method is used to fit the experimental data with a good agreement and lead to $\gamma_{wire} = 22$ $\mathrm{W^{-1}m^{-1}}$, $A_{eff} = 1.4$ µm^2, $D_c = -950$ ps/nm-km ($\beta_2 = 1210$ ps^2/km), $\beta_3 = 2.2$ ps^3/km. In the wire section of this microtaper, 100% of the power is propagating in the As_2Se_3 core and no significant fraction in the PMMA cladding, thus leading to a linear attenuation coefficient of $\alpha_{hybrid}^{dB} = 0.0085$ dB/cm. The value provided for γ_{wire} represents the value in the microwire section of the microtaper, where 93% of the nonlinear phase-shift accumulates. The 7% remaining is accumulated in the transition regions of the microtaper near the wire section.

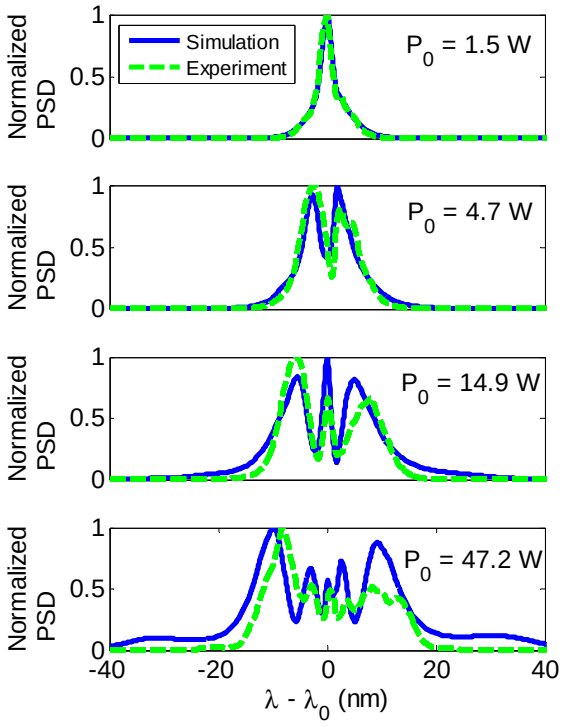

Fig. 4.19 Output pulse spectra of the hybrid microtaper for increasing peak power levels. Dashed line: experiment, solid line: simulation.

4.5 Super-Continuum Generation

A second hybrid microtaper is fabricated with microwire section length of 9.7 cm, an As_2Se_3 core diameter of 0.8 µm, and a PMMA cladding diameter of 2.4 µm. The setup in Fig. 4.18 is also used to sends pulses centered at $\lambda = 1552.4$ nm with a full-width at half-maximum of 330 fs at a repetition rate of 20 MHz into the second microwire and the output is observed using an optical spectrum analyzer. Figure 4.20 presents the output spectra of the second hybrid microtaper showing a supercontinuum with a 20 dB spectral width greater than 400 nm. The split-step Fourier method with $\gamma_{wire} = 133$ $W^{-1}m^{-1}$, $D_c = -160$ ps/nm-km ($\beta_2 = 205$ ps^2/km), $\beta_3 = 3.8$ ps^3/km, $A_{eff} = 0.34$ μm^2, and a loss $\alpha^{dB}_{hybrid} = 0.018$ dB/cm are used to simulate pulse propagation in the second microtaper as shown in Fig. 4.21.

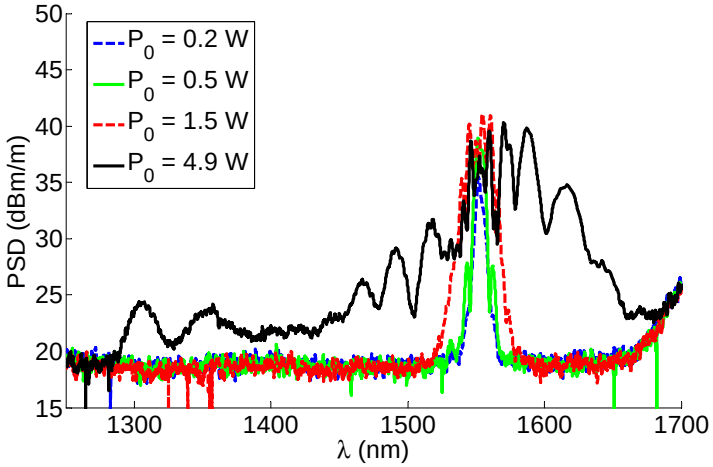

Fig. 4.20 Output pulse spectra of the hybrid microtaper #2 for increasing peak power levels.

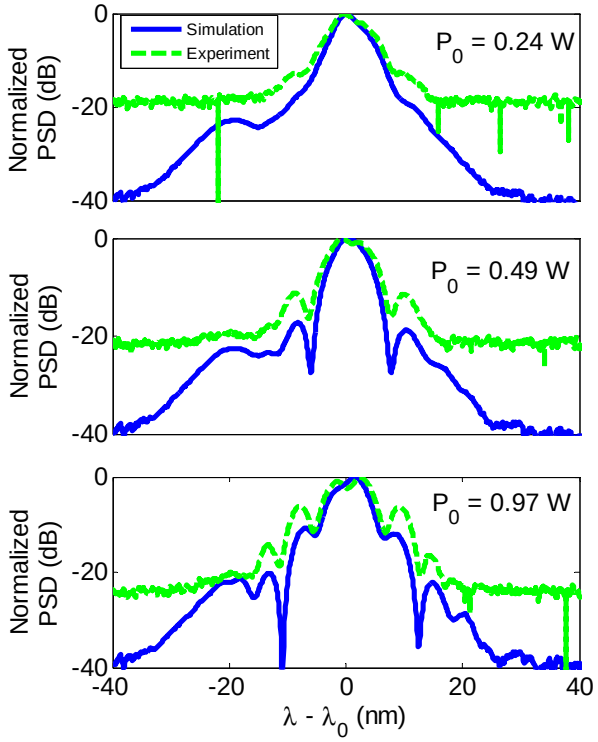

Fig. 4.21 Experimental and simulation results of pulse spectra at the output of the second hybrid microtaper. Dashed line: experiment, solid line: simulation.

4.6 Conclusion

We reported the first hybrid As_2Se_3-PMMA micowires providing an ultrahigh waveguide nonlinearity, sufficient mechanical robustness for normal handling, and reduced sensitivity to the surrounding environment. The polymer coating made of PMMA has a softening temperature compatible with As_2Se_3 and enables stretching of both materials simultaneously. Hybrid microwires having an As_2Se_3 core diameters of 1.8 µm and 0.8 µm were fabricated leading to waveguide nonlinearity parameters of $\gamma = 22$ $W^{-1}m^{-1}$ and $\gamma = 133$ $W^{-1}m^{-1}$ respectively. From theory, the maximum waveguide nonlinearity parameter could even be increased up to $\gamma_{wire} = 187$ $W^{-1}m^{-1}$. Hybrid As_2Se_3-PMMA microwires of a few cm, with their high waveguide nonlinearity parameter and group-velocity dispersion that is broadly variable while keeping a large waveguide nonlinearity, are foreseen as a key element in any Kerr-based nonlinear device.

Chapter 5

Hybrid Microwires from Multi-Mode Hybrid Fibers

In the previous chapter, we have reported the fabrication and optical characterization of the first hybrid As_2Se_3-PMMA microtaper, prepared by tapering a single-mode step-index As_2Se_3 fiber that is coated with a PMMA layer [19]. Figure 5.1(a) presents a schematic of the hybrid microtaper fabricated from a PMMA coated step-index As_2Se_3 fiber. In the fabrication process of the hybrid microwire, a single-mode step-index As_2Se_3 fiber is used to ensure single-mode propagation from the fiber input to the microwire and from the microwire back to the fiber output, given that the taper transition region satisfies the adiabaticity criteria [31, 32]. In this case though, the transmission of the resulting hybrid microwire depends upon the As_2Se_3 fiber quality and design.

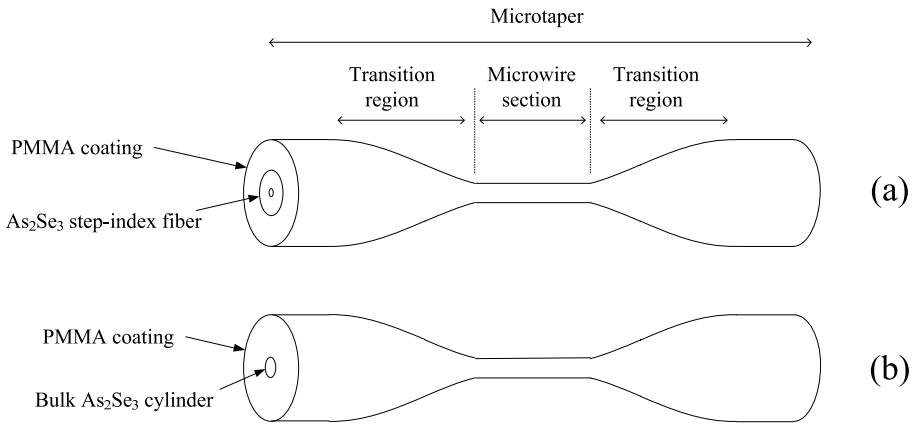

Fig. 5.1 Schematic of hybrid microtapers. In a), a hybrid microtaper with a PMMA coated single-mode step-index As_2Se_3 fiber. In b), a hybrid microtaper with a PMMA coated bulk As_2Se_3 cylinder.

Hybrid microtapers with single-mode transmission can also be fabricated from a multi-mode As_2Se_3-PMMA fiber composed of a bulk As_2Se_3 cylinder that is coated with a PMMA layer, as presented in Fig. 5.1(b). The multi-mode hybrid fiber must be tapered sufficiently such that only the fundamental mode is preserved in the As_2Se_3 core of the microwire. Single-mode transmission in tapered multi-mode fiber structures was first observed and studied in tapered fused couplers [22,34]. Later, different tapering schemes have been used to filter out higher order modes in multi-mode fibers and achieve single-mode transmission [35–37].

In this chapter, we report single-mode transmission and high nonlinearity in tapered multi-mode As_2Se_3-PMMA fibers. We fabricate multi-mode and large refractive index contrast hybrid fibers with an As_2Se_3 core and a PMMA cladding. The As_2Se_3 core diameter is designed for optimal coupling between the fundamental mode of the hybrid fiber and the fundamental mode of an SMF. A segment of this multi-mode fiber is then tapered down into a wire until the As_2Se_3 core sustains single-mode transmission. This microwire with SMF-compatible pigtails is then characterized and used as the nonlinear element of a Kerr-shutter to a achieve optical switching based on nonlinear polarization rotation [101].

5.1 Multi-Mode AsSe-PMMA Fiber Design

A primary design criterion for the As_2Se_3-PMMA multi-mode fiber is the maximization of the coupling efficiency between the fundamental mode of an SMF and the fundamental mode of the hybrid fiber. The coupling efficiency and the reflectivity are calculated using [102]

$$\eta = \frac{4\beta_i\beta_t}{(\beta_i+\beta_t)^2}\frac{\left[\int\int \vec{E}_t\vec{E}_i^* dxdy\right]^2}{\left[\int\int \vec{E}_t\vec{E}_t^* dxdy\right]\left[\int\int \vec{E}_i\vec{E}_i^* dxdy\right]}$$

$$R = \frac{(\beta_i-\beta_t)^2}{(\beta_i+\beta_t)^2}$$

where β, $\vec{E}$ are the propagation constant and the electric field distribution of the fundamental mode, and the subscripts i and t stand for the incident and transmitted light. Fig. 5.2 shows the coupling efficiency and the reflectivity as a function of the As_2Se_3 core diameter (ϕ_{AsSe}). Optimal coupling is achieved when $\phi_{AsSe} = 15.5$ µm with a coupling loss of 0.66 dB per facet from which 0.46 dB is due to reflection and the remaining 0.2 dB is due to mode mismatch. In practice, there are other sources of loss such as lateral misalignment between the cores, a gap between the facets of the two fibers, angular misalignment between the axes of the two fibers, a scratched fiber facet, a non planar fiber facet, or an angled facet, which lead to extra loss at each coupling facet.

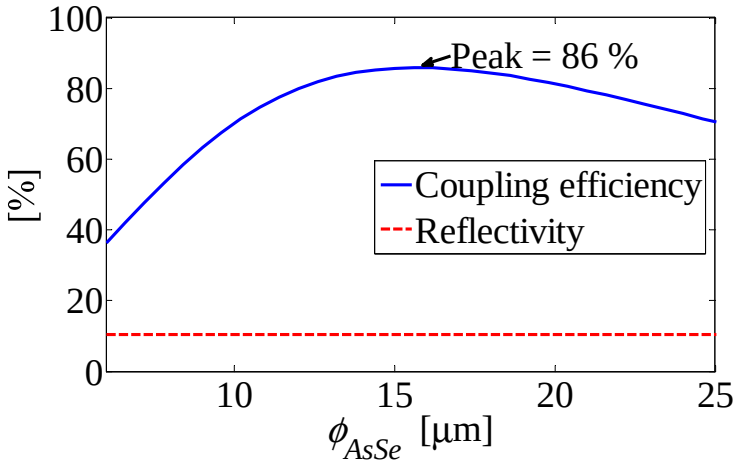

Fig. 5.2 Calculated coupling efficiency and reflectivity as a function of the As_2Se_3 core diameter.

5.2 Microtaper Design

To achieve single-mode transmission in tapered multi-mode As_2Se_3-PMMA fibers, the wire section must exclusively confine the fundamental mode. Moreover, there must be no power transfer between the fundamental mode and higher order modes in the transition region and multi-mode section of the taper. The wire section exclusively confine the fundamental mode when $\phi_{AsSe} \leq 0.49$ µm which corresponds to a normalized frequency $V = \pi\phi_{AsSe}\left(n_{AsSe}^2 - n_{PMMA}^2\right)^{0.5}/\lambda \leq 2.4$ [70], where n_{AsSe} and n_{PMMA} are the refractive indices of the As_2Se_3 core and the PMMA cladding, respectively. Moreover, to avoid power transfer between the fundamental mode and higher order modes there must be no sharp bends in the multi-mode section of the taper, and the slope of the taper transition region must satisfy the condition

$$\frac{d\phi_{AsSe}}{dz} < \frac{\phi_{AsSe}}{2\pi}\left(\beta_{11} - \beta_{12}\right)$$

where β_{11} and β_{12} are the propagation constants of the modes HE_{11} and HE_{12}, respectively. Figure 5.3 shows the maximum allowed taper slope for every value of the core diameter, also known as the delineation line. If the taper slope is made equal to the delineation line, the transition region over which ϕ_{AsSe} decreases from 15.5 µm to 0.49 µm can be made shorter than 1.0 mm. For practical reasons and to guarantee an adiabatic propagation of the fundamental mode in the transition region, the slope of the transition region from the initial diameter to the final diameter in the fabricated tapers is always set to $|d\phi_{AsSe}/dz| = \phi_{AsSe}/L_0$ with $L_0 = 1$ cm.

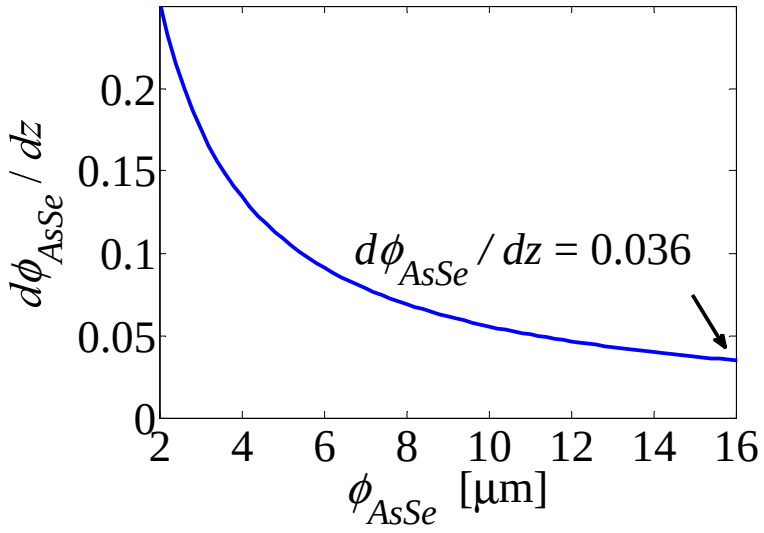

Fig. 5.3 Maximum allowed taper slope as a function of the As_2Se_3 core diameter for adiabatic transformation of the fundamental mode in the taper transition region.

Calculated value of chromatic dispersion, waveguide nonlinearity, and material losses in hybrid microwires were presented in Section 4.2. Figure 5.4 presents a magnified version of Fig. 4.12 to show D_c and γ the region of interest, $\phi_{AsSe} < 0.5$ µm, where the As_2Se_3 core confines exclusively the fundamental mode. The diameter $\phi_{AsSe} = 0.47$ µm that corresponds to the maximum achievable nonlinearity lies in the region where the microwire is single-mode. The chromatic dispersion is normal in this region. Moreover, Fig. 5.5 presents a magnified version of Fig. 4.13 with emphasis on the value of α^{dB}_{hybrid} in the region of single-mode operation. Significant percentage of the mode power propagates in the PMMA layer when $\phi_{AsSe} < 0.5$ µm, potentially providing additional functionality in the microwire by using doped PMMA.

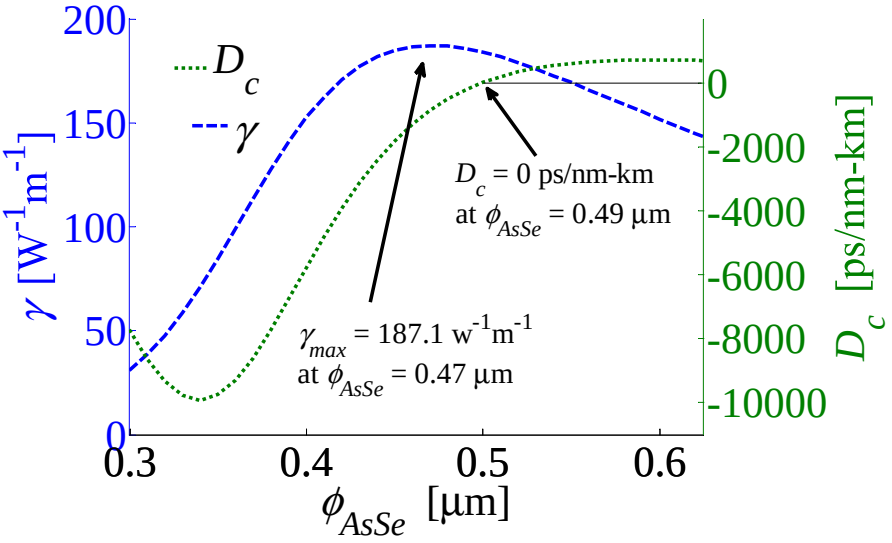

Fig. 5.4 Waveguide nonlinearity parameter and chromatic dispersion of the hybrid microtaper as a function of the As_2Se_3 core diameter at a wavelength of 1550 nm.

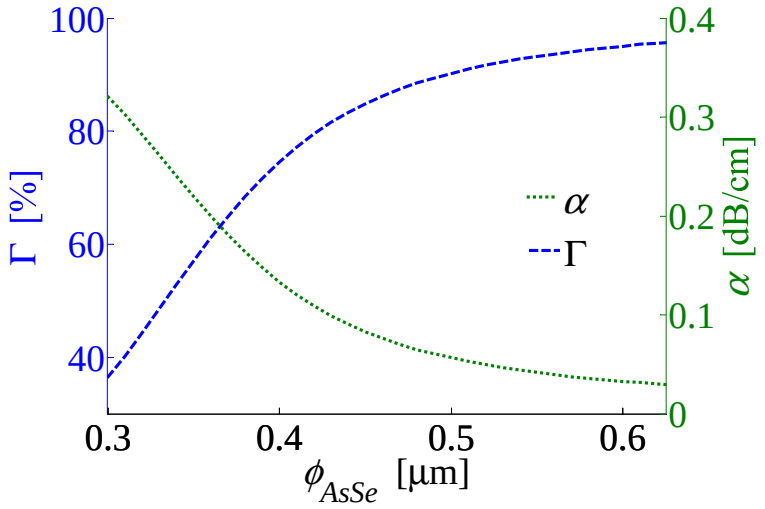

Fig. 5.5 Confinement factor and loss of the hybrid microtaper as a function of the As_2Se_3 core diameter at a wavelength of 1550 nm.

5.3 Hybrid Fiber and Microtaper Fabrication

Figure 5.6 shows a schematic of the setup used for the fabrication of As_2Se_3-PMMA fiber preforms. A cylinder of bulk As_2Se_3 with a diameter of 170 µm is inserted into a commercially available PMMA tube with an inner diameter of 3.2 mm and an outer diameter of 9.5 mm and the assembly is pushed into a funnel heated at 230° C at a constant feed velocity of $v_f = 50$ µm/s. The PMMA tube collapses on the As_2Se_3 cylinder and the composite flows out at the bottom of the funnel. The composite exiting from the bottom of the funnel is captured and is drawn at a constant velocity of $v_d = 225$ µm/s to obtain a preform with a uniform diameter as shown in Fig. 5.7.

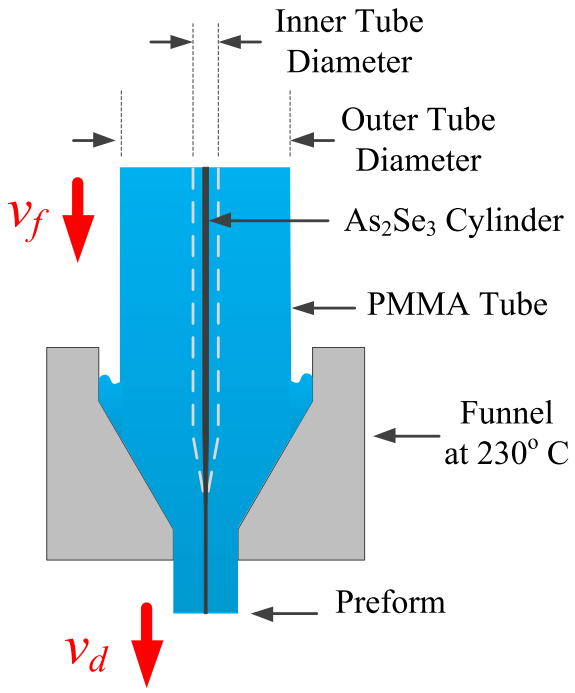

Fig. 5.6 A schematic of the As_2Se_3-PMMA fiber preform fabrication setup.

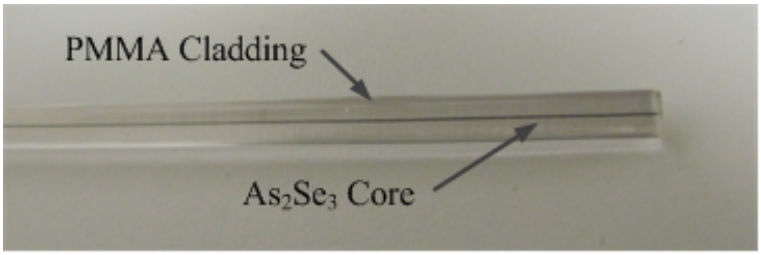

Fig. 5.7 An image of the hybrid fiber preform.

The preform is then drawn at a temperature of 200° C to obtain a hybrid fiber with $\phi_{AsSe} = 15.5$ µm and $\phi_{PMMA} = 472.8$ µm. A 6 cm long sample of this hybrid fiber is cut, and both ends are polished. Figure 5.8 presents an image of the polished facet of the hybrid fiber showing the As_2Se_3 core surrounded by the PMMA cladding. The hybrid fiber sample is tapered using the heat-brush method [19, 23, 24, 34] to obtain a microwire with a $\phi_{AsSe} = 0.45$ µm, $\phi_{PMMA} = 13.7$ µm, and a length of $L_w = 10.0$ cm. With a PMMA layer sufficiently robust for manual handling, the microtaper is manually removed from the tapering setup and transferred to a butt-coupling setup. The input and the output of the microtaper are permanently butt-coupled to SMF-28 fibers using UV-cured epoxy. Finally, the pigtailed microtaper is manually packaged in box to obtain a ready-for-use nonlinear component.

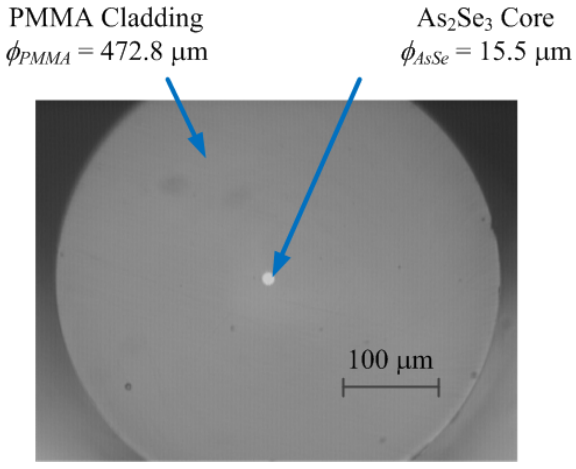

Fig. 5.8 An image of the hybrid fiber cross-section.

5.4 Microtaper Characterization

Figure 5.9 presents the transmission spectrum of the hybrid microtaper between λ = 1500 nm and λ = 1600 nm measured using amplified spontaneous emission noise from an Erbium-doped fiber amplifier and an optical spectrum analyzer with a resolution bandwidth of 0.06 nm. The transmission is maximum at λ = 1530 nm with a loss of 8.4 dB. The transmission decreases at shorter wavelengths because PMMA has an absorption peak at λ = 1390 nm and at longer wavelengths due to a combination of the presence of a PMMA absorption peak at λ = 1620 nm and the decrease of the mode confinement. The transmission spectrum of the microtaper has no interference features indicating single mode transmission.

A loss coefficient of $\sim$ 0.52 dB/cm at λ = 1530 nm is experimentally estimated by the comparison between the transmission losses of multiple hybrid microtapers with identical transition regions and different wire section lengths. This measured loss is 6.3 times higher than the theoretically estimated loss of 0.083 dB/cm from Fig. 5.5. We believe the loss increase arises from imperfections in the fabrication process and the degradation of PMMA. Using the experimentally estimated value of the loss coefficient, propagation in the 10 cm long wire section of the microtaper amounts to 5.2 dB from the total 8.4 dB transmission loss at λ = 1530 nm in Fig. 5.9. The remaining 3.2 dB includes the losses from mode mismatch and reflection at the coupling interfaces (1.3 dB from Fig. 5.2), imperfections in the hybrid fiber facets, and propagation in the 3.5 cm long transition regions of the microtaper.

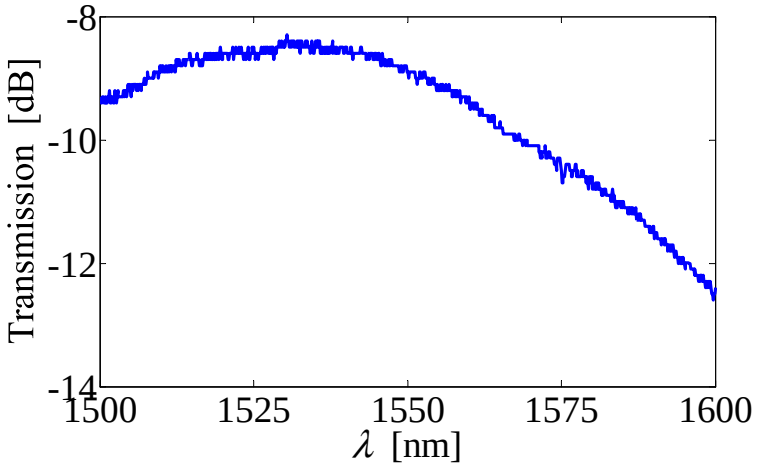

Fig. 5.9 Transmission spectrum of a hybrid microtaper with a wire length of 10 cm and a waist diameter of 0.45 µm.

Figure 5.10 presents a schematic of the setup used to measure γ from the nonlinear phase-shift ϕ_{SPM} accumulated from signal propagation in the microwire [103]. A sinusoidal signal with a duration of 29 ps is formed by combining two continuous wave (CW) lasers at wavelengths $\lambda_1 = 1549.75$ nm and $\lambda_2 = 1550.03$ nm using a 3 dB coupler and then aligning their polarizations using two polarization controllers (PC), PC1 and PC2, and a linear polarizer (LP). The sinusoidal signal is amplitude modulated using a Mach-Zehnder modulator and a square pulse with a duration of 10 ns at a repetition rate of 1 MHz reducing the average power of the signal by 20 dB. The modulated signal is then amplified using an Erbium-doped fiber amplifier and passed to a variable attenuator (VA). The output of the attenuator is launched in the hybrid microtaper and the output of the microtaper is observed using an optical spectrum analyzer.

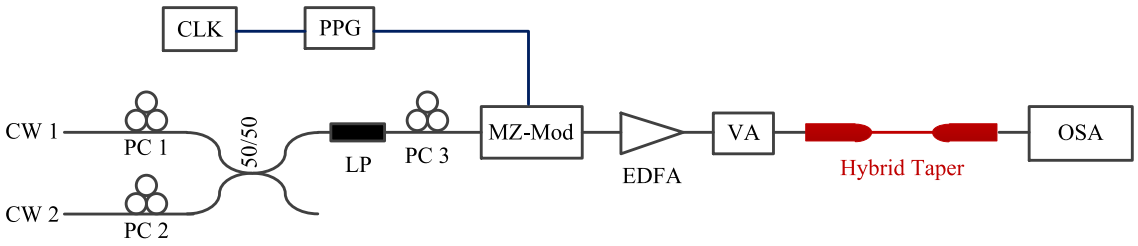

Fig. 5.10 Schematic of the waveguide nonlinearity measurement setup. CW: continuous wave laser, PC: polarization controller, LP: linear polarizer, CLK: electrical clock, PPG: pulse pattern generator, MZ-Mod: Mach-Zehnder modulator, EDFA: Erbium-doped fiber amplifier, VA: variable attenuator, OSA: Optical spectrum analyzer.

Figure 5.11(a) shows the spectral evolution of the sinusoidal signal at the output of the hybrid microtaper at increasing peak power levels. Figure 5.11(b) presents the value of ϕ_{SPM} for each peak power level calculated from I_0 and I_1, which are illustrated in Fig. 5.11, using the equation [103]

$$\frac{I_0}{I_1} = \frac{J_0^2(\phi_{SPM}/2) + J_1^2(\phi_{SPM}/2)}{J_1^2(\phi_{SPM}/2) + J_2^2(\phi_{SPM}/2)} \tag{5.1}$$

where J_0, J_1 and J_2 are the zero, first, and second order Bessel functions of the first kind. Using the experimentally estimated loss of 5.2 dB over the wire section length of 10 cm, the effective length is $L_{eff} = 5.83$ cm. The ratio of nonlinear phase-shift accumulating in the wire section $\phi_{SPM}^{w} = \gamma P_0 L_{eff}$ to the phase-shift in the entire microtaper $\phi_{SPM} = \int \gamma(z)\, P(z)\, dz$ is $\rho = \phi_{SPM}^{w}/\phi_{SPM} = 0.87$. The product $\gamma L_{eff}/\rho = 11.8$ W^{-1} is the slope of the linear fit connecting the experimentally measured values of ϕ_{SPM} in Fig. 5.11(b). The waveguide nonlinearity in the wire section of the microtaper is $\gamma = 11.8 \times \rho/L_{eff} = 176$ W^{-1}m^{-1}, in close agreement with the theoretically calculated value of 185 W^{-1}m^{-1} at $\phi_{AsSe} = 0.45$ µm in Fig. 5.4.

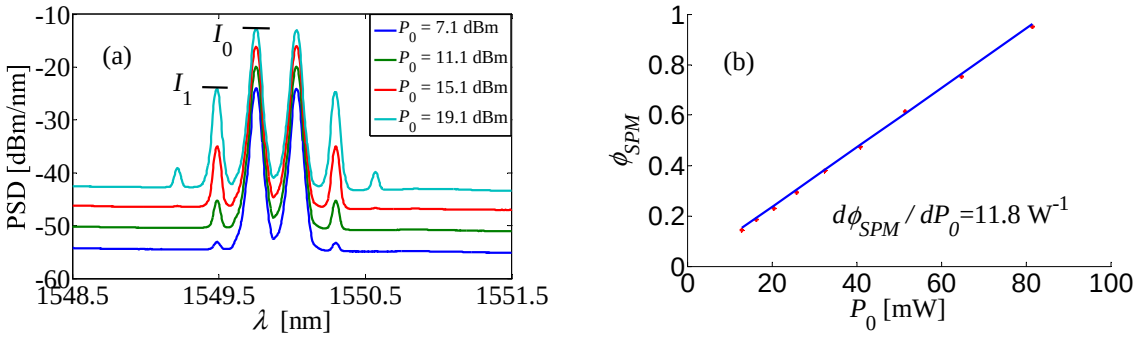

Fig. 5.11 Sinusoidal-signal self-phase modulation measurements showing a) the recorded output spectra of the hybrid microtaper for increasing power levels, and b) the measured ϕ_{SPM} as a function of the peak power of the sinusoidal-signal.

5.5 All-Optical Switching in a Kerr-Shutter

Figure 5.12 presents a schematic of the Kerr-shutter setup [101] used to demonstrate switching by induced polarization rotation in the hybrid microwire. Pump optical pulses with a full-width at half maximum (FWHM) duration of $T_{FWHM} = 5.47$ ns and a repetition rate of $f = 3.3$ kHz at $\lambda = 1535$ nm from a Q-switched laser are combined with a CW laser probe at $\lambda = 1575$ nm using a 3 dB coupler and then launched into the microtaper. When the pump is linearly polarized in the microtaper and the pump peak-power is increased using the variable attenuator, birefringence is induced due to Kerr nonlinearity leading to time dependent birefringence modulation; consequently, the copropagating probe experiences polarization modulation. The polarization-modulated part of the probe is isolated using a linear polarizer which blocks the non-modulated part of the probe leading to pulses at the probe wavelength. A tunable filter is then used to block the pump laser pulses and exclusively pass the probe pulses which are then detected using a photodiode and an oscilloscope. The polarization of the optical pulses from the Q-switched laser, the CW probe laser, and the output of the microtaper are adjusted using PC1, PC2, and PC3 such that the transmitted probe power is zero when the pump laser is OFF, and the peak of the probe pulse is maximum when the pump laser is ON.

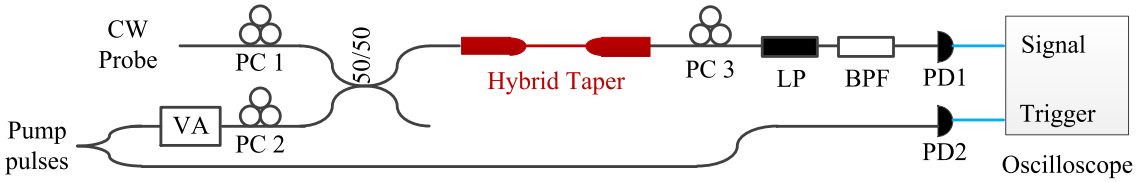

Fig. 5.12 Schematic of the Kerr-shutter setup. CW: continuous wave laser, PC: polarization controller, LP: linear polarizer, VA: variable attenuator, BPF: band-pass filter, PD: photo-diode.

The equation describing the interaction between CW probe and the quasi-CW pump lasers at wavelengths λ_{probe} and λ_{pump} with field amplitudes A and A^{pump}, respectively, is

$$\frac{\partial A_m}{\partial z} = -j\gamma \left(|A_m|^2 + 2\,|A_m^{pump}|^2 + B\,|A_n^{pump}|^2 + B\,|A_n|^2 \right) A_m \tag{5.2}$$

$$\frac{\partial A_m^{pump}}{\partial z} = -j\gamma \left(|A_m^{pump}|^2 + 2\,|A_m|^2 + B\,|A_n^{pump}|^2 + B\,|A_n|^2 \right) A_m^{pump} \tag{5.3}$$

where m and n represent two orthogonal polarization axis with $m \neq n$, and $B = 1$ for a nonbirefringent fiber. Using a linearly polarized pump with $A^{pump} \gg A$ and setting one of the principal axis parallel to the pump polarization, Eq. 5.2 and Eq. 5.3 lead to

$$\frac{\partial A^{pump}}{\partial z} = -j\gamma\,|A^{pump}|^2\,A^{pump}$$

$$\frac{\partial A_\parallel}{\partial z} = -j\gamma \left(2\,|A^{pump}|^2 \right) A_\parallel$$

$$\frac{\partial A_\perp}{\partial z} = -j\gamma \left(|A^{pump}|^2 \right) A_\perp$$

which are solved as

$$A^{pump}(z) = A^{pump}(0)\,e^{-j\gamma P(z) z}$$

$$A_\parallel(z) = A_\parallel(0)\,e^{-j2\gamma P(z) z}$$

$$A_\perp(z) = A_\perp(0)\,e^{-j\gamma P(z) z}$$

where $P(z) = |A^{pump}(z)|^2$, $A_\parallel(z)$ and $A_\perp(z)$ are the amplitudes of probe electric-field components parallel and perpendicular to the pump, respectively. The accumulated nonlinear phase-shift of the pump signal due to propagation in a microtaper is $\phi_{SPM} = \int \gamma(z)\,P(z)\,dz$

and the accumulated nonlinear phase-shifts for the parallel and the perpendicular components of the probe signal are $\phi_{\parallel} = 2\phi_{SPM}$ and $\phi_{\perp} = \phi_{SPM}$.

The birefringence induced by the linearly polarized pump in the microtaper leads to a phase difference of $\Delta\phi_{Birefringence} = \phi_{SPM}$ between the parallel axis and the perpendicular axis to the pump. At the output of the linear polarizer aligned at 45^o from the linearly polarized pump, the probe electric-field amplitude is given by

$$A_{out} = \sqrt{0.5}A_{\parallel}e^{-j2\phi_{SPM}} - \sqrt{0.5}A_{\perp}e^{-j\phi_{SPM}},$$

where $A_{\parallel}$ and $A_{\perp}$ are, respectively, the amplitudes of probe electric-field components parallel and perpendicular to the pump when the pump power is zero. Using $P_{\parallel} = \left|A_{\parallel}\right|^2 = rP_{tot}$ and $P_{\perp} = \left|A_{\perp}\right|^2 = (1-r)\,P_{tot}$, where $P_{\parallel}$ and $P_{\perp}$ are the powers of the probe components parallel and perpendicular to the pump, respectively, r is the ratio of the parallel probe component power to the total probe power, and $P_{tot} = P_{\parallel} + P_{\perp}$ is total probe power, the probe electric-field amplitude becomes

$$A_{out} = \sqrt{\frac{P_{tot}}{2}}\left[\sqrt{r}e^{-j\phi_{SPM}/2} - \sqrt{(1-r)}e^{j\phi_{SPM}/2}\right]e^{-3j\phi_{SPM}/2},$$

and the probe power at the output of the linear polarizer becomes

$$P_{out} = \frac{P_{tot}}{2}\left[1 - 2\sqrt{r}\sqrt{(1-r)}\cos\left(\phi_{SPM}\right)\right].$$

For $r = 0.5$ and using $\phi_{SPM} = \phi_{SPM}^{w}/\rho = \gamma P_0 L_{eff}/\rho$, the output probe power becomes

$$P_{out} = 0.5P_{tot}\left[1 - \cos\left(\gamma P_0 L_{eff}/\rho\right)\right]$$

and full power switching occurs when the pump peak power P_0 reaches a critical power

$$P_c = \pi\rho/\gamma L_{eff}.$$

Figure 5.13(a) shows the probe pulse normalized to the total power of the probe P_{tot} that is measured at PD1 by adjusting PC3 until full probe transmission through the linear polarizer is achieved. Due to the quasi-CW nature of the long pump pulses, power at the center of the probe pulse (P_{cpp}) depends on the peak power P_0 at the center of the pump

pulse following the relation $P_{cpp} = 0.5P_{tot}\,[1 - \cos(\gamma P_0 L_{eff}/\rho)]$. When P_0 reaches P_c, 100% power transmission occurs at the center of the probe pulse and P_{cpp} becomes equal to P_{tot}. As P_0 exceeds P_c, power transmission at the center of the probe pulse decreases while full power transmission occurs at the wings of the probe pulse. Consequently, a depression starts to appears at the center of probe pulse as can be observed in Fig. 5.13(a). Figure 5.13(b) presents the measured power at center of the probe pulses as a function of the peak of the pump pulses. The power at the center of the probe pulse reaches maximum when the pump peak power is $P_0 = 266$ mW leading to $\gamma = \pi\rho/P_0 L_{eff} = 176$ W^{-1}m^{-1} in agreement with the previous measurement. The estimated ratio $P_{cpp}/P_{tot} = 0.5\,[1 - \cos(\gamma P_0 L_{eff}/\rho)]$ is also plotted in Fig. 5.13(b) showing close agreement with experimental results.

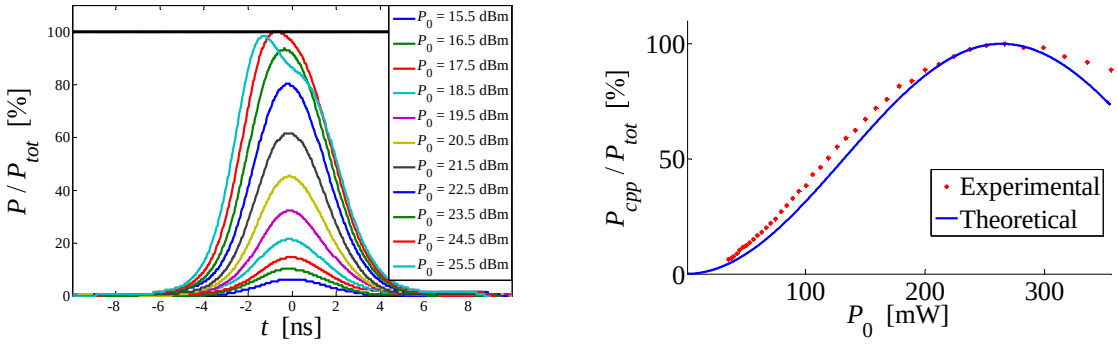

Fig. 5.13 Measured probe pulse at $\lambda = 1575$ nm showing a) the probe pulse shape at increasing pump peak power levels, and b) the power at the center of the converted pulse versus the peak power of the pump pulse.

5.6 Conclusion

A multi-mode As_2Se_3-PMMA fiber has been tapered to achieve single-mode transmission and an ultrahigh waveguide nonlinearity of $\gamma = 176$ W^{-1}m^{-1}. Fabrication of such hybrid microwires from a multi-mode As_2Se_3-PMMA fiber is greatly simplified as it eliminates the need for single-mode step-index As_2Se_3 fibers. Proper design of the initial As_2Se_3 diameter allowed for optimal power coupling into the microwire from an SMF. A Kerr-shutter has been implemented using the fabricated hybrid microwire to demonstrate switching by induced polarization rotation with a 100% switching power of 266 mW.

Chapter 6

Birefringent Eccentric-Core Hybrid Microwires

6.1 Introduction

Fiber structures have been engineered with induced birefringence and high nonlinearity for applications including polarized supercontinuum generation [104, 105], all-optical self-polarization switching with a reduced switching power [106,107], and polarization-entangled photon generation by four-wave mixing [47, 48]. Birefringence in these fiber structures is quantified by both the phase birefringence $b = n_x - n_y$ and the group birefringence $b_g = n_x^g - n_y^g$, where $n_i = \beta_i/k_0$ and $n_i^g = (-\lambda^2/2\pi)\, d\beta_i/d\lambda$ are the effective and the group refractive indices, respectively, β_i is the propagation constant of the fundamental mode, the subscript i represents the principal polarization axes x and y, $k_0 = 2\pi/\lambda$ is the wavenumber, and λ is the wavelength [108]. Nonlinearity is quantified using the waveguide nonlinearity parameter γ given by $\gamma = k_0 n_2/A_{eff}$, where A_{eff} is the modal effective area and n_2 is the material nonlinearity [9].

Two main approaches have been proposed to induce birefringence in an optical waveguide.The first approach is based on applying permanent mechanical stress on the core, as is the case for panda fibers [109–112] and bow-tie fibers [110,113]. The second approach makes use of geometrical asymmetry in the cross-sectional refractive-index distribution, as is the case for elliptical microwires [114], eccentric-core fibers [44–46], side-tunnel fibers [115], asymmetric photonic crystal fibers [116], and asymmetric photonic band-gap fibers [117].

In the last chapter, a high waveguide nonlinearity of $\gamma = 176$ W^{-1}m^{-1} was demonstrated in hybrid As_2Se_3-PMMA microwires composed of an As_2Se_3 core and a PMMA cladding [19, 33]. High birefringence can be achieved in such hybrid structures by placing the As_2Se_3 core close to the air-PMMA interface, and thus forming an eccentric-core hybrid microwire (ECHM). Figure 6.1 presents a schematic of a hybrid microwire with a concentric core [Fig. 6.1(a)] and an eccentric core [Fig. 6.1(b)]. In this chapter, we report the fabrication and characterization of ECHMs with high birefringence and high nonlinearity, using the hybrid As_2Se_3-PMMA technology platform. We report experimental results of group birefringence up to $b_g = 0.018$ and a waveguide nonlinearity of $\gamma = 180$ W^{-1}m^{-1}.

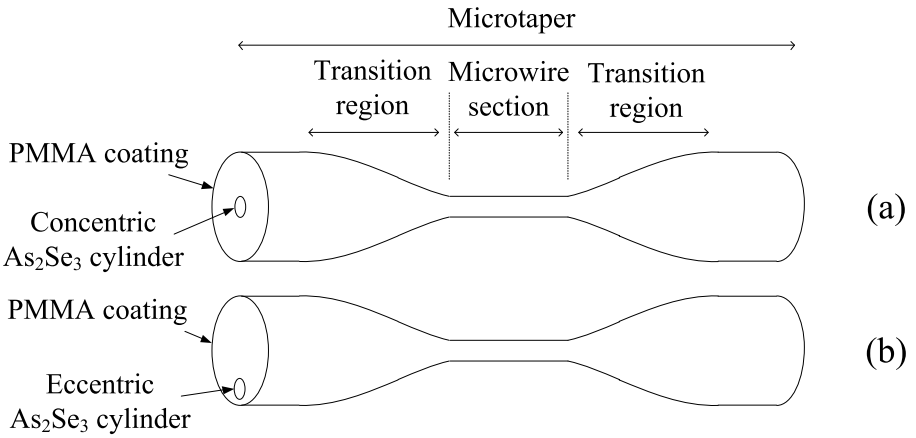

Fig. 6.1 Schematic of hybrid microtapers with a) an concentric core and b) an eccentric core.

6.2 Birefringence Design

Figure 6.2(a) presents a schematic of the cross-section of an eccentric-core As_2Se_3-PMMA microwire. The main geometrical parameters used in the design of an ECHM are the As_2Se_3 core diameter (ϕ_{AsSe}), the PMMA cladding diameter (ϕ_{PMMA}), and the edge separation (s) defined as the shortest distance between the core and cladding edges. The tangential vector finite-element method [80, 81] is implemented and used for the calculation of the effective and group refractive indices of the orthogonal modes and determine b and b_g as a function ϕ_{AsSe}, ϕ_{PMMA}, s, and λ. Figure 6.2(b) and Fig. 6.2(c) present sample meshes used to analyze ECHMs. The mesh in Fig. 6.2(c) is used for the analysis of the ECHM modes when $\phi_{PMMA} > 4.0$ µm, allowing for precision and reasonable calculation time.

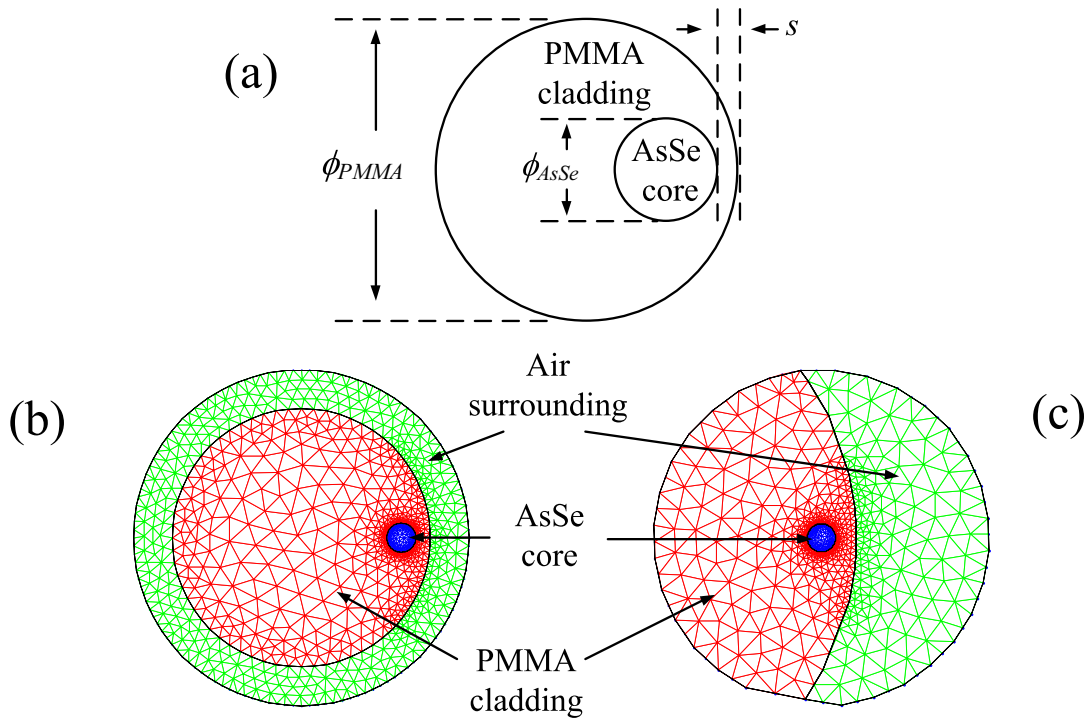

Fig. 6.2 In a), a schematic of an ECHM. In b) and c), sample meshes used in the finite-element analysis of ECHMs.

The tangential vector finite-element method is also used for the calculation of the vectorial field distribution of the modes sustained by the ECHM. The vectorial field distribution is essential for the identification of the modes and their polarization orientation. Figure 6.3(a) and Fig. 6.3(b) present the calculated electric field distribution for the x-polarized and y-polarized fundamental modes of an ECHM. The z-component of the electric field (E_z) is plotted as contours, and the transverse component of the electric field ($\vec{E}_t$) that lies in the plane of the fiber cross-section is plotted as vectors. The distribution symmetry of E_z with respect to the x-axis is odd for the x-polarized mode and even for the y-polarized mode; therefore, the two orthogonal modes are sometimes denoted as the odd and even modes [45, 118].

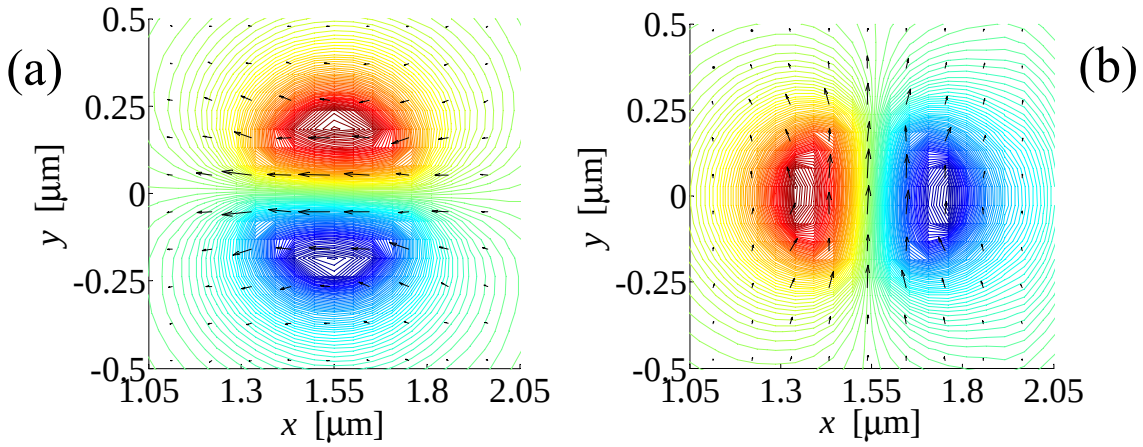

Fig. 6.3 The electric field distribution for a) the x-polarized and b) the y-polarized fundamental modes of an ECHM.

Birefringence engineering is advantageous for specific applications of nonlinear processing in birefringent fiber structures. For example, engineering the values of both b and b_g enables the selection of the wavelength at which the phase matching condition for four-wave mixing is satisfied [49, 50]. Also, it is advantageous to maintain $b_g = 0$ while b is large for applications involving the propagation of pulses with a sub-picosecond duration [108]. Numerical calculations show that ECHMs provide high birefringence and great flexibility in the design of b and b_g.

Figure 6.4 presents both b and b_g as a function of λ in the wavelength range between $\lambda = 1250$ nm and $\lambda = 1600$ nm for an ECHM with $\phi_{AsSe} = 0.30$ µm, $\phi_{PMMA} = 10.0$ µm, and $s = 0.225$ µm. The value of b varies with wavelength reaching a peak of $b = 0.0226$ at $\lambda = 1445$ nm. The value of b_g becomes zero at $\lambda = 1420$ nm while still maintaining the near maximum $b = 0.0224$. The sign of b_g changes at $\lambda = 1420$ nm indicating that the slow axis becomes the fast axis and vice versa. The value of b_g is related to b using $b_g = b - \lambda db/d\lambda$ and, in eccentric core microwires, is mainly dependent on the dominant term $\lambda db/d\lambda$. The term $\lambda db/d\lambda$, and consequently b_g, becomes zero and changes sign when $b\,(\lambda)$ is close to maximum.

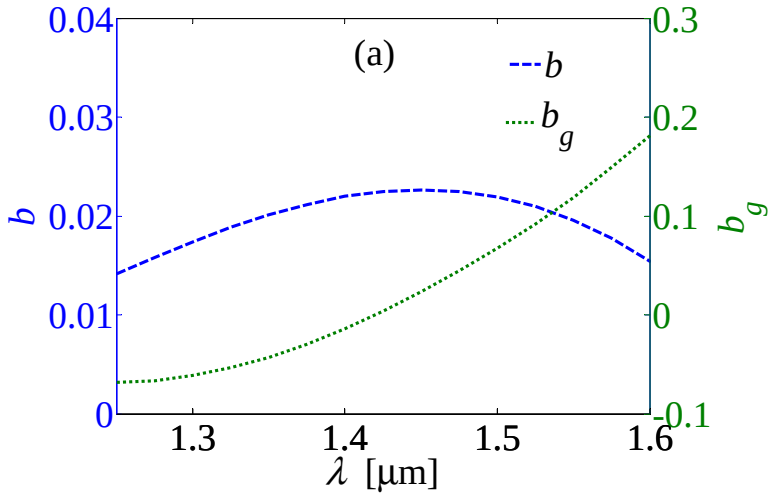

Fig. 6.4 Calculated b and b_g of an ECHM as a function of λ for $\phi_{AsSe} = 0.30$ µm, $\phi_{PMMA} = 10.0$ µm, and $s = 0.225$ µm.

The As_2Se_3 core diameter ϕ_{AsSe} and the edge separation s can be used to engineer the birefringence. Figure 6.5 presents both b and b_g as a function of ϕ_{AsSe} for an ECHM with $\phi_{clad} = 10$ µm and different s values at $\lambda = 1550$ nm. The value of b is positive for all values of ϕ_{AsSe} and s indicating that the x-polarized mode always has a lower phase velocity. Unlike b, the value of b_g can be negative, positive, or zero depending on the values of ϕ_{AsSe} and s. For example, an ECHM with $s = 0.05$ µm has $b_g < 0$ at large ϕ_{AsSe} reaching a negative peak of $b_g = -0.097$ as ϕ_{AsSe} decrease to $\phi_{AsSe} = 0.42$ µm. The value of b_g continues to vary as ϕ_{AsSe} reduces below $\phi_{AsSe} = 0.42$ µm becoming zero at $\phi_{AsSe} = 0.36$ µm and reaching a positive peak of $b_g = 0.255$ at $\phi_{AsSe} = 0.30$ µm.

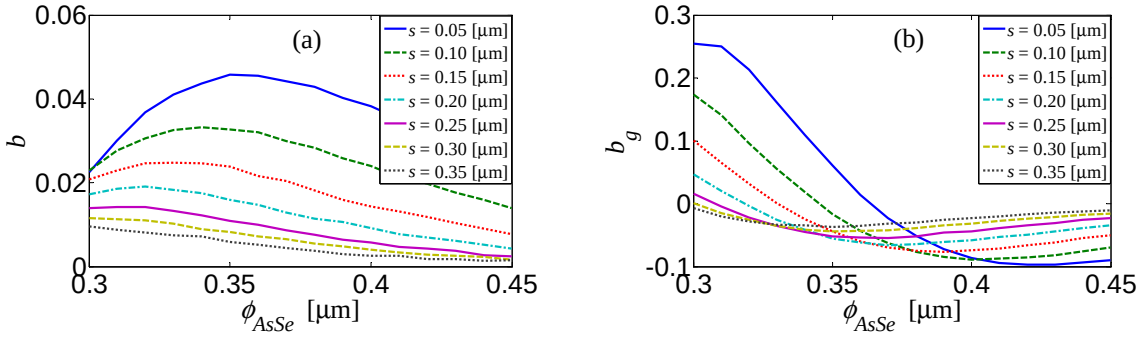

Fig. 6.5 Calculated a) b, and b) b_g of an ECHM as a function of ϕ_{AsSe} for $\phi_{clad} = 10.0$ µm and different values of s at $\lambda = 1550$ nm.

Figure 6.6 presents b and b_g as a function of s for an ECHM with different ϕ_{AsSe} and $\phi_{PMMA} = 10.0$ µm at $\lambda = 1550$ nm. The value of b is positive for all s and is increased by reducing s. A shorter s increases the percentage mode power that propagates in the surrounding air making the ECHM sensitive to the surrounding environment. The cladding diameter can also be used to engineer birefringence; however, $\phi_{PMMA} \geq 10.0$ µm is always used to guarantee the ECHM is mechanically robust. Numerical calculations show that the variation of ϕ_{PMMA} above $\phi_{PMMA} = 4.0$ µm has a negligible impact on b and b_g; therefore, ϕ_{PMMA} is not as critical as ϕ_{AsSe} and s for engineering birefringence.

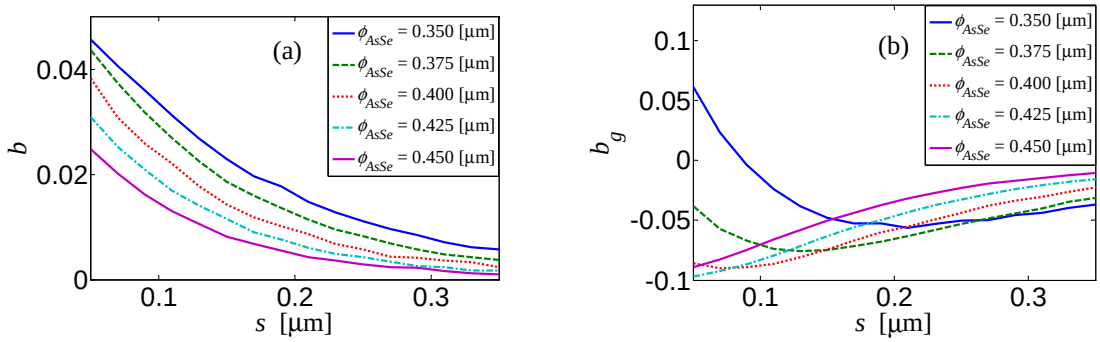

Fig. 6.6 Calculated a) b, and b) b_g of an ECHM as a function of s for different ϕ_{AsSe} and $\phi_{PMMA} = 10.0$ µm at $\lambda = 1550$ nm.

6.3 Eccentric-Core Hybrid Fiber and Microwire Fabrication

Figure 6.7(a) presents a schematic of the setup used for the fabrication of eccentric-core As_2Se_3-PMMA fiber preforms [33]. A cylinder of bulk As_2Se_3 with a diameter of 170 µm is inserted into a PMMA tube with an inner diameter of 0.5 mm and an outer diameter of 1.5 mm. Asymmetry is provided by thermally fusing this PMMA tube to a PMMA rod with a diameter of 9.5 mm, as illustrated in Fig. 6.7(a). The assembly is vertically pushed into a funnel heated at 230° C at a constant feed velocity of $v_f = 50$ µm/s. The PMMA tube collapses on the As_2Se_3 cylinder and the composite flows out at the bottom of the funnel. The composite exiting from the bottom of the funnel is captured and is drawn at a constant velocity of $v_d = 225$ µm/s to obtain a preform with a uniform cross-section. The preform is then drawn at a temperature of 220° C to obtain an eccentric-core hybrid fiber (ECHF) with $\phi_{AsSe} = 15.5$ µm, $\phi_{PMMA} = 445.8$ µm, and $s = 10.7$ µm. Figure 6.7(b) presents an image of the cross-section of the ECHF showing the As_2Se_3 core surrounded

by the PMMA cladding. Figure 6.7(b) also presents a magnified image of the core showing the separation between the edges of the core and the cladding.

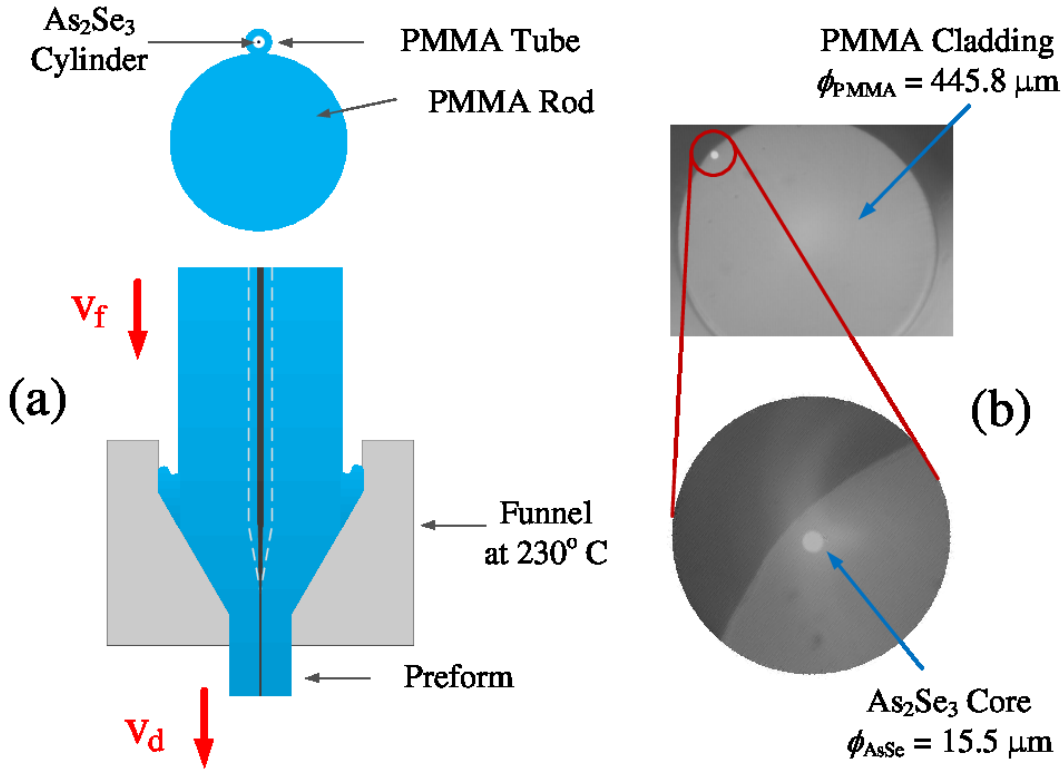

Fig. 6.7 a) A schematic of the preform fabrication setup for ECHFs. b) An image of the ECHF cross-section with a magnified image of the As_2Se_3 core.

The core diameter of $\phi_{AsSe} = 15.5$ µm maximizes the coupling efficiency between the fundamental mode of a standard single-mode silica fiber and the fundamental mode of an ECHF [33]. For $\phi_{AsSe} = 15.5$ µm, the ECHF is multi-mode and is tapered such that the As_2Se_3 core in the wire section exclusively confines the fundamental mode [33]. A 6 cm long sample of the ECHF is cut, and both ends are polished. The input and the output of the microtaper are permanently butt-coupled to standard single-mode silica fibers using UV-cured epoxy. The ECHF sample is tapered using the heat-brush method [19, 23, 24, 34] to obtain a microwire with $\phi_{AsSe} = 0.45$ µm, $\phi_{PMMA} = 12.9$ µm, $s = 0.31$ µm, and a length of $L_w = 10.0$ cm. The slope of the transition region from the initial diameter to the final diameter in the fabricated tapers is set to $|d\phi_{AsSe}/dz| = \phi_{AsSe}/L_0$ with $L_0 = 1$ cm to ensure adiabatic propagation of the fundamental mode [31–33]. At the end of the tapering

process, the microtaper is packaged in a box to obtain a ready-to-use highly birefringent and highly nonlinear component.

Figure 6.8 presents the transmission of an eccentric-core hybrid microtaper as a function of extension obtained by measuring the power of a laser at $\lambda = 1530$ nm transmitted through the hybrid fiber while tapering. An oscillatory transmission is observed due to the interference between the modes propagating in the fiber. During the tapering process, the accumulated phase-differences between the different modes change and the transmission reaches a maximum whenever the phase differences increase by an integer multiple of 2π. All modes except the fundamental mode are cut off when $\phi_{AsSe} < 0.5$ µm indicating single-mode operation. The transmitted power through the taper drops due to spreading of the fundamental mode into the PMMA layer leading to a total transmission loss of 8.0 dB. Similar to concentric-core microtapers, the loss coefficient in the microwire section is ~ 0.52 dB/cm which is 6.3 times higher than the theoretically calculated value of 0.083 dB/cm [33]. We believe the higher loss arises due to the partial crystallization of the PMMA under quiescent conditions as it cools after being heat-softened and under flow due to stretching during the tapering process [119]. Propagation in the 10 cm long microwire section of the microtaper amounts to 5.2 dB from the total transmission loss, and the remaining 2.8 dB includes the losses from mode mismatch and reflection at the coupling interfaces (0.66 dB/facet), imperfections in the ECHF facets, and propagation in the 3.5 cm long transition regions of the microtaper [33].

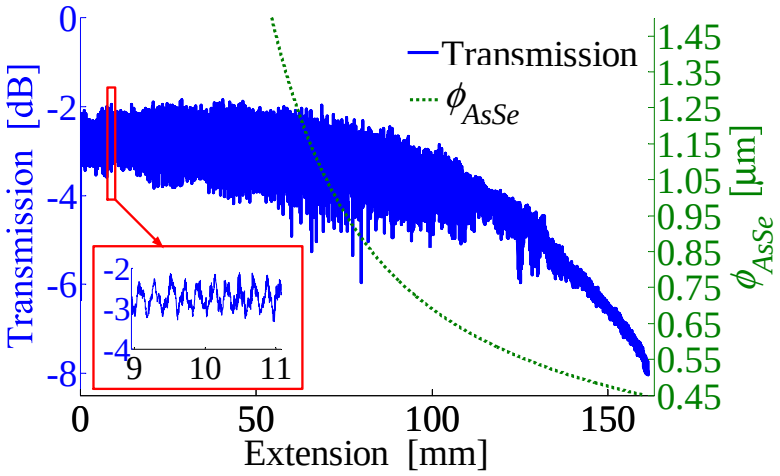

Fig. 6.8 Measured microtaper transmission as a function of extension.

6.4 Birefringence Characterization

The group birefringence is measured using the method of crossed-polarizers [120–122]. Figure 6.9 presents a schematic of the setup used to measure the group birefringence in tapered ECHFs. Amplified spontaneous emission is passed through a linear polarizer and launched into the microtaper at 45^o from the principal axes so that half the signal power propagates along the slow axis, and the other half propagates along the fast axis. The output of the birefringent fiber is passed through another linear polarizer at 45^o from the principal axes of the microtaper.

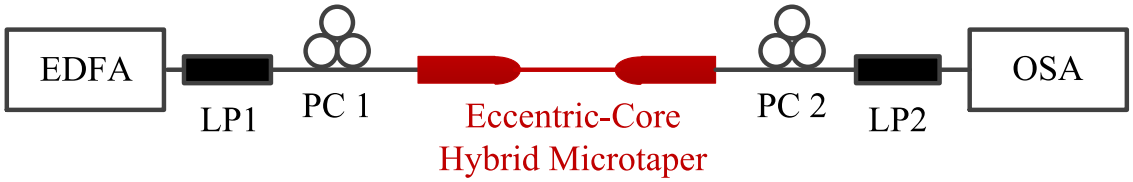

Fig. 6.9 Schematic of the crossed-polarizers setup for the measurement of group birefringence. EDFA: Erbium-doped fiber amplifier, LP: linear polarizer, PC: Polarization Controller, OSA: Optical spectrum analyzer.

After the second linear polarizer, the total electric field is given by

$$E = a_x e^{j\beta_x(\lambda)L_w} + a_y e^{j\beta_y(\lambda)L_w}$$

and the intensity is given by

$$I = |a_x|^2 + |a_y|^2 + 2\,|a_x|\,|a_y| \cos\left[\Delta\beta L_w + \theta_x - \theta_y\right],$$

where a_m and β_m are the complex amplitude and the propagation constant with m being x or y, θ_m is the phase of a_m, L_w is the length of the microwire, and $\Delta\beta = \beta_x - \beta_y$. A spectral interference pattern with a modulation proportional to $\cos\left[\Delta\beta L_w + \theta_x - \theta_y\right]$ arises from the wavelength dependence of $\Delta\beta$ [120]. By differentiating the phase-difference $\Delta\phi = \Delta\beta L_w$ with respect to wavelength and using $n_g = (-\lambda^2/2\pi)\, d\beta/d\lambda$, the group birefringence is given by

$$b_g = \Delta n_g = \left(-\lambda^2/2\pi\right) d\Delta\beta/d\lambda = \left(-\lambda^2/2\pi L_w\right) d\Delta\phi/d\lambda.$$

Between two consecutive minima of the interference pattern, at λ_1 and λ_2, $\Delta\phi$ varies by

2π and $|d\Delta\phi/d\lambda| \approx 2\pi/\Delta\lambda$ where $\Delta\lambda = |\lambda_1 - \lambda_2|$, leading to

$$|b_g| = |\Delta n_g| = \lambda^2/\Delta\lambda L_w$$

Figure 6.10 presents the measured transmission of the second linear polarizer at the end of the tapering process. Using the measured spectral modulation period of $\Delta\lambda = 0.8$ nm at $\lambda = 1550$ nm, and $L_w = 10$ cm, the group birefringence of the ECHM is $|b_g| = 0.018$.

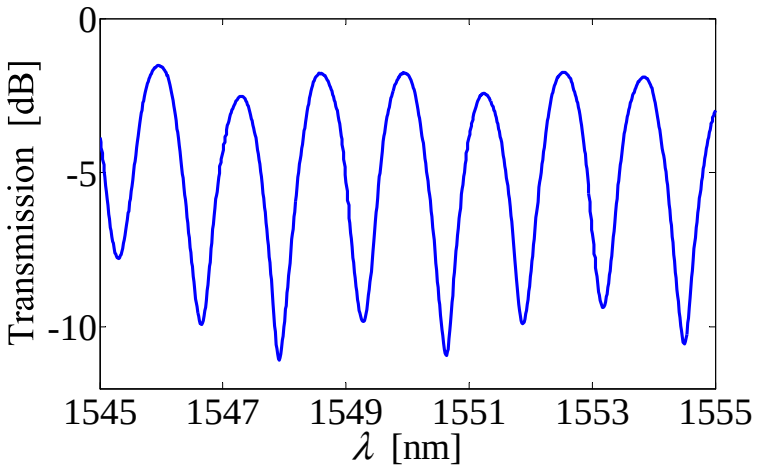

Fig. 6.10 Interference pattern obtained at the OSA in Fig 6.9.

The interference spectrum at the OSA was taken during the tapering process for the determination of b_g as a function of ϕ_{AsSe} for the ECHF in Fig. 6.7(b). Figure 6.11 presents the measured b_g as a function of ϕ_{AsSe} showing an increase in the birefringence as the core diameter decreases. The tangential vector finite-element method [80, 81] is used to numerically calculate b_g as a function of ϕ_{AsSe} with $s = \rho\phi_{AsSe}$, where $\rho = 0.69$ is the ratio of the edge separation to the As_2Se_3 core diameter for the ECHF in Fig. 6.7(b) and is constant during the tapering process. The numerically calculated values of b_g provided in Fig. 6.11 show close agreement with experimental results.

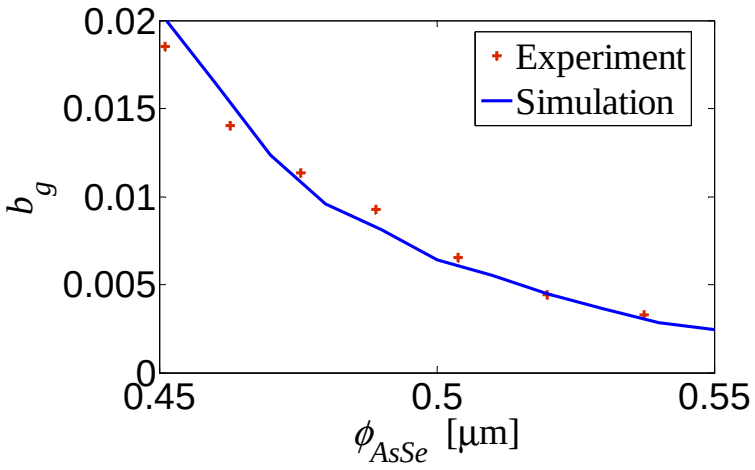

Fig. 6.11 Experimental value of b_g as a function of core diameter measured during the tapering process.

Wavelength values λ_i corresponding to the minima of the measured interference pattern are recorded from Fig. 6.10. The phase difference $\Delta\phi(\lambda)$ increases or decreases by 2π between λ_i and λ_{i+1} for all λ_i leading to

$$\Delta\phi_{i+1} = \Delta\phi_i \pm 2\pi = \Delta\phi_{i=1} \pm 2\pi i,$$

where $\Delta\phi_i = \Delta\phi(\lambda_i)$. Setting $\Delta\phi_{i=1} = 0$, the values of $\Delta\phi_i$ and λ_i are fitted to a third degree polynomial to obtain a function $\Delta\phi(\lambda)$. Figure 6.12 presents the wavelength dependence of the group birefringence calculated from $\Delta\phi(\lambda)$ using $|b_g| = (\lambda^2/2\pi L)\,|d\Delta\phi/d\lambda|$. The value of $|b_g|$ varies with wavelength at a rate of 7.8×10^{-5} nm^{-1} at $\lambda = 1550$ nm indicting strong group birefringence dispersion.

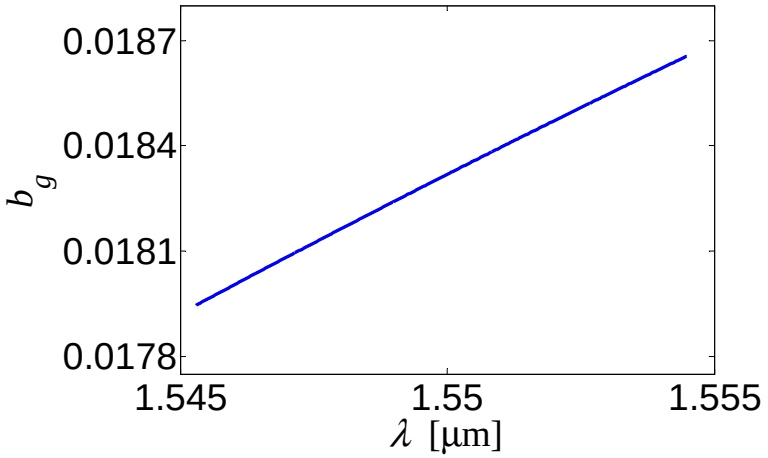

Fig. 6.12 Measured b_g as a function of λ using the interference pattern in Fig. 6.10.

6.5 Nonlinearity Characterization

Figure 6.13 presents a schematic of the setup used to measure γ [103]. Two continuous wave (CW) lasers with equal powers at wavelengths $\lambda_1 = 1549.75$ nm and $\lambda_2 = 1550.03$ nm are combined using a 3 dB coupler to obtain a sinusoidal signal with a duration of 29 ps. The polarization controllers PC1 and PC2 are used to align the polarization of the two CW lasers with the transmission axis of a linear polarizer to guarantee full interference between the lasers and form a sinusoidal signal. To avoid damaging the microwire by thermal heating through material absorption, the average power is reduced by 20 dB through modulation of the sinusoidal signal using a Mach-Zehnder modulator and a square pulse with a duration of 10 ns at a repetition rate of 1 MHz. The polarization of the sinusoidal signal is aligned with the principal axis of the Mach-Zehnder modulator using PC3 to achieve the maximum modulation extinction ratio. The modulated signal is then passed through an Erbium-doped fiber amplifier followed by a variable attenuator before being launched into the microtaper. The polarization of the modulated sinusoidal signal is aligned with one of the principal axes of microtaper using PC4. The output of the microtaper is observed using an optical spectrum analyzer.

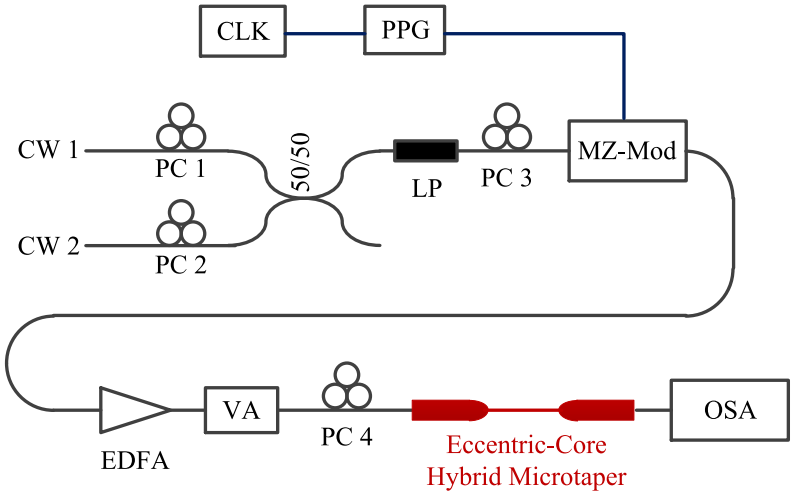

Fig. 6.13 Schematic of the waveguide nonlinearity measurement setup. CW: continuous wave laser, PC: polarization controller, LP: linear polarizer, CLK: electrical clock, PPG: pulse pattern generator, MZ-Mod: Mach-Zehnder modulator, EDFA: Erbium-doped fiber amplifier, VA: variable attenuator, OSA: Optical spectrum analyzer.

Figure 6.14(a) shows the spectral evolution of the sinusoidal signal at the output of the microtaper at increasing peak power levels. Figure 6.14(b) presents the value of ϕ_{SPM} for each peak power level calculated from I_0 and I_1, which are illustrated in Fig. 6.14(a), using the equation [103]

$$\frac{I_0}{I_1} = \frac{J_0^2(\phi_{SPM}/2) + J_1^2(\phi_{SPM}/2)}{J_1^2(\phi_{SPM}/2) + J_2^2(\phi_{SPM}/2)}$$

where J_0, J_1 and J_2 are the zero, first, and second order Bessel functions of the first kind. Using the experimentally estimated loss of 5.2 dB over the wire section length of 10 cm, the effective length is $L_{eff} = 5.83$ cm. The ratio of nonlinear phase-shift accumulating in the wire section $\phi_{SPM}^{w} = \gamma P_0 L_{eff}$ to the phase-shift in the entire microtaper $\phi_{SPM} = \int \gamma(z)\, P(z)\, dz$ is $\rho = \phi_{SPM}^{w}/\phi_{SPM} = 0.87$. The product $\gamma L_{eff}/\rho = 12.04$ W^{-1} is the slope of the linear fit connecting the experimentally measured values of ϕ_{SPM} in Fig. 6.14(b). The waveguide nonlinearity in the wire section of the microtaper is $\gamma = 12.04 \times \rho/L_{eff} = 180$ W^{-1}m^{-1}, in close agreement with the value measured in concentric-core microwires [33].

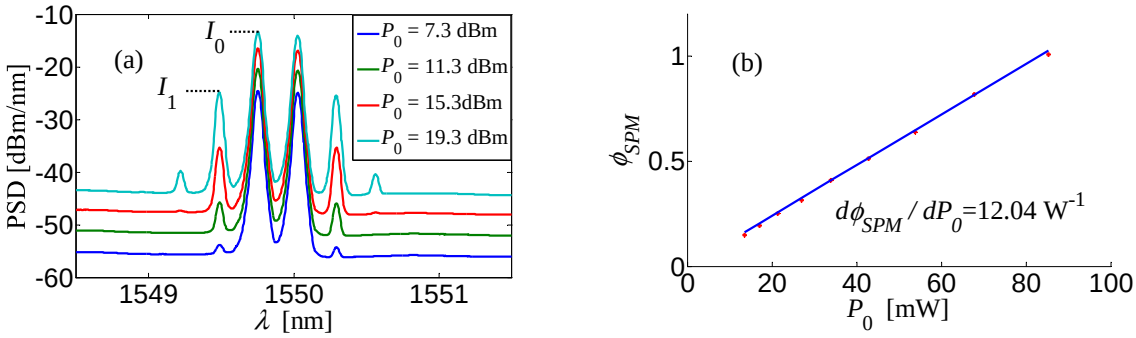

Fig. 6.14 Sinusoidal-signal self-phase modulation measurements showing a) the recorded output spectra of the hybrid microtaper for increasing power levels, and b) the measured ϕ_{SPM} as a function of the peak power of the sinusoidal-signal.

6.6 Conclusion

An eccentric-core As_2Se_3-PMMA fiber has been tapered to achieve a high group birefringence of $b_g = 0.018$ and a high waveguide nonlinearity of $\gamma = 180$ W^{-1}m^{-1}. The tangential vector finite-element method is used to numerically calculate the phase birefringence and the group birefringence. Group birefringence characterization of eccentric-core hybrid microtapers shows close agreement between experimental results and numerical calculations. Such eccentric-core hybrid microtapers with engineerable birefringence and high nonlinearity can be used for a variety of applications involving an extensive use of polarization and nonlinearity.

Chapter 7

Conclusion

In this thesis, I have presented a study of hybrid microwires that are composed of an As_2Se_3 core and a PMMA cladding. First, I have presented a theoretical and experimental study of the generalized heat-brush approach for the fabrication of microtapers. This tapering approach is used for the fabrication the microwires presented in this thesis. Second, I have presented the results of the fabrication and characterization of hybrid microwires that are fabricated by tapering a single-mode step-index As_2Se_3 fiber that is coated with a PMMA layer. Supercontinuum generation has been demonstrated in one microwire with $\gamma = 133\ \mathrm{W^{-1}m^{-1}}$. Third, I have presented the results of the fabrication and characterization of hybrid microwires that are fabricated by tapering multimode hybrid fibers that are composed of an As_2Se_3 and a PMMA cladding. The hybrid fiber has been tapered to achieve single-mode transmission and a waveguide nonlinearity as high as $\gamma = 176\ \mathrm{W^{-1}m^{-1}}$ close to the maximum theoretical value of $\gamma = 187\ \mathrm{W^{-1}m^{-1}}$. Fabrication of such hybrid microwires from a multi-mode As_2Se_3-PMMA fiber is greatly simplified as it eliminates the need for single-mode step-index As_2Se_3 fibers. A Kerr-shutter has been implemented using the fabricated hybrid microwire to demonstrate switching by induced polarization rotation with a 100% switching power of 266 mW. Finally, I have presented a theoretical study of and an experimental demonstration of eccentric-core hybrid microwire with a high group birefringence of $b_g = 0.018$ and a high waveguide nonlinearity of $\gamma = 180\ \mathrm{W^{-1}m^{-1}}$. Such eccentric-core hybrid microtapers with engineerable birefringence and high nonlinearity can be used for a variety of applications involving an extensive use of polarization and nonlinearity.

There are several practical fundamental research problems open for further investigation in the future. First, in addition to concentric-core and eccentric core microwires, the hybrid As_2Se_3-PMMA technology platform can be used for the fabrication of advanced cross-sectional geometries such as dual-core and photonics crystal fibers. Just as the As_2Se_3 microwire is made into a hybrid microwire by replacing the air cladding with a polymer cladding, air holes in As_2Se_3 photonic crystal and suspended core fibers can be filled with PMMA to obtain advanced hybrid structures. Therefore, all advantages provided by suspended core and photonic crystal fibers in terms of chromatic dispersion and birefringence engineering can be achieved using the hybrid technology. Furthermore, the fabrication of photonic-crystal fiber geometries where the air is replaced with a polymer is easier; especially in the case of photonic crystal fibers because filling the holes with PMMA eliminates the problem of hole collapse.

Second, microwires with advanced longitudinal geometries can be fabricated for a variety of advanced applications. Indeed, a project has been started with the objective of achieving enhanced self-frequency shift in hybrid microwires that have nonuniform cross-section. The theoretical study for this application has already been performed [38] and there are plans to achieve experimental demonstration.

Third, highly birefringent eccentric-core microwires can be used for the variety of nonlinear applications such as polarization entangled photon generation [47, 48]. They can also be used for sensing applications when the As_2Se_3 core is placed at the edge of the PMMA cladding layer making the microwire sensitive to the surrounding environment. The supporting polymer layer makes the overall structure robust enough for placement in a fluid to measure refractive-index changes.

Forth, there must be further investigation to determine the origin of the increased loss in microwires. For example, it should verified that the crystallization of PMMA is actually the cause of the loss in the microwire. By placing the hybrid microwire in an organic solvent, the PMMA layer will dissolve. Comparison between the transmission loss before and after the PMMA layer is removed will show whether crystallization is the cause of the loss. Another fundamental problem of interest is the investigation of methods for the elimination of the crystallization in PMMA and other polymers. This can be investigated in the context of mixing different polymers together, and by controlling the length of the polymer chains.

Fifth, the polymer can be doped with a variety of materials for advanced application.

For example, the polymer can be doped with carbon nanotubes allowing saturable absorption in hybrid microwires. The polymer can also be doped with rare-earth elements such as Erbium for the amplification of optical signals in the telecommunication band. Finally, the polymer can be doped with polymer dyes for dispersion engineering and sensing applications.

Bibliography

[1] J. H. V. Price, T. M. Monro, H. Ebendorff-Heidepriem, F. Poletti, P. Horak, V. Finazzi, J. Y. Y. Leong, P. Petropoulos, J. C. Flanagan, G. Brambilla, X. Feng, and D. J. Richardson, "Mid-IR supercontinuum generation from nonsilica microstructured optical fibers," *J. Sel. Topics in Quant. Electron.*, vol. 13, no. 3, pp. 738 –749, 2007.

[2] F. Gonthier, J. Lapierre, C. Veilleux, S. Lacroix, and J. Bures, "Investigation of power oscillations along tapered monomode fibers," *Appl. Opt.*, vol. 26, no. 3, pp. 444–449, 1987.

[3] P. A. Franken, A. E. Hill, C. W. Peters, and G. Weinreich, "Generation of optical harmonics," *Phys. Rev. Lett.*, vol. 7, pp. 118–119, 1961.

[4] B. Saleh and M. C. Teich, *Fundamentals of photonics*, 2nd ed. Wiley, 1991.

[5] L. Yin, J. Zhang, P. M. Fauchet, and G. P. Agrawal, "Optical switching using nonlinear polarization rotation inside silicon waveguides," *Opt. Lett.*, vol. 34, no. 4, pp. 476–478, 2009.

[6] B. E. Olsson, P. Ohlen, L. Rau, and D. J. Blumenthal, "A simple and robust 40-gb/s wavelength converter using fiber cross-phase modulation and optical filtering," *Photon. Technol. Lett.*, vol. 12, no. 7, pp. 846 –848, 2000.

[7] J. K. Ranka, R. S. Windeler, and A. J. Stentz, "Visible continuum generation in air-silica microstructure optical fibers with anomalous dispersion at 800 nm," *Opt. Lett.*, vol. 25, no. 1, pp. 25–27, 2000.

[8] P. V. Mamyshev, "All-optical data regeneration based on self-phase modulation effect," in *Optical Communication, 1998. 24th European Conference on*, vol. 1, 1998, pp. 475 – 476 vol.1.

[9] G. P. Agrawal, *Nonlinear fiber optics*, 4th ed. Academic Press, 2007.

[10] R. E. Slusher, G. Lenz, J. Hodelin, J. Sanghera, L. B. Shaw, and I. D. Aggarwal, "Large raman gain and nonlinear phase shifts in high-purity As_2Se_3 chalcogenide fibers," *J. Opt. Soc. Am. B*, vol. 21, no. 6, pp. 1146–1155, 2004.

[11] T. Schreiber, J. Limpert, H. Zellmer, A. TÃŒnnermann, and K. Hansen, "High average power supercontinuum generation in photonic crystal fibers," *Opt. Commun.*, vol. 228, no. 1-3, pp. 71 – 78, 2003.

[12] G. Boudebs, W. Berlatier, S. Cherukulappurath, F. Smektala, M. Guignard, and J. Troles, "Nonlinear optical properties of chalcogenide glasses at telecommunication wavelength using nonlinear imaging technique," in *Transparent Optical Networks, 2004. Proceedings of 2004 6th International Conference on*, vol. 2, July 2004, pp. 145–150.

[13] G. Boudebs, S. Cherukulappurath, M. Guignard, J. Troles, F. Smektala, and F. Sanchez, "Linear optical characterization of chalcogenide glasses," *Optics Communications*, vol. 230, no. 4-6, pp. 331 – 336, 2004.

[14] K. S. Abedin, "Linear and nonlinear optical properties of single-mode as_2se_3 chalcogenide fiber," in *Optical Fiber Communication Conference, 2006 and the 2006 National Fiber Optic Engineers Conference. OFC 2006*, March 2006, pp. 3 pp.–.

[15] P. Dumais, F. Gonthier, S. Lacroix, J. Bures, A. Villeneuve, P. G. J. Wigley, and G. I. Stegeman, "Enhanced self-phase modulation in tapered fibers," *Opt. Lett.*, vol. 18, no. 23, pp. 1996–1998, 1993.

[16] K. Hansen, "Dispersion flattened hybrid-core nonlinear photonic crystal fiber," *Opt. Express*, vol. 11, no. 13, pp. 1503–1509, 2003.

[17] K. Kiang, K. Frampton, T. Monro, R. Moore, J. Tucknott, D. Hewak, D. Richardson, and H. Rutt, "Extruded singlemode non-silica glass holey optical fibres," *Electron. Lett.*, vol. 38, no. 12, pp. 546–547, 2002.

[18] E. C. Mägi, L. B. Fu, H. C. Nguyen, M. R. Lamont, D. I. Yeom, and B. J. Eggleton, "Enhanced kerr nonlinearity in sub-wavelength diameter As_2Se_3 chalcogenide fiber tapers," *Opt. Express*, vol. 15, no. 16, pp. 10 324–10 329, 2007.

[19] C. Baker and M. Rochette, "Highly nonlinear hybrid AsSe-PMMA microtapers," *Opt. Express*, vol. 18, no. 12, pp. 12 391–12 398, 2010.

[20] L. Brilland, F. Smektala, G. Renversez, T. Chartier, J. Troles, T. Nguyen, N. Traynor, and A. Monteville, "Fabrication of complex structures of holey fibers in chalcogenide glass," *Opt. Express*, vol. 14, no. 3, pp. 1280–1285, 2006.

[21] M. El-Amraoui, J. Fatome, J. C. Jules, B. Kibler, G. Gadret, C. Fortier, F. Smektala, I. Skripatchev, C. Polacchini, Y. Messaddeq, J. Troles, L. Brilland, M. Szpulak, and G. Renversez, "Strong infrared spectral broadening in low-loss as-s chalcogenide suspended core microstructured optical fibers," *Opt. Express*, vol. 18, no. 5, pp. 4547–4556, 2010.

[22] F. Bilodeau, K. Hill, S. Faucher, and D. Johnson, "Low-loss highly overcoupled fused couplers: Fabrication and sensitivity to external pressure," in *Optical Fiber Sensors*. Optical Society of America, 1988, p. ThCC10.

[23] R. P. Kenny, T. A. Birks, and K. P. Oakley, "Control of optical fibre taper shape," *Electron. Lett.*, vol. 27, no. 18, pp. 1654–1656, Aug. 1991.

[24] T. A. Birks and Y. W. Li, "The shape of fiber tapers," *J. Lightwave Technol.*, vol. 10, no. 4, pp. 432–438, Apr 1992.

[25] C. Baker and M. Rochette, "A generalized heat-brush approach for precise control of the waist profile in fiber tapers," *Opt. Mater. Express*, vol. 1, no. 6, pp. 1065–1076, 2011.

[26] S. D. Hart, G. R. Maskaly, B. Temelkuran, P. H. Prideaux, J. D. Joannopoulos, and Y. Fink, "External reflection from omnidirectional dielectric mirror fibers," *Science*, vol. 296, no. 5567, pp. 510–513, 2002.

[27] B. Temelkuran, S. D. Hart, G. Benoit, and J. D. J. Y. Fink, "Wavelength-scalable hollow optical fibres with large photonic bandgaps for co_2 laser transmission," *Nature*, vol. 420, no. 6916, pp. 650–653, 2002.

[28] T. Engeness, M. Ibanescu, S. Johnson, O. Weisberg, M. Skorobogatiy, S. Jacobs, and Y. Fink, "Dispersion tailoring and compensation by modal interactions in omniguide fibers," *Opt. Express*, vol. 11, no. 10, pp. 1175–1196, 2003.

[29] M. Liao, C. Chaudhari, G. Qin, X. Yan, C. Kito, T. Suzuki, Y. Ohishi, M. Matsumoto, and T. Misumi, "Fabrication and characterization of a chalcogenide-tellurite composite microstructure fiber with high nonlinearity," *Opt. Express*, vol. 17, no. 24, pp. 21 608–21 614, 2009.

[30] N. Granzow, S. P. Stark, M. A. Schmidt, A. S. Tverjanovich, L. Wondraczek, and P. S. Russell, "Supercontinuum generation in chalcogenide-silica step-index fibers," *Opt. Express*, vol. 19, no. 21, pp. 21 003–21 010, 2011.

[31] J. D. Love and W. M. Henry, "Quantifying loss minimisation in single-mode fibre tapers," *Electronics Letters*, vol. 22, no. 17, pp. 912–914, 1986.

[32] J. D. Love, W. M. Henry, W. J. Stewart, R. J. Black, S. Lacroix, and F. Gonthier, "Tapered single-mode fibres and devices. *I*. adiabaticity criteria," *Optoelectron., IEE Proc. J*, vol. 138, no. 5, pp. 343–354, 1991.

[33] C. Baker and M. Rochette, "High nonlinearity and single-mode transmission in tapered multi-mode As_2Se_3-PMMA fibers," *J. IEEE Photonics*, vol. 4, no. 3, pp. 960 –969, 2012.

[34] F. Bilodeau, K. O. Hill, D. C. Johnson, and S. Faucher, "Compact, low-loss, fused biconical taper couplers: overcoupled operation and antisymmetric supermode cutoff," *Opt. Lett.*, vol. 12, no. 8, pp. 634–636, 1987.

[35] S. Moon and D. Y. Kim, "Effective single-mode transmission at wavelengths shorter than the cutoff wavelength of an optical fiber," *Photon. Technol. Lett.*, vol. 17, no. 12, pp. 2604 – 2606, 2005.

[36] D. Donlagic, "In-line higher order mode filters based on long highly uniform fiber tapers," *J. Lightwave Technol.*, vol. 24, no. 9, pp. 3532 –3539, 2006.

[37] Y. Jung, G. Brambilla, and D. J. Richardson, "Broadband single-mode operation of standard optical fibers by using a sub-wavelength optical wire filter," *Opt. Express*, vol. 16, no. 19, pp. 14 661–14 667, 2008.

[38] A. Alkadery and M. Rochette, "Widely tunable soliton shifting for mid-infrared applications," in *IEEE Photonics Conference 2011 (IPC2011)*, 2011.

[39] R. Ahmad and M. Rochette, "High efficiency and ultra broadband optical parametric four-wave mixing in chalcogenide-pmma hybrid microwires," *Opt. Express*, vol. 20, no. 9, pp. 9572–9580, 2012.

[40] A. Kudlinski, A. K. George, J. C. Knight, J. C. Travers, A. B. Rulkov, S. V. Popov, and J. R. Taylor, "Zero-dispersion wavelength decreasing photonic crystal fibers for ultraviolet-extended supercontinuum generation," *Opt. Express*, vol. 14, no. 12, pp. 5715–5722, 2006.

[41] G. Qin, X. Yan, C. Kito, M. Liao, T. Suzuki, A. Mori, and Y. Ohishi, "Zero-dispersion-wavelength-decreasing tellurite microstructured fiber for wide and flattened supercontinuum generation," *Opt. Lett.*, vol. 35, no. 2, pp. 136–138, 2010.

[42] A. C. Judge, O. Bang, B. J. Eggleton, B. T. Kuhlmey, E. C. Mägi, R. Pant, and C. M. de Sterke, "Optimization of the soliton self-frequency shift in a tapered photonic crystal fiber," *J. Opt. Soc. Am. B*, vol. 26, no. 11, pp. 2064–2071, Nov 2009.

[43] C. Baker and M. Rochette, "Birefringence engineering and high nonlinearity in eccentric-core As_2Se_3-pmma microtapers," *J. Lightwave Technol.*, 2012.

[44] A. Alphones and G. Sanyal, "Polarization characteristics of eccentric core single-mode fibers," *J. Lightwave Technol.*, vol. 5, no. 4, pp. 598 – 601, 1987.

[45] N. Kishi and E. Yamashita, "Realization of broad-band phase devices by using w-type eccentric-core optical fibers," *J. Lightwave Technol.*, vol. 8, no. 8, pp. 1207 – 1211, 1990.

[46] C. Guan, L. Yuan, F. Tian, and Q. Dai, "Characteristics of near-surface-core optical fibers," *J. Lightwave Technol.*, vol. 29, no. 19, pp. 3004–3008, 2011.

[47] R. H. Stolen, M. A. Bösch, and C. Lin, "Phase matching in birefringent fibers," *Opt. Lett.*, vol. 6, no. 5, pp. 213–215, 1981.

[48] X. .Li, P. L. Voss, J. E. Sharping, and P. Kumar, "Optical-fiber source of polarization-entangled photons in the 1550 nm telecom band," *Phys. Rev. Lett.*, vol. 94, p. 053601, 2005.

[49] J. E. Rothenberg, "Modulational instability for normal dispersion," *Phys. Rev. A*, vol. 42, pp. 682–685, 1990.

[50] S. Wabnitz, "Modulational polarization instability of light in a nonlinear birefringent dispersive medium," *Phys. Rev. A*, vol. 38, pp. 2018–2021, 1988.

[51] R. Ahmad, M. Rochette, and C. Baker, "Fabrication of bragg gratings in subwavelength diameter as2se3 chalcogenide wires," *Opt. Lett.*, vol. 36, no. 15, pp. 2886–2888, 2011.

[52] W. Liang, Y. Huang, Y. X., R. K. Lee, and A. Yariv, "Highly sensitive fiber bragg grating refractive index sensors," *App. Phys. Lett.*, vol. 86, no. 15, p. 151122, 2005.

[53] A. D. Kersey, M. A. Davis, H. J. Patrick, M. LeBlanc, K. P. Koo, C. G. Askins, M. A. Putnam, and E. J. Friebele, "Fiber grating sensors," *J. Lightwave Technol.*, vol. 15, no. 8, pp. 1442 –1463, 1997.

[54] I. V. Kabakova, D. Grobnic, S. Mihailov, E. C. Mägi, C. M. de Sterke, and B. J. Eggleton, "Bragg grating-based optical switching in a bismuth-oxide fiber with strong $\chi(3)$-nonlinearity," *Opt. Express*, vol. 19, no. 7, pp. 5868–5873, 2011.

[55] J. T. Mok, C. M. de Sterke, I. C. M. Littler, and B. J. Eggleton, "Dispersionless slow light using gap solitons," *Nat. Phys.*, vol. 2, no. 11, pp. 775 – 780, 2006.

[56] T. Bricheno and V. Baker, "All-fibre polarisation splitter/combiner," *Electron. Lett.*, vol. 21, no. 6, pp. 251–252, 1985.

[57] A. C. Boucouvalas and G. Georgiou, "Biconical taper coaxial optical fibre coupler," *Electron. Lett.*, vol. 21, no. 19, pp. 864–865, July 1985.

[58] M. S. Yataki, D. N. Payne, and M. P. Varnham, "All-fibre wavelength filters using concatenated fused-taper couplers," *Electronics Letters*, vol. 21, no. 6, pp. 248–249, 1985.

[59] J. V. Wright, "Wavelength dependence of fused couplers," *Electronics Letters*, vol. 22, no. 6, pp. 320–321, 1986.

[60] C. M. Lawson, P. M. Kopera, T. Y. Hsu, and V. J. Tekippe, "In-line single-mode wavelength division multiplexer/demultiplexer," *Electronics Letters*, vol. 20, no. 23, pp. 963–964, 1984.

[61] R. G. Lamont, D. C. Johnson, and K. O. Hill, "Power transfer in fused biconical-taper single-mode fiber couplers: dependence on external refractive index," *Appl. Opt.*, vol. 24, no. 3, pp. 327–332, 1985.

[62] S. Jensen, "The nonlinear coherent coupler," *J. Quantum Electron.*, vol. 18, no. 10, pp. 1580–1583, Oct 1982.

[63] A. W. SNYDER, "Coupled-mode theory for optical fibers," *J. Opt. Soc. Am.*, vol. 62, no. 11, pp. 1267–1277, 1972.

[64] N. G. R. Broderick, T. M. Monro, P. J. Bennett, and D. J. Richardson, "Nonlinearity in holey optical fibers: measurement and future opportunities," *Opt. Lett.*, vol. 24, no. 20, pp. 1395–1397, 1999.

[65] J. Broeng, D. Mogilevstev, S. E. Barkou, and A. Bjarklev, "Photonic crystal fibers: A new class of optical waveguides," *Opt. Fiber Tech.*, vol. 5, no. 3, pp. 305 – 330, 1999.

[66] J. C. Knight, T. A. Birks, P. S. J. Russell, and D. M. Atkin, "All-silica single-mode optical fiber with photonic crystal cladding," *Opt. Lett.*, vol. 21, no. 19, pp. 1547–1549, 1996.

[67] R. F. Cregan, B. J. Mangan, J. C. Knight, T. A. Birks, P. S. J. Russell, P. J. Roberts, and D. C. Allan, "Single-mode photonic band gap guidance of light in air," vol. 285, no. 5433, pp. 1537–1539, 1999.

[68] D. Mogilevtsev, T. A. Birks, and P. S. J. Russell, "Group-velocity dispersion in photonic crystal fibers," *Opt. Lett.*, vol. 23, no. 21, pp. 1662–1664, 1998.

[69] V. Finazzi, T. M. Monro, and D. J. Richardson, "Small-core silica holey fibers: nonlinearity and confinement loss trade-offs," *J. Opt. Soc. Am. B*, vol. 20, no. 7, pp. 1427–1436, 2003.

[70] A. W. Snyder and J. D. Love, *Optical waveguide theory.* Chapman and Hall, 1983.

[71] J. Gowar, *Optical Communication Systems*, 2nd ed. Prentice Hall, 1993.

[72] V. P. Tzolov, M. Fontaine, N. Godbout, and S. Lacroix, "Nonlinear modal parameters of optical fibers: a full-vectorial approach," *J. Opt. Soc. Am. B*, vol. 12, no. 10, pp. 1933–1941, 1995.

[73] V. Tzolov, M. Fontaine, N. Godbout, and S. Lacroix, "Nonlinear self-phase-modulation effects: a vectorial first-order perturbation approach," *Opt. Lett.*, vol. 20, no. 5, pp. 456–458, 1995.

[74] M. Foster, K. Moll, and A. Gaeta, "Optimal waveguide dimensions for nonlinear interactions," *Opt. Express*, vol. 12, no. 13, pp. 2880–2887, 2004.

[75] S. Afshar and T. M. Monro, "A full vectorial model for pulse propagation in emerging waveguides with subwavelength structures part i: Kerr nonlinearity," *Opt. Express*, vol. 17, no. 4, pp. 2298–2318, 2009.

[76] S. Afshar, W. Q. Zhang, H. Ebendorff-Heidepriem, and T. M. Monro, "Small core optical waveguides are more nonlinear than expected: experimental confirmation," *Opt. Lett.*, vol. 34, no. 22, pp. 3577–3579, 2009.

[77] A. Yariv, *Optical Electronics in Modern Communications*, 5th ed. Oxford University Press, 1997.

[78] F. Gonthier, S. Lacroix, and J. Bures, "Numerical calculations of modes of optical waveguides with two-dimensional refractive index profiles by a field correction method," *Opt. and Quantum Electron.*, vol. 26, pp. S135–S149, 1994.

[79] N. Kishi and T. Okoshi, "Proposal for a boundary-integral method without using green's function," *Microwave Theory and Techniques, IEEE Transactions on*, vol. 35, no. 10, pp. 887 – 892, oct. 1987.

[80] T. Angkaew, M. Matsuhara, and N. Kumagai, "Finite-element analysis of waveguide modes: A novel approach that eliminates spurious modes," *Microwave Theory and Techniques, IEEE Transactions on*, vol. 35, no. 2, pp. 117 – 123, 1987.

[81] J. F. Lee, D. K. Sun, and Z. J. Cendes, "Full-wave analysis of dielectric waveguides using tangential vector finite elements," *Microwave Theory and Techniques, IEEE Transactions on*, vol. 39, no. 8, pp. 1262 –1271, 1991.

[82] J. M. Jin, *The Finite Element Method in Electromagnetics*, 2nd ed. Wiley-IEEE Press, 2002.

[83] D. Engwirda. (2009) Mesh2d - automatic mesh generation. [Online]. Available: http://www.mathworks.com/matlabcentral/fileexchange/25555-mesh2d-automatic-mesh-generation

[84] R. H. Hardin and F. D. Tappert, "Applications of the split-step fourier method to the numerical solution of nonlinear and variable coefficient wave equations," *SIAM Rev*, vol. 15, no. 13, p. 423, 1973.

[85] R. A. Fisher and W. Bischel, "The role of linear dispersion in plane-wave self-phase modulation," *Applied Physics Letters*, vol. 23, no. 12, pp. 661–663, 1973.

[86] F. Geyling, "Basic fluid dynamic consideration in the drawing of optical fibers," *Bell Sys. Tech. J.*, vol. 55, pp. 1011–1056, 1976.

[87] J. Dewynne, J. R. Ockendon, and P. Wilmott, "On a mathematical model for fiber tapering," *SIAM J. on App. Math.*, vol. 49, no. 4, pp. 983–990, 1989.

[88] N. Vukovic, N. Broderick, M. Petrovich, and G. Brambilla, "Novel method for the fabrication of long optical fiber tapers," *Photon. Technol. Lett.*, vol. 20, no. 14, pp. 1264 –1266, 2008.

[89] S. Chapra and R. Canale, *Numerical Methods for Engineers*, 5th ed. McGraw-Hill, 2005.

[90] T. H. Cormen, C. E. Leiserson, R. L. Rivest, and C. Stein, *Introduction to Algorithms*, 2nd ed. MIT Press, 2001.

[91] *AMTIR-2: Arsenic Selenide Glass As-Se*, Amorphous Materials Inc., 2009. [Online]. Available: http://www.amorphousmaterials.com/amtir2.htm

[92] S. N. Kasarova, N. G. Sultanova, C. D. Ivanov, and I. D. Nikolov, "Analysis of the dispersion of optical plastic materials," *Opt. Materials*, vol. 29, no. 11, pp. 1481 – 1490, 2007.

[93] F. D'Amore, M. Lanata, S. M. Pietralunga, M. C. Gallazzi, and G. Zerbi, "Enhancement of PMMA nonlinear optical properties by means of a quinoid molecule," *Optical Materials*, vol. 24, no. 4, pp. 661 – 665, 2004.

[94] M. G. Kuzyk, *Polymer Fiber Optics: Materials, Physics, and Applications*, 1st ed. CRC Press, 2006.

[95] W. Stewart and J. Love, "Design limitation on tapers and couplers in single mode fibers," *in technical digest, Fifth International Conference on Integrated Optics and Optical Fiber Communication-Eleventh European Conference on Optical Communication*, p. 559, 1985.

[96] S. Lacroix, R. Bourbonnais, F. Gonthier, and J. Bures, "Tapered monomode optical fibers: understanding large power transfer," *Appl. Opt.*, vol. 25, no. 23, pp. 4421–4425, 1986.

[97] S. Lacroix, R. J. Black, C. Veilleux, and J. Lapierre, "Tapered single-mode fibers: external refractive-index dependence," *Appl. Opt.*, vol. 25, no. 15, pp. 2468–2469, 1986.

[98] W. Burns, M. Abebe, C. Villarruel, and R. Moeller, "Loss mechanisms in single-mode fiber tapers," *J. Lightwave Technol.*, vol. 4, no. 6, pp. 608–613, 1986.

[99] R. J. Black, S. Lacroix, F. Gonthier, and J. D. Love, "Tapered single-mode fibres and devices. II. experimental and theoretical quantification," *Optoelectronics, IEE Proceedings J*, vol. 138, no. 5, pp. 355–364, 1991.

[100] C. Lee, M. Wu, L. Sheu, P. Fan, and J. Hsu, "Design and analysis of completely adiabatic tapered waveguides by conformal mapping," *J. Lightwave Technol.*, vol. 15, no. 2, pp. 403–410, 1997.

[101] M. A. Duguay and J. W. Hansen, "An ultrafast light gate," in *Electron Devices Meeting, 1969 International*, vol. 15, 1969, pp. 68 – 70.

[102] C. Pollock and M. Lipson, *Integrated photonics*. Springer, 2003.

[103] A. Boskovic, S. V. Chernikov, J. R. Taylor, L. Gruner-Nielsen, and O. A. Levring, "Direct continuous-wave measurement of n_2 in various types of telecommunication fiber at 1.55 μm," *Opt. Lett.*, vol. 21, no. 24, pp. 1966–1968, 1996.

[104] P. Blandin, F. Druon, M. Hanna, S. Lévêque-Fort, C. Lesvigne, V. Couderc, P. Leproux, A. Tonello, and P. Georges, "Picosecond polarized supercontinuum generation controlled by intermodal four-wave mixing for fluorescence lifetime imaging microscopy," *Opt. Express*, vol. 16, no. 23, pp. 18 844–18 849, 2008.

[105] C. Xiong and W. J. Wadsworth, "Polarized supercontinuum in birefringent photonic crystal fibre pumped at 1064 nm and application to tuneable visible/uv generation," *Opt. Express*, vol. 16, no. 4, pp. 2438–2445, 2008.

[106] B. Daino, G. Gregori, and S. Wabnitz, "New all-optical devices based on third-order nonlinearity of birefringent fibers," *Opt. Lett.*, vol. 11, no. 1, pp. 42–44, 1986.

[107] S. Trillo, S. Wabnitz, R. H. Stolen, G. Assanto, C. T. Seaton, and G. I. Stegeman, "Experimental observation of polarization instability in a birefringent optical fiber," *Applied Physics Letters*, vol. 49, no. 19, pp. 1224–1226, 1986.

[108] P. Morin, B. Kibler, J. Fatome, C. Finot, and G. Millot, "Group birefringence cancellation in highly birefringent photonic crystal fibre at telecommunication wavelengths," *Electron. Lett.*, vol. 46, no. 7, pp. 525 –526, 2010.

[109] Y. Sasaki, T. Hosaka, and J. Noda, "Low-loss polarisation-maintaining optical fibre with low crosstalk," *Electronics Letters*, vol. 21, no. 4, pp. 156 –157, 1985.

[110] J. Noda, K. Okamoto, and Y. Sasaki, "Polarization-maintaining fibers and their applications," *J. Lightwave Technol.*, vol. 4, no. 8, pp. 1071–1089, 1986.

[111] Y. Sasaki, T. Hosaka, M. Horiguchi, and J. Noda, "Design and fabrication of low-loss and low-crosstalk polarization-maintaining optical fibers," *J. Lightwave Technol.*, vol. 4, no. 8, pp. 1097 – 1102, 1986.

[112] K. Okamoto and T. Hosaka, "Polarization-dependent chromatic dispersion in birefringent optical fibers," *Opt. Lett.*, vol. 12, no. 4, pp. 290–292, 1987.

[113] M. P. Varnham, D. N. Payne, R. D. Birch, and E. J. Tarbox, "Single-polarisation operation of highly birefringent bow-tie optical fibres," *Electronics Letters*, vol. 19, no. 7, pp. 246–247, 1983.

[114] Y. Jung, G. Brambilla, K. Oh, and D. J. Richardson, "Highly birefringent silica microfiber," *Opt. Lett.*, vol. 35, no. 3, pp. 378–380, 2010.

[115] T. Okoshi, K. Oyamada, M. Nishimura, and H. Yokota, "Side-tunnel fibre: an approach to polarisation-maintaining optical waveguiding scheme," *Electronics Letters*, vol. 18, no. 19, pp. 824–826, 1982.

[116] A. Ortigosa-Blanch, J. C. Knight, W. J. Wadsworth, J. Arriaga, B. J. Mangan, T. A. Birks, and P. S. J. Russell, "Highly birefringent photonic crystal fibers," *Opt. Lett.*, vol. 25, no. 18, pp. 1325–1327, 2000.

[117] X. Chen, M. Li, N. Venkataraman, M. Gallagher, W. Wood, A. Crowley, J. Carberry, L. Zenteno, and K. Koch, "Highly birefringent hollow-core photonic bandgap fiber," in *Optical Fiber Communication Conference and Exposition and The National Fiber Optic Engineers Conference*. Optical Society of America, 2005, p. OTuI1.

[118] A. Alphones and G. S. Sanyal, "Propagation characteristics of eccentric core fibers using point-matching method," *Proceedings of the IEEE*, vol. 74, no. 10, pp. 1456 – 1458, 1986.

[119] G. F. M. L. C. Sawyer, D. T. Grubb, *Polymer Microscopy*, 3rd ed. Springer, 2008.

[120] S. C. Rashleigh, "Wavelength dependence of birefringence in highly birefringent fibers," *Opt. Lett.*, vol. 7, no. 6, pp. 294–296, 1982.

[121] K. Kikuchi and T. Okoshi, "Wavelength-sweeping technique for measuring the beat length of linearly birefringent optical fibers," *Opt. Lett.*, vol. 8, no. 2, pp. 122–123, 1983.

[122] S. C. Rashleigh, "Measurement of fiber birefringence by wavelength scanning: effect of dispersion," *Opt. Lett.*, vol. 8, no. 6, pp. 336–338, 1983.